

Higgs Physics at the CLIC Electron-Positron Linear Collider

H. Abramowicz¹, A. Abusleme², K. Afanaciev³, N. Alipour Tehrani⁴, C. Balázs⁵,
Y. Benhammou¹, M. Benoit⁶, B. Bilki⁷, J.-J. Blaising⁸, M.J. Boland⁹, M. Boronat¹⁰,
O. Borysov¹, I. Božović-Jelisavčić¹¹, M. Buckland¹², S. Bugiel¹³, P.N. Burrows¹⁴,
T.K. Charles⁵, W. Daniluk¹⁵, D. Dannheim⁴, R. Dasgupta¹³, M. Demarteau⁷, M.A. Díaz
Gutierrez², G. Eigen¹⁶, K. Elsener⁴, U. Felzmann⁹, M. Firlej¹³, E. Firt¹⁷, T. Fiutowski¹³,
J. Fuster¹⁰, M. Gabriel¹⁸, F. Gaede^{4,19}, I. García¹⁰, V. Ghenescu¹⁷, J. Goldstein²⁰,
S. Green²¹, C. Greife^{4,a,*}, M. Hauschild⁴, C. Hawkes²², D. Hynds⁴, M. Idzik¹³,
G. Kačarevič¹¹, J. Kalinowski²³, S. Kananov¹, W. Klempt⁴, M. Kopec¹³, M. Krawczyk²³,
B. Krupa¹⁵, M. Kucharczyk¹⁵, S. Kulis⁴, T. Laštovička²⁴, T. Lesiak¹⁵, A. Levy¹,
I. Levy¹, L. Linssen⁴, S. Lukić^{11,*}, A.A. Maier⁴, V. Makarenko³, J.S. Marshall²¹,
K. Mei²¹, G. Milutinović-Dumbelović¹¹, J. Moron¹³, A. Moszczyński¹⁵, D. Moya²⁵,
R.M. Münker^{4,b}, A. Münnich^{4,c}, A.T. Neagu¹⁷, N. Nikiforou⁴, K. Nikolopoulos²²,
A. Nürnberg⁴, M. Pandurović¹¹, B. Pawlik¹⁵, E. Perez Codina⁴, I. Peric²⁶, M. Petric⁴,
F. Pitters^{4,d}, S.G. Poss⁴, T. Preda¹⁷, D. Protopopescu²⁷, R. Rassool⁹, S. Redford^{4,e,*},
J. Repond⁷, A. Robson²⁷, P. Roloff^{4,*}, E. Ros¹⁰, O. Rosenblatt¹, A. Ruiz-Jimeno²⁵,
A. Sailer⁴, D. Schlatter⁴, D. Schulte⁴, N. Shumeiko^{3,†}, E. Sicking⁴, F. Simon^{18,*},
R. Simoniello⁴, P. Sopicki¹⁵, S. Stapnes⁴, R. Ström⁴, J. Strube^{4,f}, K.P. Świentek¹³,
M. Szalay¹⁸, M. Tesař¹⁸, M.A. Thomson^{21,*}, J. Trenado²⁸, U.I. Uggerhøj²⁹,
N. van der Kolk¹⁸, E. van der Kraaij¹⁶, M. Vicente Barreto Pinto⁶, I. Vila²⁵,
M. Vogel Gonzalez^{2,g}, M. Vos¹⁰, J. Vosseveld¹², M. Watson²², N. Watson²², M.A. Weber⁴,
H. Weerts⁷, J.D. Wells³⁰, L. Weuste¹⁸, A. Winter²², T. Wojtoń¹⁵, L. Xia⁷, B. Xu²¹,
A.F. Żarnecki²³, L. Zawiejski¹⁵, I.-S. Zgura¹⁷

¹Raymond & Beverly Sackler School of Physics & Astronomy, Tel Aviv University, Tel Aviv, Israel

²Pontificia Universidad Católica de Chile, Santiago, Chile

³National Scientific and Educational Centre of Particle and High Energy Physics, Belarusian State University, Minsk, Belarus

⁴CERN, Geneva, Switzerland

⁵Monash University, Melbourne, Australia

⁶Département de Physique Nucléaire et Corpusculaire (DPNC), Université de Genève, Geneva, Switzerland

⁷Argonne National Laboratory, Argonne, USA

⁸Laboratoire d'Annecy-le-Vieux de Physique des Particules, Annecy-le-Vieux, France

⁹University of Melbourne, Melbourne, Australia

¹⁰IFIC, CSIC-University of Valencia, Valencia, Spain

¹¹Vinča Institute of Nuclear Sciences, University of Belgrade, Belgrade, Serbia

¹²University of Liverpool, Liverpool, United Kingdom

¹³Faculty of Physics and Applied Computer Science, AGH University of Science and Technology, Cracow, Poland

¹⁴Oxford University, Oxford, United Kingdom

¹⁵The Henryk Niewodniczański Institute of Nuclear Physics Polish Academy of Sciences, Cracow, Poland

¹⁶Department of Physics and Technology, University of Bergen, Bergen, Norway

¹⁷Institute of Space Science, Bucharest, Romania

¹⁸Max-Planck-Institut für Physik, Munich, Germany

¹⁹DESY, Hamburg, Germany

²⁰University of Bristol, Bristol, United Kingdom

²¹Cavendish Laboratory, University of Cambridge, Cambridge, United Kingdom

²²School of Physics and Astronomy, University of Birmingham, Birmingham, United Kingdom

²³Faculty of Physics, University of Warsaw, Poland

²⁴Institute of Physics of the Academy of Sciences of the Czech Republic, Prague, Czech Republic

²⁵IFCA, CSIC-University of Cantabria, Santander, Spain

²⁶Karlsruher Institut für Technologie (KIT), Institut für Prozessdatenverarbeitung und Elektronik (IPE), Karlsruhe, Germany

²⁷University of Glasgow, Glasgow, United Kingdom

²⁸University of Barcelona, Barcelona, Spain

²⁹Aarhus University, Aarhus, Denmark

³⁰Physics Department, University of Michigan, Ann Arbor, Michigan, USA

Received: date / Accepted: date

Abstract The Compact Linear Collider (CLIC) is an option for a future e^+e^- collider operating at centre-of-mass energies up to 3 TeV, providing sensitivity to a wide range of new physics phenomena and precision physics measurements at the energy frontier. This paper presents the Higgs physics reach of CLIC operating in three energy stages, $\sqrt{s} = 350$ GeV, 1.4 TeV and 3 TeV. The initial stage of operation allows the study of Higgs boson production in Higgsstrahlung ($e^+e^- \rightarrow ZH$) and WW-fusion ($e^+e^- \rightarrow H\nu_e\bar{\nu}_e$), resulting in precise measurements of the production cross sections, the Higgs total decay width Γ_H , and model-independent determinations of the Higgs couplings. Operation at $\sqrt{s} > 1$ TeV provides high-statistics samples of Higgs bosons produced through WW-fusion, enabling tight constraints on the Higgs boson couplings. Studies of the rarer processes $e^+e^- \rightarrow t\bar{t}H$ and $e^+e^- \rightarrow HH\nu_e\bar{\nu}_e$ would allow measurements of the top Yukawa coupling and the Higgs boson self-coupling. This paper presents detailed studies of the precision achievable with Higgs measurements at CLIC and describes the interpretation of these measurements in a global fit.

Contents

1	Introduction	2
2	Experimental Environment at CLIC	3
3	Overview of Higgs Production at CLIC	4
4	Event Generation, Detector Simulation and Reconstruction	9
5	Higgs Production at $\sqrt{s} = 350$ GeV	10
6	WW-fusion at $\sqrt{s} > 1$ TeV	20
7	ZZ-fusion	29
8	Top Yukawa Coupling	30
9	Double Higgs Production	32
10	Higgs Mass	33
11	Combined Fits	34

*Corresponding Editors: clicdp-higgs-paper-editors@cern.ch

[†]Deceased

^aNow at University of Bonn, Bonn, Germany

^bAlso at University of Bonn, Bonn, Germany

^cNow at European XFEL GmbH, Hamburg, Germany

^dAlso at Vienna University of Technology, Vienna, Austria

^eNow at Paul Scherrer Institute, Villigen, Switzerland

^fNow at Pacific Northwest National Laboratory, Richland, Washington, USA

^gNow at University of Wuppertal, Wuppertal, Germany

12 Summary and Conclusions

1 Introduction

The discovery of a Higgs boson [1, 2] at the Large Hadron Collider (LHC) provided confirmation of the electroweak symmetry breaking mechanism [3–8] of the Standard Model (SM). However, it is not yet known if the observed Higgs boson is the fundamental scalar of the SM or is either a more complex object or part of an extended Higgs sector. Precise studies of the properties of the Higgs boson at the LHC and future colliders are essential to understand its true nature.

The Compact Linear Collider (CLIC) is the only mature option for a future multi-TeV high-luminosity linear e^+e^- collider and is currently under development at CERN. It is based on a novel two-beam acceleration technique providing accelerating gradients of 100 MV/m. Recent implementation studies for CLIC have converged towards a staged approach offering a unique physics programme spanning several decades. In this scheme, CLIC would provide high-luminosity e^+e^- collisions at centre-of-mass energies from a few hundred GeV up to 3 TeV. For the current study, the nominal centre-of-mass energy of the first energy stage was chosen to be $\sqrt{s} = 350$ GeV. At this centre-of-mass energy, the Higgsstrahlung and WW-fusion processes have significant cross sections, giving access to precise measurement of absolute values of Higgs couplings to both fermions and bosons. Another advantage of operating the first stage of CLIC at $\sqrt{s} \approx 350$ GeV is that it enables a programme of precision top quark physics, including a scan of the $t\bar{t}$ cross section close to the production threshold. In practice, the centre-of-mass energy of the second stage of CLIC operation would be motivated by both the machine design and the results from the LHC. Here it was assumed that the second CLIC energy stage has $\sqrt{s} = 1.4$ TeV and that the ultimate CLIC centre-of-mass energy is 3 TeV. In addition to direct and indirect searches for Beyond the Standard Model (BSM) phenomena, these higher energy stages of operation provide a rich potential for Higgs physics beyond that accessible at lower energies, such as the direct measurement of the top Yukawa coupling and a direct probe of the Higgs potential through the measurement of the Higgs self-coupling. Furthermore, rare Higgs boson decays become accessible due to the higher integrated luminosities at higher energies and the increasing cross section for Higgs production in WW-fusion.

The following sections describe: the experimental conditions at CLIC; an overview of Higgs production at CLIC; the Monte Carlo samples, detector simulation and event reconstruction used for the subsequent studies; Higgs production at $\sqrt{s} = 350$ GeV; Higgs production in WW-fusion at $\sqrt{s} > 1$ TeV; Higgs production in ZZ-fusion; the measurement of

the top Yukawa coupling; double Higgs production; measurements of the Higgs boson mass; and conclude with a discussion of the resulting measurement precisions on the Higgs couplings obtained in a combined fit to the expected CLIC results.

The detailed study of the CLIC potential for Higgs physics presented here supersedes earlier preliminary estimates [9].

2 Experimental Environment at CLIC

The experimental environment at CLIC is characterised by challenging conditions imposed by the CLIC accelerator technology, by detector concepts optimised for the precise reconstruction of complex final states in the multi-TeV energy range and by the operation in several energy stages to maximise the physics potential.

2.1 Accelerator and Beam Conditions

The CLIC accelerator design is based on a two-beam acceleration scheme. It uses a high-intensity drive beam to efficiently generate radio frequency (RF) power at 12 GHz. The RF power is used to accelerate the main particle beam that runs parallel to the drive beam. CLIC uses normal-conducting accelerator structures, operated at room temperature. These structures permit high accelerating gradients, while the short pulse duration discussed below limits ohmic losses to tolerable levels. The initial drive beams and the main electron/positron beams are generated in the central complex and are then injected at the ends of the two linac arms. The feasibility of the CLIC accelerator has been demonstrated through prototyping, simulations and large-scale tests, as described in the Conceptual Design Report [10]. In particular, the two-beam acceleration at gradients exceeding 100 MV/m has been demonstrated in the CLIC test facility, CTF3. High luminosities are achievable by very small beam emittances, which are generated in the injector complex and maintained during transport to the interaction point.

CLIC is to be operated with a bunch train repetition rate of 50 Hz. Each bunch train consists of 312 individual bunches, with 0.5 ns between bunch crossings at the interaction point. The average number of hard e^+e^- interactions in a single bunch train crossing is much less than one. However, for CLIC operation at $\sqrt{s} > 1$ TeV, the highly-focussed intense beams lead to significant beamstrahlung (radiation of photons from electrons/positrons in the electric field of the other beam). Beamstrahlung results in high rates of incoherent electron-positron pairs and low- Q^2 t -channel multi-peripheral $\gamma\gamma \rightarrow$ hadron events, where Q^2 is the negative of the four-

momentum squared of the virtual space-like photon. In addition, the energy loss through beamstrahlung generates a long lower-energy tail to the luminosity spectrum that extends well below the nominal centre-of-mass energy. Both the CLIC detector design and the event reconstruction techniques employed are optimised to mitigate the influence of these backgrounds, which are most severe at the higher CLIC energies.

The baseline machine design allows for up to $\pm 80\%$ electron polarisation, while provisions have been made to allow positron polarisation as an upgrade option. Most studies presented in this paper are performed for zero beam polarisation and are subsequently scaled to account for the increased cross sections with left-handed polarisation for the electron beam.

2.2 Detectors at CLIC

The detector concepts used for the CLIC physics studies, described here and elsewhere [11], are based on the SiD [12, 13] and ILD [13, 14] detector concepts for the International Linear Collider (ILC). They were initially adapted for the CLIC 3 TeV operation, which constitutes the most challenging environment for the detectors in view of the high beam-induced background levels. For most sub-detector systems, the 3 TeV detector design is suitable at all energy stages. The only exception being the inner tracking detectors and the vertex detector, where the lower backgrounds at $\sqrt{s} = 350$ GeV enable detectors to be deployed with a smaller inner radius.

The key performance parameters of the CLIC detector concepts with respect to the Higgs programme are:

- excellent track-momentum resolution of $\sigma_{p_T}/p_T^2 \lesssim 2 \cdot 10^{-5} \text{ GeV}^{-1}$, required for a precise reconstruction of leptonic Z decays in ZH events;
- precise impact parameter resolution defined by $a \lesssim 5 \mu\text{m}$ and $b \lesssim 15 \mu\text{m GeV}$ in $\sigma_{d_0}^2 = a^2 + b^2/(p^2 \sin^3 \theta)$ to provide accurate vertex reconstruction, enabling flavour tagging with clean b-, c- and light-quark jet separation;
- jet-energy resolution $\sigma_E/E \lesssim 3.5\%$ for jet energies in the range 100 GeV to 1 TeV, required for the reconstruction of hadronic Z decays in ZH events and the separation of $W \rightarrow q\bar{q}$, $Z \rightarrow q\bar{q}$ and $H \rightarrow q\bar{q}$ based on the reconstructed di-jet invariant mass;
- detector coverage for electrons extending to very low angles with respect to the beam axis, to maximise background rejection for WW-fusion events.

The main design driver for the CLIC (and ILC) detector concepts is the required jet-energy resolution. As a result, the CLIC detector concepts [11], CLIC_SiD and CLIC_ILD,

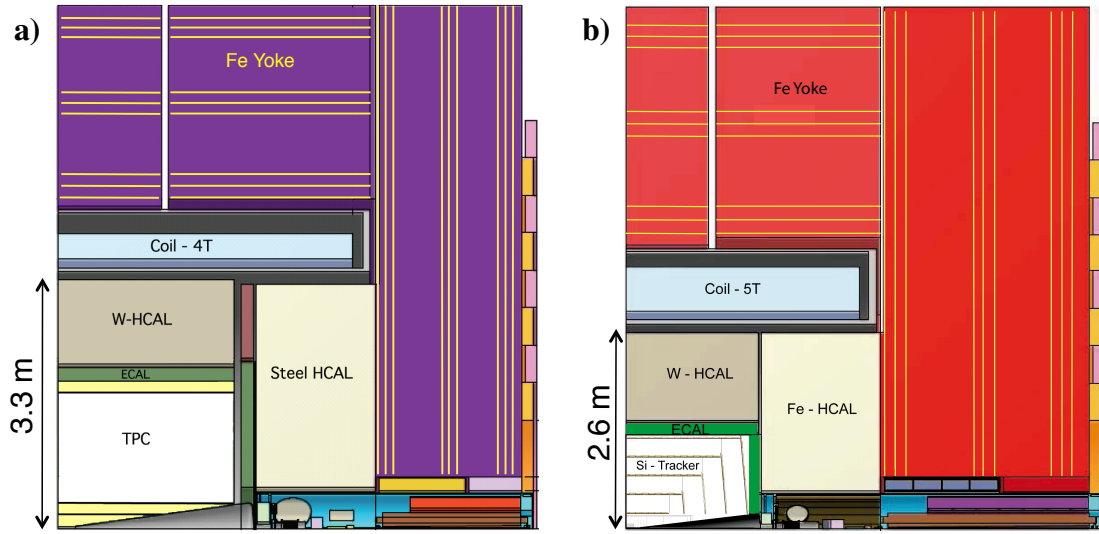


Fig. 1: Longitudinal cross section of the top right quadrant of the CLIC_ILD (a) and CLIC_SiD (b) detector concepts.

are based on fine-grained electromagnetic and hadronic calorimeters (ECAL and HCAL), optimised for particle-flow analysis techniques. In the particle-flow approach, the aim is to reconstruct the individual final-state particles within a jet using information from the tracking detectors combined with that from the highly granular calorimeters [15, 16]. In addition, particle-flow event reconstruction provides a powerful tool for the rejection of beam-induced backgrounds [11]. The CLIC detector concepts employ strong central solenoid magnets, located outside the HCAL, providing an axial magnetic field of 5 T in CLIC_SiD and 4 T in CLIC_ILD. The CLIC_SiD concept employs central silicon-strip tracking detectors, whereas CLIC_ILD assumes a large central gaseous Time Projection Chamber. In both concepts, the central tracking system is augmented with silicon-based inner tracking detectors. The two detector concepts are shown schematically in Figure 1 and are described in detail in [11].

2.3 Assumed Staged Running Scenario

The studies presented in this paper are based on a particular staging scenario for CLIC, which assumes a three-stage implementation. The first stage provides a centre-of-mass energy of around 350 GeV to reach the top-pair production threshold. The second stage extends up to $\sqrt{s} = 1.4$ TeV. This energy was chosen because it can be reached with a single CLIC drive-beam complex. The third stage reaches $\sqrt{s} = 3$ TeV, the ultimate energy of CLIC. At each stage, four to five years of running with a fully commissioned accelerator are foreseen, providing integrated luminosities of 500 fb^{-1} ,

1.5 ab^{-1} and 2 ab^{-1} at 350 GeV, 1.4 TeV and 3 TeV, respectivelyⁱ.

3 Overview of Higgs Production at CLIC

A high-energy e^+e^- collider such as CLIC provides a clean experimental environment to study the properties of the Higgs boson with high precision. The evolution of the leading-order e^+e^- Higgs production cross sections with centre-of-mass energy is shown in Figure 2 for a Higgs boson mass of 126 GeV [18].

The Feynman diagrams for the three highest cross section Higgs production processes at CLIC are shown in Figure 3. In the initial stage of operation at $\sqrt{s} \approx 350$ GeV, the Higgsstrahlung process ($e^+e^- \rightarrow ZH$) has the largest cross section, but the WW-fusion process ($e^+e^- \rightarrow H\nu_e\bar{\nu}_e$) is also significant. The combined study of these two processes probes the Higgs boson properties (width and branching ratios) in a model-independent manner. In the higher energy stages of CLIC operation ($\sqrt{s} = 1.4$ TeV and 3 TeV), Higgs production is dominated by the WW-fusion process, with the ZZ-fusion process ($e^+e^- \rightarrow H e^+e^-$) also becoming significant. Here the relatively large WW-fusion cross section, combined with the high luminosity of CLIC, results in large data samples, allowing precise $\mathcal{O}(1\%)$ measurements of the couplings of the Higgs boson to both fermions and gauge bosons. In addition to the main Higgs production channels, rarer processes such as $e^+e^- \rightarrow t\bar{t}H$ and $e^+e^- \rightarrow HH\nu_e\bar{\nu}_e$,

ⁱA slightly different staging scenario for CLIC, with a first stage at 380 GeV to include precise measurements of top quark properties as a probe for BSM physics, has recently been proposed [17].

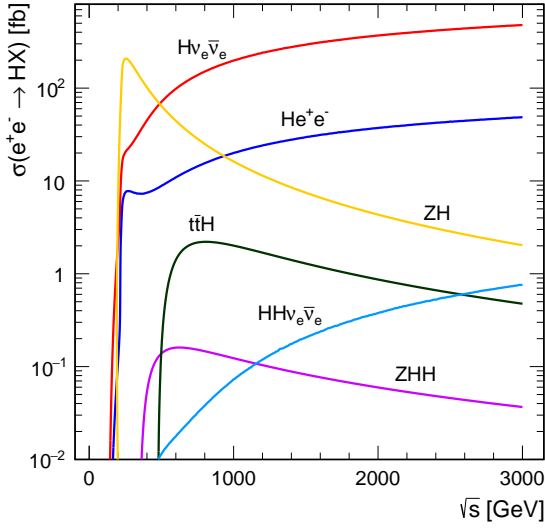


Fig. 2: Cross section as a function of centre-of-mass energy for the main Higgs production processes at an e^+e^- collider for a Higgs mass of $m_H = 126 \text{ GeV}$. The values shown correspond to unpolarised beams and do not include the effect of beamstrahlung.

provide access to the top Yukawa coupling and the Higgs trilinear self-coupling governed by the parameter λ in the Higgs potential. Feynman diagrams for these processes are shown in Figure 4. In all cases, the Higgs production cross sections can be increased with polarised electron (and positron) beams.

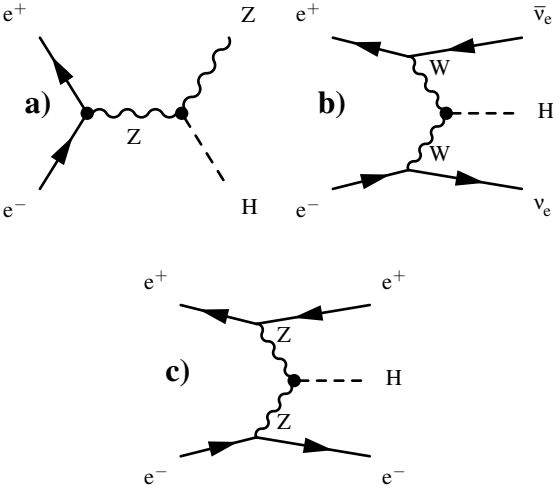


Fig. 3: Leading-order Feynman diagrams of the highest cross section Higgs production processes at CLIC; Higgsstrahlung (a), WW-fusion (b) and ZZ-fusion (c).

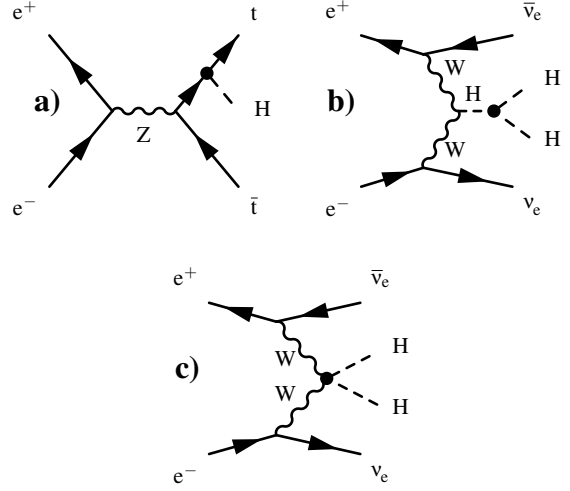


Fig. 4: Feynman diagrams of the leading-order processes at CLIC involving the top Yukawa coupling g_{Htt} (a), the Higgs boson trilinear self-coupling λ (b) and the quartic coupling g_{HHWW} (c).

Table 1 lists the expected numbers of ZH, $H\nu_e\bar{\nu}_e$ and He^+e^- events for the three main CLIC centre-of-mass energy stages. These numbers account for the effect of beamstrahlung and initial state radiation (ISR), which result in a tail in the distribution of the effective centre-of-mass energy $\sqrt{s'}$. The impact of beamstrahlung on the expected numbers of events is mostly small. For example, it results in an approximately 10% reduction in the numbers of $H\nu_e\bar{\nu}_e$ events at $\sqrt{s} > 1 \text{ TeV}$ (compared to the beam spectrum with ISR alone), because the cross section rises relatively slowly with \sqrt{s} . The reduction of the effective centre-of-mass energies due to ISR and beamstrahlung leads to moderate numbers of ZH events at $\sqrt{s} = 1.4 \text{ TeV}$ and 3 TeV .

The polar angle distributions for single Higgs production obtained using WHIZARD 1.95 [19] for the CLIC centre-of-mass energies are shown in Figure 5. Most Higgs bosons produced at $\sqrt{s} = 350 \text{ GeV}$ can be reconstructed in the central parts of the detectors while the Higgs bosons produced in the WW-fusion process and their decay products tend towards the beam axis with increasing energy. Hence good capabilities of the detectors in the forward regions are crucial at $\sqrt{s} = 1.4 \text{ TeV}$ and 3 TeV .

A SM Higgs boson with mass of $m_H = 126 \text{ GeV}$ has a wide range of decay modes, as listed in Table 2, providing the possibility to test the SM predictions for the couplings of the Higgs to both gauge bosons and to fermions [20]. All the modes listed in Table 2 are accessible at CLIC.

$\sqrt{s} =$	350 GeV	1.4 TeV	3 TeV
\mathcal{L}_{int}	500 fb ⁻¹	1.5 ab ⁻¹	2 ab ⁻¹
$\sigma(e^+e^- \rightarrow \text{ZH})$	133 fb	8 fb	2 fb
$\sigma(e^+e^- \rightarrow \text{H}\nu_e\bar{\nu}_e)$	34 fb	276 fb	477 fb
$\sigma(e^+e^- \rightarrow \text{He}^+e^-)$	7 fb	28 fb	48 fb
# ZH events	68,000	20,000	11,000
# $\text{H}\nu_e\bar{\nu}_e$ events	17,000	370,000	830,000
# He^+e^- events	3,700	37,000	84,000

Table 1: The leading-order Higgs unpolarised cross sections for the Higgsstrahlung, WW-fusion, and ZZ-fusion processes for $m_H = 126 \text{ GeV}$ at the three centre-of-mass energies discussed in this document. The quoted cross sections include the effects of ISR but do not include the effects of beamstrahlung. Also listed are the numbers of expected events including the effects of the CLIC beamstrahlung spectrum and ISR. The cross sections and expected event numbers do not account for the possible enhancements from polarised beams.

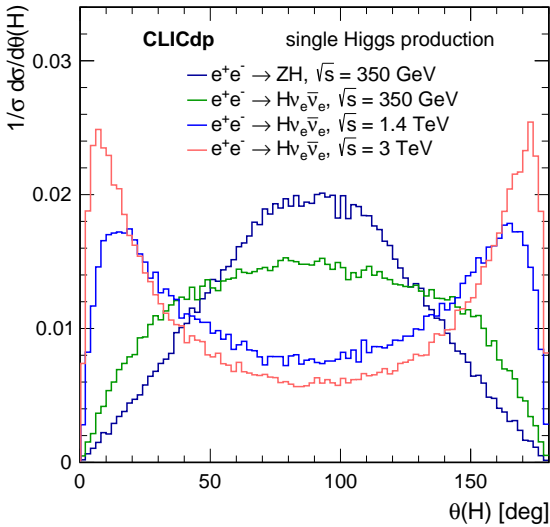


Fig. 5: Polar angle distributions for single Higgs events at $\sqrt{s} = 350 \text{ GeV}$, 1.4 TeV and 3 TeV , including the effects of the CLIC beamstrahlung spectrum and ISR. The distributions are normalised to unity.

3.1 Motivation for $\sqrt{s} = 350 \text{ GeV}$ CLIC Operation

The choice of the CLIC energy stages is motivated by the desire to pursue a programme of precision Higgs physics and to operate the machine above 1 TeV at the earliest possible time; no CLIC operation is foreseen below the top-pair production threshold. From the perspective of Higgs physics, lower-energy operation is partly motivated by the direct and model-independent measurement of the coupling of the Higgs boson to the Z, which can be obtained from the

Decay mode	Branching ratio
$\text{H} \rightarrow b\bar{b}$	56.1 %
$\text{H} \rightarrow \text{WW}^*$	23.1 %
$\text{H} \rightarrow g\bar{g}$	8.5 %
$\text{H} \rightarrow \tau^+\tau^-$	6.2 %
$\text{H} \rightarrow c\bar{c}$	2.8 %
$\text{H} \rightarrow \text{ZZ}^*$	2.9 %
$\text{H} \rightarrow \gamma\gamma$	0.23 %
$\text{H} \rightarrow \text{Z}\gamma$	0.16 %
$\text{H} \rightarrow \mu^+\mu^-$	0.021 %
Γ_H	4.2 MeV

Table 2: The investigated SM Higgs decay modes and their branching ratios as well as the total Higgs width for $m_H = 126 \text{ GeV}$ [20].

recoil mass distribution in $\text{ZH} \rightarrow e^+e^- \text{H}$, $\text{ZH} \rightarrow \mu^+\mu^- \text{H}$ and $\text{ZH} \rightarrow q\bar{q} \text{H}$ production (see Section 5.1.1 and Section 5.1.3). These measurements play a central role in the determination of the Higgs couplings at a linear collider. Thus, it might seem surprising that no significant CLIC running is considered at $\sqrt{s} = 250 \text{ GeV}$, which is close to the maximum of the Higgsstrahlung cross section (see Figure 2).

There are three reasons why 250 GeV operation is not considered a priority. Firstly, the reduction in cross section in going to $\sqrt{s} = 350 \text{ GeV}$ is compensated, in part, by the increased instantaneous luminosity achievable at a higher centre-of-mass energy. The instantaneous luminosity scales approximately linearly with the centre-of-mass energy, $\mathcal{L} \propto \gamma_e$, where γ_e is the Lorentz factor for the beam electrons/positrons. For this reason the precision on the coupling g_{HZZ} at 350 GeV is comparable to that achievable at 250 GeV for the same period of operation. Secondly, the additional boost of the Z and H at $\sqrt{s} = 350 \text{ GeV}$ provides greater separation between the final-state jets from Z and H decays. Consequently, the measurements of $\sigma(\text{ZH}) \times \text{BR}(\text{H} \rightarrow X)$ can be more precise at $\sqrt{s} = 350 \text{ GeV}$. Thirdly, and most importantly, measurements of the Higgsstrahlung cross section alone are not sufficient to provide truly model-independent measurements of the Higgs boson couplings; knowledge of the total decay width Γ_H is also required. This can be inferred from the measurements of the cross sections for the WW-fusion processes. Initial operation of CLIC at $\sqrt{s} \approx 350 \text{ GeV}$, where the $e^+e^- \rightarrow \text{H}\nu_e\bar{\nu}_e$ fusion cross section is significant, provides constraints on the Higgs coupling to the W boson and, by inference, provides a determination of the Higgs width Γ_H . For the above reasons, the preferred option for the first stage of CLIC operation is $\sqrt{s} \approx 350 \text{ GeV}$.

Another advantage of $\sqrt{s} \approx 350 \text{ GeV}$ is that detailed studies of the top-pair production process can be performed in the initial stage of CLIC operation. Finally, it is worth noting that a similar Higgs boson mass precision can be obtained from the recoil mass distribution in $\text{ZH} \rightarrow \mu^+\mu^- \text{H}$

Polarisation $P(e^-) : P(e^+)$	Enhancement factor		
	$e^+e^- \rightarrow ZH$	$e^+e^- \rightarrow H\nu_e\bar{\nu}_e$	$e^+e^- \rightarrow He^+e^-$
unpolarised	1.00	1.00	1.00
-80 % : 0 %	1.12	1.80	1.12
-80 % : +30 %	1.40	2.34	1.17
-80 % : -30 %	0.83	1.26	1.07
+80 % : 0 %	0.88	0.20	0.88
+80 % : +30 %	0.69	0.26	0.92
+80 % : -30 %	1.08	0.14	0.84

Table 3: The dependence of the event rates for the s -channel $e^+e^- \rightarrow ZH$ process and the pure t -channel $e^+e^- \rightarrow H\nu_e\bar{\nu}_e$ and $e^+e^- \rightarrow He^+e^-$ processes for several example beam polarisations. The scale factors assume an effective weak mixing angle given by $\sin^2 \theta_W^{\text{eff}} = 0.23146$ [21]. The numbers are approximate as they do not account for interference between $e^+e^- \rightarrow ZH \rightarrow \nu_e\bar{\nu}_e H$ and $e^+e^- \rightarrow H\nu_e\bar{\nu}_e$.

at $\sqrt{s} = 250 \text{ GeV}$ or from the direct reconstruction of the Higgs decay products in, for example, $H \rightarrow q\bar{q}$ decays at $\sqrt{s} = 350 \text{ GeV}$ and higher.

3.2 Impact of Beam Polarisation

The majority of CLIC Higgs physics studies have been performed assuming unpolarised e^+ and e^- beams. However, for the baseline CLIC design, the electron beam can be polarised up to $\pm 80\%$. There is the possibility of positron polarisation at a lower level, although this is not in the baseline CLIC machine design. For an electron polarisation of P_- and positron polarisation of P_+ , the relative fractions of collisions in the different helicity states are:

$$e_R^- e_R^+ : \frac{1}{4}(1+P_-)(1+P_+) , \quad e_R^- e_L^+ : \frac{1}{4}(1+P_-)(1-P_+) , \\ e_L^- e_R^+ : \frac{1}{4}(1-P_-)(1+P_+) , \quad e_L^- e_L^+ : \frac{1}{4}(1-P_-)(1-P_+) .$$

By selecting different beam polarisations it is possible to enhance/suppress different physical processes. The chiral nature of the weak coupling to fermions results in significant possible enhancements in WW-fusion Higgs production, as indicated in Table 3. The potential gains for the s -channel Higgsstrahlung process, $e^+e^- \rightarrow ZH$, are less significant, and the $e^+e^- \rightarrow He^+e^-$ cross section dependence on the polarisation is even smaller. In practice, the balance between operation with different beam polarisations will depend on the CLIC physics programme taken as a whole, including the searches for and potential measurements of BSM particle production.

3.3 Overview of Higgs Measurements at $\sqrt{s} = 350 \text{ GeV}$

The Higgsstrahlung process provides the opportunity to study the couplings of the Higgs boson in a model-independent manner. This is unique to an electron-positron collider. The clean experimental environment, and the relatively low SM cross sections for background processes, allow $e^+e^- \rightarrow ZH$ events to be selected based solely on the measurement of the four-momentum of the Z through its decay products. The most distinct event topologies occur for $Z \rightarrow e^+e^-$ and $Z \rightarrow \mu^+\mu^-$ decays, which can be identified by requiring that the di-lepton invariant mass is consistent with m_Z . In $e^+e^- \rightarrow ZH$ events, the invariant mass of the system recoiling against the Z boson will peak at m_H , allowing the ZH events to be selected based only on the observation of the leptons from the Z decay, providing a model-independent measurement of the Higgs coupling to the Z boson (see Section 5.1.1). A slightly less clean, but more precise, measurement is obtained from the recoil mass analysis for $Z \rightarrow q\bar{q}$ decays (see Section 5.1.3).

The recoil-mass studies provide an absolute measurement of the total ZH production cross section and a model-independent measurement of the coupling of the Higgs to the Z boson, g_{HZZ} . The combination of the leptonic and hadronic decay channels allows g_{HZZ} to be determined with a precision of 0.8 %. In addition, the recoil mass from $Z \rightarrow q\bar{q}$ decays provides a direct search for possible Higgs decays to invisible final states, and can be used to constrain the invisible decay width of the Higgs, Γ_{invis} .

By identifying the individual final states for different Higgs decay modes, precise measurements of the Higgs boson branching fractions can be made. Because of the high flavour tagging efficiencies [11] achievable at CLIC, the $H \rightarrow b\bar{b}$ and $H \rightarrow c\bar{c}$ decays can be cleanly separated. Neglecting the Higgs decays into light quarks, the branching ratio of $H \rightarrow gg$ can also be inferred and $H \rightarrow \tau^+\tau^-$ decays can be identified.

Although the cross section is lower, the t -channel WW-fusion process $e^+e^- \rightarrow H\nu_e\bar{\nu}_e$ is an important part of the CLIC Higgs physics programme at $\sqrt{s} \approx 350 \text{ GeV}$. Because the final state consists of the Higgs boson decay products alone, the direct reconstruction of the invariant mass of the Higgs boson or, in the case of $H \rightarrow WW^*$, its decay products, plays a central role in the event selection. The combination of Higgs production and decay data from Higgsstrahlung and WW-fusion processes provides a model-independent extraction of Higgs couplings.

3.3.1 Extraction of Higgs Couplings

At the LHC, only ratios of the Higgs boson couplings can be inferred from the data in a model-independent way. At an electron-positron collider, absolute measurements of the couplings can be determined using the total $e^+e^- \rightarrow ZH$ cross section from the recoil mass analyses. This allows the coupling of the Higgs boson to the Z to be determined with a precision of better than 1 % in an essentially model-independent manner. Once the coupling to the Z is known, the Higgs coupling to the W can be determined from, for example, the ratios of Higgsstrahlung to WW-fusion cross sections:

$$\frac{\sigma(e^+e^- \rightarrow ZH) \times BR(H \rightarrow b\bar{b})}{\sigma(e^+e^- \rightarrow \nu_e \bar{\nu}_e H) \times BR(H \rightarrow b\bar{b})} \propto \left(\frac{g_{HZZ}}{g_{HWW}} \right)^2.$$

In order to determine absolute measurements of the other Higgs couplings, the Higgs total decay width needs to be inferred from the data.

For a Higgs boson mass of around 126 GeV, the total Higgs decay width in the SM (Γ_H) is less than 5 MeV and cannot be measured directly. However, given that the absolute couplings of the Higgs boson to the Z and W can be obtained as described above, the total decay width of the Higgs boson can be determined from $H \rightarrow WW^*$ or $H \rightarrow ZZ^*$ decays. For example, the measurement of the Higgs decay to WW^* in the WW-fusion process determines:

$$\sigma(H\nu_e \bar{\nu}_e) \times BR(H \rightarrow WW^*) \propto \frac{g_{HWW}^4}{\Gamma_H},$$

and thus the total width can be determined utilising the model-independent measurement of g_{HWW} . In practice, a fit (see Section 11) is performed to all of the experimental measurements involving the Higgs boson couplings.

3.4 Overview of Higgs Measurements at $\sqrt{s} > 1$ TeV

For CLIC operation above 1 TeV, the large number of Higgs bosons produced in the WW-fusion process allow relative couplings of the Higgs boson to the W and Z bosons to be determined at the $\mathcal{O}(1\%)$ level. These measurements provide a strong test of the SM prediction for:

$$g_{HWW}/g_{HZZ} = \cos^2 \theta_W,$$

where θ_W is the weak-mixing angle. Furthermore, the exclusive Higgs decay modes can be studied with significantly higher precision than at $\sqrt{s} = 350$ GeV. For example, CLIC operating at 3 TeV would yield a statistical precision of 1.5 % on the ratio g_{Hcc}/g_{Hbb} , providing a direct comparison of the SM coupling predictions for up-type (charge +2/3) and

down-type (charge $-1/3$) quarks. In the context of the model-independent measurements of the Higgs branching ratios, the measurement of $\sigma(H\nu_e \bar{\nu}_e) \times BR(H \rightarrow WW^*)$ is particularly important. For CLIC operation at $\sqrt{s} \approx 1.4$ TeV, the large number of events allows this cross section to be determined with a precision of 1.5 % (see Section 6.3). When combined with the measurements at $\sqrt{s} \approx 350$ GeV, this places a strong constraint on Γ_H .

Although the WW-fusion process has the largest cross section for Higgs production above 1 TeV, other processes are also important. For example, measurements of the ZZ-fusion process provide further constraints on the g_{HZZ} coupling. Moreover, CLIC operation at $\sqrt{s} = 1.4$ TeV enables a determination of the top Yukawa coupling from the process $e^+e^- \rightarrow t\bar{t}H \rightarrow bW^+ \bar{b}W^- H$ with a precision of 4.5 % (see Section 8). Finally, the self-coupling of the Higgs boson at the HHH vertex is measurable in 1.4 TeV and 3 TeV operation. In the SM, the Higgs boson originates from a doublet of complex scalar fields ϕ described by the potential:

$$V(\phi) = \mu^2 \phi^\dagger \phi + \lambda (\phi^\dagger \phi)^2,$$

where μ and λ are the parameters of the Higgs potential. After spontaneous symmetry breaking, this form of the potential gives rise to a trilinear Higgs self-coupling of strength proportional to λv , where v is the vacuum expectation value of the Higgs potential.

The measurement of the strength of the Higgs self-coupling therefore provides direct access to the coupling λ assumed in the Higgs mechanism. This measurement is an essential part of experimentally establishing the Higgs mechanism as described by the SM. For $m_H = 126$ GeV, the measurement of the Higgs boson self-coupling at the LHC will be extremely challenging even with 3000 fb^{-1} of data (see for example [22]). At a linear collider, the trilinear Higgs self-coupling can be measured through the $e^+e^- \rightarrow ZHH$ and $e^+e^- \rightarrow HH\nu_e \bar{\nu}_e$ processes. The achievable precision has been studied for the $e^+e^- \rightarrow ZHH$ process at $\sqrt{s} = 500$ GeV in the context of the ILC, where the results show that a very large integrated luminosity is required [23]. For this reason, the most favourable channel for the measurement of the Higgs self-coupling is the $e^+e^- \rightarrow HH\nu_e \bar{\nu}_e$ process at $\sqrt{s} \geq 1$ TeV. Here the sensitivity increases with increasing centre-of-mass energy and the measurement of the Higgs boson self-coupling (see Section 9) forms a central part of the CLIC Higgs physics programme. Ultimately a precision of approximately 10 % on λ can be achieved.

4 Event Generation, Detector Simulation and Reconstruction

The results presented in this paper are based on detailed Monte Carlo (MC) simulation studies including the generation of a complete set of relevant SM background processes, full GEANT4 [24, 25] based simulations of the CLIC detector concepts and a full reconstruction of the simulated events.

4.1 Event Generation

Because of the presence of beamstrahlung photons in the colliding electron and positron beams, it is necessary to generate MC event samples for e^+e^- , $e^+\gamma$, γe^- and $\gamma\gamma$ interactions. The main physics backgrounds, with up to six particles in the final state, were generated using the WHIZARD 1.95 [19] program. In all cases the expected energy spectra for the CLIC beams, including the effects from beamstrahlung and the intrinsic machine energy spread, were used for the initial-state electrons, positrons and beamstrahlung photons. In addition, low- Q^2 processes with quasi-real photons were described using the Weizsäcker-Williams approximation as implemented in WHIZARD. The process of fragmentation and hadronisation was simulated using PYTHIA 6.4 [26] with a parameter set that was tuned to OPAL e^+e^- data recorded at LEP (see [11] for details). The decays of τ leptons were simulated using TAUOLA [27]. The mass of the Higgs boson was taken to be $126\text{ GeV}^{\text{ii}}$ and the decays of the Higgs boson were simulated using PYTHIA with the branching fractions listed in [20]. The events from the different Higgs production channels were simulated separately. To avoid double counting, the Higgs boson mass was set to 12 TeV in the generation of the background samples. Monte Carlo samples for the measurement of the top Yukawa coupling measurement (see Section 8) with eight final-state fermions were obtained using the PHYSSIM [28] package; again PYTHIA was used for fragmentation, hadronisation and the Higgs boson decays.

4.2 Simulation and Reconstruction

The GEANT4 detector simulation toolkits MOKKA [29] and SLIC [30] were used to simulate the detector response to the generated events in the CLIC_ILD and CLIC_SiD concepts, respectively. The QGSP_BERT physics list was used to model the hadronic interactions of particles in the detectors. The digitisation, namely the translation of the raw simulated energy deposits into detector signals, and the event

reconstruction were performed using the MARLIN [31] and org.lcsim [32] software packages. Particle flow reconstruction was performed using PANDORAPFA [15, 16, 33]. Vertex reconstruction and heavy flavour tagging are performed using the LCFIPLUS program [34]. The detailed training of the multivariate classifiers for the flavour tagging was performed separately for each centre-of-mass energy and each final state of interest.

Because of the 0.5 ns bunch spacing in the CLIC beams, the pile-up of beam-induced backgrounds can impact the event reconstruction and needs to be accounted for. Realistic levels of pile-up from the most important beam-induced background, the $\gamma\gamma \rightarrow \text{hadrons}$ process, was included in all the simulated event samples to ensure that the impact on the event reconstruction was correctly modelled. The $\gamma\gamma \rightarrow \text{hadrons}$ events were simulated separately and a randomly chosen subset corresponding to 60 bunch crossings was superimposed on the physics event before the digitisation step [35]. For the $\sqrt{s} = 350\text{ GeV}$ samples, where the background rates are lower, 300 bunch crossings were overlaid on the physics event. The impact of the background is small at $\sqrt{s} = 350\text{ GeV}$, and is most significant at $\sqrt{s} = 3\text{ TeV}$, where approximately 1.2 TeV of energy is deposited in the calorimeters in a time window of 10 ns . A dedicated reconstruction algorithm was developed to identify and remove approximately 90% of this out-of-time background, using criteria based on the reconstructed transverse momentum p_T of the particle and the truncated mean calorimeter cluster time. A more detailed description can be found in [11].

Jet finding was performed using the FASTJET [36] package. Because of the presence of pile-up from $\gamma\gamma \rightarrow \text{hadrons}$, it was found that the Durham [37] algorithm employed at LEP is not optimal for CLIC studies. Instead, the hadron-collider inspired k_t algorithm [38, 39], with the distance parameter R based on $\Delta\eta$ and $\Delta\phi$, was found to give better performance since it increases distances in the forward region, thus reducing the clustering of the (predominantly low transverse momentum) background particles together with those from the hard e^+e^- interaction. The particles clustered into the beam jets are likely to have originated from beam-beam backgrounds, and are removed from the event. As a result of using the R -based k_t algorithm, the impact of the pile-up from $\gamma\gamma \rightarrow \text{hadrons}$ is largely mitigated, even without the timing and momentum cuts described above. Further details are given in [11]. The choice of R was optimised separately for different analyses. In many of the following studies events are forced into a particular N -jet topology. The variable y_{ij} is the smallest k_t distance when combining j jets to $i = (j - 1)$ jets. These resolution parameters are widely used in a number of event selections, allowing events to be categorised into topologically different final states. In several studies it was found to be advantageous first to ap-

ⁱⁱ A Higgs boson of 125 GeV was used in the generation of $e^+e^- \rightarrow t\bar{t}H$.

ply the hadron-collider inspired k_t algorithm to remove the background clustered in the beam jets and then to recluster the remaining event using the Durham algorithm.

The event simulation and reconstruction of the large data samples used in this study was performed using the iLCDIRAC [40, 41] grid production tools.

5 Higgs Production at $\sqrt{s}=350$ GeV

The study of the Higgsstrahlung process is central to the precision Higgs physics programme at any future electron-positron collider. This section describes the physics potential from studies of $e^+e^- \rightarrow ZH$ at $\sqrt{s} = 350$ GeV and, in particular, focuses on the model-independent measurements of ZH production from the kinematic properties of the Z decay products. Complementary information obtained from Higgs production through WW-fusion at $\sqrt{s} = 350$ GeV is also presented. All analyses at $\sqrt{s} = 350$ GeV described in the following have used the CLIC_ILD detector model.

5.1 Recoil Mass Measurements of $e^+e^- \rightarrow ZH$

In the process $e^+e^- \rightarrow ZH$, it is possible to efficiently identify $Z \rightarrow e^+e^-$ and $Z \rightarrow \mu^+\mu^-$ decays, with a selection efficiency that is essentially independent of the H decay mode. The four-momentum of the system (the Higgs boson) recoiling against the Z can be obtained from $E_{\text{rec}} = \sqrt{s} - E_Z$ and $\mathbf{p}_{\text{rec}} = -\mathbf{p}_Z$, and the recoil mass, m_{rec} , will peak sharply around m_H . The recoil mass analysis for leptonic decays of the Z is described in Section 5.1.1. Whilst these measurements provide a clean model-independent probe of ZH production, they are limited by the relatively small leptonic branching ratios of the Z. Studies of ZH production with $Z \rightarrow q\bar{q}$ are inherently less clean, but are statistically more powerful. Despite the challenges related to the reconstruction of hadronic Z decays in the presence of various Higgs decay modes, a precise and nearly model-independent probe of ZH production can be obtained by analysing the recoil mass in hadronic Z decays, as detailed in Section 5.1.3. When all these measurements are taken together, a model-independent measurement of the g_{HZZ} coupling constant with a precision of $< 1\%$ can be inferred.

5.1.1 Leptonic Decays: $Z \rightarrow e^+e^-$ and $Z \rightarrow \mu^+\mu^-$

The signature for $e^+e^- \rightarrow ZH$ production with $Z \rightarrow e^+e^-$ or $Z \rightarrow \mu^+\mu^-$ is a pair of oppositely charged high- p_T leptons, with an invariant mass consistent with that of the Z

boson, $m_{ll} \approx m_Z$, and a recoil mass, calculated from the four-momenta of the leptons alone, consistent with the Higgs mass, $m_{\text{rec}} \approx m_H$ [42]. Consequently, the $\mu^+\mu^-X$ and e^+e^-X final states, where X represents any decay mode of the Higgs boson, can be identified using the properties of the observed leptons alone. Backgrounds from two-fermion final states $e^+e^- \rightarrow l^+l^-$ ($l = e, \mu, \tau$) are trivial to remove. The dominant backgrounds are from four-fermion processes with final states consisting of a pair of oppositely-charged leptons and any other possible fermion pair. For both the $\mu^+\mu^-X$ and e^+e^-X channels, the total four-fermion background cross section is approximately one thousand times greater than the signal cross section.

The event selection, consisting of a set of preselection cuts and a multivariate analysis, was studied using fully simulated MC events. The preselection required at least one negatively and one positively charged lepton of the lepton flavour of interest (muons or electrons) with an invariant mass loosely consistent with the mass of the Z boson, $40 < m_{ll} \text{ (GeV)} < 126$. For signal events the lepton identification efficiencies are 99% for muons and 90% for electrons. Backgrounds from two-fermion processes were essentially eliminated by requiring that the di-lepton system had a large transverse momentum, $p_T > 60$ GeV. Four-fermion backgrounds are suppressed by requiring that the recoil mass lies between $95 < m_{\text{rec}} \text{ (GeV)} < 290$. The lower bound suppresses $e^+e^- \rightarrow ZZ$ production. The upper bound is significantly greater than the Higgs boson mass, to allow for the possibility of ZH production with ISR or significant beamstrahlung, which, in the recoil mass analysis, results in a tail to the recoil mass distribution since the effective centre-of-mass energy of the e^+e^- collision, $\sqrt{s'}$, is lower than \sqrt{s} , which means that the energy (and consequently the mass) of the recoiling system, $E_{\text{rec}} = \sqrt{s} - E_Z$, is over-estimated.

Events passing the preselection cuts were categorised using a multivariate analysis of seven discriminating variables: the transverse momentum (p_T) and invariant mass (m_{ll}) of the candidate Z as reconstructed from the di-lepton system; the cosine of the polar angle ($|\cos\theta|$) of the candidate Z; the acollinearity and acoplanarity of the leptons; the imbalance between the transverse momenta of the two selected leptons ($p_{T1} - p_{T2}$); and the transverse momentum of the highest energy photon in the event. The event selection employed a Boosted Decision Tree (BDT) as implemented in TMVA [43]. The resulting selection efficiencies are summarised in Table 4. For both investigated final states, the number of selected background events is less than twice the number of selected signal events. The impact of the background can be reduced further using the recoil mass distribution, which is achieved by a fit here.

The fit to the recoil mass distribution of the selected events (in both the $Z \rightarrow e^+e^-$ and $Z \rightarrow \mu^+\mu^-$ channels) can be used

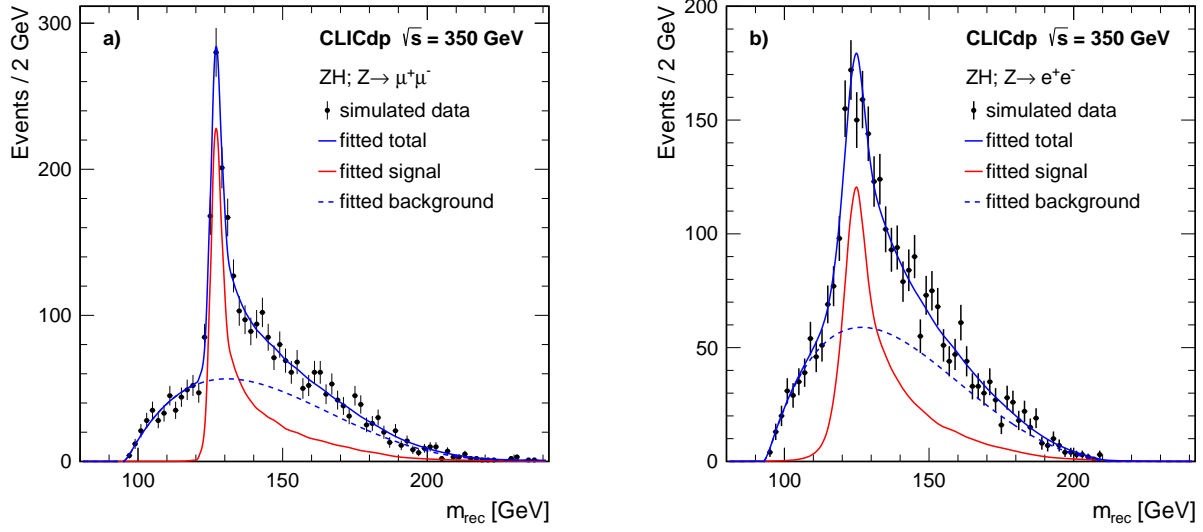


Fig. 6: Reconstructed recoil mass distributions of $e^+e^- \rightarrow ZH$ events at $\sqrt{s} = 350$ GeV, where $ZH \rightarrow \mu^+\mu^-X$ (a) and $ZH \rightarrow e^+e^-X$ with bremsstrahlung recovery (b). All distributions are normalised to an integrated luminosity of 500 fb^{-1} .

Process	σ/fb	ϵ_{preSEL}	ϵ_{BDT}	N_{BDT}
$ZH; Z \rightarrow \mu^+\mu^-$	4.6	83.8 %	54.1 %	1253
$\mu^+\mu^-\bar{f}f$	4753	0.8 %	<0.01 %	1905
$ZH; Z \rightarrow e^+e^-$	4.6	73.3 %	37.1 %	858
$e^+e^-\bar{f}f$	4847	1.2 %	<0.1 %	1558

Table 4: Preselection and selection efficiencies for the ZH signal and most important background processes in the leptonic recoil mass analysis. The numbers of events correspond to 500 fb^{-1} at $\sqrt{s} = 350$ GeV.

to extract measurements of the ZH production cross section and the Higgs boson mass. The shape of the background contribution was parameterised using a fourth order polynomial and the shape of the signal distribution was modelled using Simplified Kernel Estimation [44–46], which provided a description of the ZH recoil mass distribution in which the Higgs mass subsequently could be varied. To determine the accuracy with which the Higgs mass and the number of signal events (and hence the ZH production cross section) can be measured, 1000 simulated data samples were produced. Each test sample was created by adding the high statistics selected signal sample (scaled to the correct normalisation) to the smooth fourth-order polynomial background, then applying Poissonian fluctuations to individual bins of the resulting smooth distribution to create a representative 500 fb^{-1} data sample. Each of the 1000 simulated data samples created in this way was fitted allowing the Higgs mass, the signal normalisation and the background normalisation to vary. Figure 6a displays the results of fitting a typical test

sample for the $\mu^+\mu^-X$ channel, while Figure 6b displays the results for the e^+e^-X channel. In the e^+e^-X channel fits were performed with and without applying an algorithm to recover bremsstrahlung photons. The resulting measurement precisions for the ZH cross section and the Higgs boson mass are summarised in Table 5. In the e^+e^-X channel, the bremsstrahlung recovery leads to a moderate improvement on the expected precision for the cross section measurement and a similar degradation in the expected precision for the mass determination, because it significantly increases the number of events in the peak of the recoil mass distribution, but also increases the width of this peak. For an integrated luminosity of 500 fb^{-1} at $\sqrt{s} = 350$ GeV, the combined precision on the Higgs boson mass is:

$$\Delta(m_H) = 110\text{ MeV},$$

and the combined precision on the ZH cross section is:

$$\frac{\Delta\sigma(\text{ZH})}{\sigma(\text{ZH})} = 3.8\%.$$

The expected precision with (without) bremsstrahlung recovery in the e^+e^-X channel was used in the combination for the mass (cross section).

5.1.2 Invisible Higgs Decays

The above recoil mass analysis of leptonic decays of the Z boson in $e^+e^- \rightarrow ZH$ events provides a measurement of the Higgsstrahlung cross section, independent of the Higgs boson decay model. The recoil mass technique can also be used to search for BSM decay modes of the Higgs boson

Channel	Quantity	Precision
$\mu^+\mu^-X$	m_H	122 MeV
	$\sigma(ZH)$	4.72 %
e^+e^-X	m_H	278 MeV
	$\sigma(ZH)$	7.21 %
e^+e^-X + bremsstrahlung recovery	m_H	359 MeV
	$\sigma(ZH)$	6.60 %

Table 5: Summary of measurement precisions from the leptonic recoil mass analyses in the $\mu^+\mu^-X$ and e^+e^-X channels for an integrated luminosity of 500fb^{-1} at 350GeV .

into long-lived neutral “invisible” final states. At an e^+e^- collider, a search for invisible Higgs decays is possible by identification of $e^+e^- \rightarrow ZH$ events with a visible $Z \rightarrow q\bar{q}$ decay and missing energy. Such events would typically produce a clear two-jet topology with invariant mass consistent with m_Z , significant missing energy and a recoil mass corresponding to the Higgs mass. Higgsstrahlung events with leptonic Z decays have not been investigated, as no competitive result is expected due to the small branching ratios for $Z \rightarrow e^+e^-$ and $Z \rightarrow \mu^+\mu^-$ compared to $Z \rightarrow q\bar{q}$.

To identify candidate invisible Higgs decays, a loose preselection is imposed requiring: i) a clear two-jet topology, defined by $\log_{10}(y_{23}) < -2.0$ and $\log_{10}(y_{34}) < -3.0$, using the minimal k_t distances discussed in Section 4.2; ii) a di-jet invariant mass consistent with the Z mass, $84\text{GeV} < m_{q\bar{q}} < 104\text{GeV}$; and iii) the reconstructed momentum of the candidate Z boson pointing away from the beam direction, $|\cos\theta_Z| < 0.7$. After the preselection, a BDT multivariate analysis technique was applied using the TMVA package [43] to further separate the invisible Higgs signal from the SM background. In addition to $m_{q\bar{q}}$, $|\cos\theta_Z|$ and $\log_{10}(y_{23})$, four other discriminating variables were employed: m_{rec} , the recoil mass of the invisible system recoiling against the observed Z boson; $|\cos\theta_q|$, the decay angle of one of the quarks in the Z rest frame, relative to the direction of flight of the Z boson; p_T , the magnitude of the transverse momentum of the Z boson; E_{vis} , the visible energy in the event. As an example, Figure 7 shows the recoil mass distribution for the simulated invisible Higgs decays and the total SM background. The reconstructed recoil mass for events with invisible Higgs decays peaks near m_H . The cut applied on the BDT output was chosen such that it minimises the statistical uncertainty on the cross section for invisible Higgs decays.

In the case where the branching ratio to BSM invisible final states is zero (or very small), the uncertainty on the invisible branching ratio is determined by the statistical fluctuations on the background after the event selection:

$$\Delta BR(H \rightarrow \text{invis.}) = \frac{\sqrt{b}}{s(100\%)},$$

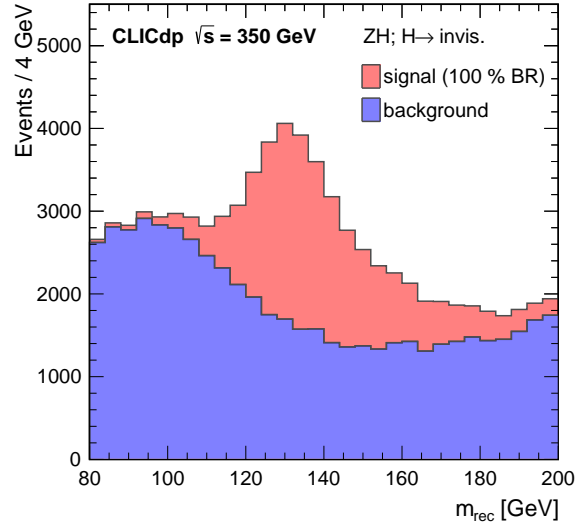


Fig. 7: Reconstructed recoil mass distributions of $e^+e^- \rightarrow ZH$ events at $\sqrt{s} = 350\text{GeV}$, showing the $H \rightarrow \text{invis.}$ signal assuming $BR(H \rightarrow \text{invis.}) = 100\%$ and SM backgrounds as stacked histograms. The distributions are normalised to an integrated luminosity of 500fb^{-1} .

where b is the expected number of selected SM background events and $s(100\%)$ is the expected number of selected Higgsstrahlung events assuming all Higgs bosons decay invisibly, i.e. $BR(H \rightarrow \text{invis.}) = 100\%$. Table 6 summarises the invisible Higgs decay event selection; the dominant background processes arise from the final states $q\bar{q}l\nu$ and $q\bar{q}\nu\bar{\nu}$. The resulting one sigma uncertainty on $BR(H \rightarrow \text{invis.})$ is 0.57 % (in the case where the invisible Higgs branching ratio is small) and the corresponding 90 % C.L. upper limit (500fb^{-1} at $\sqrt{s} = 350\text{GeV}$) on the invisible Higgs branching ratio in the modified frequentist approach [47] is:

$$BR(H \rightarrow \text{invis.}) < 0.97\% \quad \text{at } 90\% \text{ C.L.}$$

It should be noted that the SM Higgs decay chain $H \rightarrow ZZ^* \rightarrow \nu\bar{\nu}\nu\bar{\nu}$ has a combined branching ratio of 0.1 % and is not measurable.

5.1.3 Hadronic Decays: $Z \rightarrow q\bar{q}$

In the process $e^+e^- \rightarrow ZH$ it is possible to cleanly identify $Z \rightarrow e^+e^-$ and $Z \rightarrow \mu^+\mu^-$ decays regardless of the decay mode of the Higgs boson and, consequently, the selection efficiency is almost independent of the Higgs decay mode. In contrast, for $Z \rightarrow q\bar{q}$ decays, the selection efficiency will show a stronger dependence on the Higgs decay mode [48]. For example, $e^+e^- \rightarrow (Z \rightarrow q\bar{q})(H \rightarrow b\bar{b})$ events will consist of four jets and the reconstruction of the Z boson will be complicated by ambiguities in associations of particles with

Process	σ/fb	ϵ_{presel}	$\epsilon_{\text{BDT}>0.088}$	$N_{\text{BDT}>0.088}$
$q\bar{q}l\nu$	5914	<0.7 %	<0.1 %	900
$q\bar{q}\nu\bar{\nu}$	325	16.7 %	1.5 %	2414
ZH (SM decays)	93.4	0.2 %	<0.1 %	21
$H \rightarrow \text{invis.}$		41.0 %	20.7 %	9956

Table 6: Summary of the invisible Higgs decay event selection at $\sqrt{s} = 350\text{GeV}$, giving the raw cross sections, preselection efficiency, overall selection efficiency for a BDT cut of $\text{BDT} > 0.088$ and the expected numbers of events passing the event selection for an integrated luminosity of 500fb^{-1} . For the invisible Higgs decay signal the number of selected events corresponds to a BR of 100 %. Contributions from all other backgrounds are found to be negligibly small.

jets and the three-fold ambiguity in associating four jets to the hadronic decays of the Z and H. For this reason, it is much more difficult to construct a selection based only on the reconstructed $Z \rightarrow q\bar{q}$ decay that has a selection efficiency independent of the Higgs decay mode. The strategy adopted is to first reject events consistent with a number of clear background topologies using the information from the whole event; and then identify $e^+e^- \rightarrow (Z \rightarrow q\bar{q})H$ events solely based on the properties from the candidate $Z \rightarrow q\bar{q}$ decay.

The $(Z \rightarrow q\bar{q})H$ event selection proceeds in three separate stages. In the first stage, to allow for possible BSM invisible Higgs decay modes, events are divided into candidate visible Higgs decays and candidate invisible Higgs decays, in both cases produced along with a $Z \rightarrow q\bar{q}$. Events are categorised as potential visible Higgs decays if they are not compatible with a clear two-jet topology:

$$- \log_{10}(y_{23}) > -2.0 \text{ or } \log_{10}(y_{34}) > -3.0.$$

All other events are considered as candidates for an invisible Higgs decay analysis, based on that described in [Section 5.1.2](#), although with looser requirements to make the overall analysis more inclusive.

Preselection cuts then reduce the backgrounds from large cross section processes such as $e^+e^- \rightarrow q\bar{q}$ and $e^+e^- \rightarrow q\bar{q}q\bar{q}$. The preselection variables are formed by forcing each event into three, four and five jets. In each case, the best candidate for being a hadronically decaying Z boson is chosen as the jet pair giving the di-jet invariant mass ($m_{q\bar{q}}$) closest to m_Z , only considering jets with more than three charged particles. The invariant mass of the system recoiling against the Z boson candidate, m_{rec} , is calculated assuming $E_{\text{rec}} = \sqrt{s} - E_{q\bar{q}}$ and $\mathbf{p}_{\text{rec}} = -\mathbf{p}_{q\bar{q}}$. In addition, the invariant mass of all the visible particles not originating from the candidate $Z \rightarrow q\bar{q}$ decay, m_{vis} is calculated. It is important to note that m_{vis} is only used to reject specific background topologies in the

preselection and is not used in the main selection as it will depend strongly on the type of Higgs decay. The preselection cuts are:

- $70 < m_{q\bar{q}} (\text{GeV}) < 110$ and $80 < m_{\text{rec}} (\text{GeV}) < 200$;
- the background from $e^+e^- \rightarrow q\bar{q}$ is suppressed by removing events with overall $p_T < 20\text{GeV}$ and either $|\cos \theta_{\text{mis}}| > 0.90$ or $\log_{10}(y_{34}) > -2.5$, where θ_{mis} is the polar angle of the missing momentum vector;
- events with little missing transverse momentum ($p_T < 20\text{GeV}$) are forced into four jets and are rejected if the reconstructed di-jet invariant masses (and particle types) are consistent with the expectations for $e^+e^- \rightarrow q\bar{q}l\bar{l}$, $e^+e^- \rightarrow ZZ \rightarrow q\bar{q}q\bar{q}$, $e^+e^- \rightarrow WW \rightarrow q\bar{q}q\bar{q}$.

The final step in the event selection is a multivariate analysis. In order not to bias the event selection efficiencies for different Higgs decay modes, only variables related to the candidate $Z \rightarrow q\bar{q}$ decay are used in the selection. Forcing the event into four jets is the right approach for $(Z \rightarrow q\bar{q})H$ events where the Higgs decays to two-body final states, but not necessarily for final states such as $H \rightarrow WW^* \rightarrow q\bar{q}q\bar{q}$, where there is the chance that one of the jets from the WW^* decay will be merged with one of the jets from the $Z \rightarrow q\bar{q}$, potentially biasing the selection against $H \rightarrow WW^*$ decays. To mitigate this effect, the Z candidate for the event selection can either be formed from the four-jet topology as described above, or can be formed from a jet pair after forcing the event into a five-jet topology. The latter case is only used when $\log_{10}(y_{45}) > -3.5$ and the five-jet reconstruction gives a better Z and H candidates than the four-jet reconstruction. Attempting to reconstruct events in the six-jet topology is not found to improve the overall analyses. Having chosen the best Z candidate in the event (from either the four-jet or five-jet reconstruction), it is used to form variables for the multivariate selection; information about the remainder of the event is not used.

A relative likelihood selection is used to classify all events passing the preselection cuts. Two event categories are considered: the $e^+e^- \rightarrow ZH \rightarrow q\bar{q}H$ signal and all non-Higgs background processes. The relative likelihood for an event being signal is defined as:

$$\mathcal{L} = \frac{L_{\text{signal}}}{L_{\text{signal}} + L_{\text{back}}},$$

where the individual absolute likelihood L for each event type is formed from normalised probability distributions $P_i(x_i)$ of the discriminating variables x_i for that event type:

$$L = \sigma_{\text{presel}} \times \prod_i P_i(x_i),$$

where σ_{presel} is the cross section after the preselection cuts. The discriminating variables used, all of which are based on

Process	σ/fb	ϵ_{presel}	$\epsilon_{\mathcal{L}>0.65}$	$N_{\mathcal{L}>0.65}$
$q\bar{q}$	25180	0.4 %	0.07 %	8525
$q\bar{q}l\nu$	5914	11.2 %	0.20 %	5767
$q\bar{q}q\bar{q}$	5847	3.8 %	0.49 %	14142
$q\bar{q}ll$	1704	1.5 %	0.22 %	1961
$q\bar{q}\nu\bar{\nu}$	325	0.6 %	0.04 %	60
$H\nu_e\bar{\nu}_e$	52	2.5 %	0.23 %	60
$ZH; Z \rightarrow q\bar{q}$	93	42.0 %	22.6 %	10568

Table 7: Summary of the $(Z \rightarrow q\bar{q})(H \rightarrow \text{vis.})$ event selection at $\sqrt{s} = 350\text{GeV}$, giving the raw cross sections, preselection efficiency, overall selection efficiency for a likelihood cut of $\mathcal{L} > 0.65$ and the expected numbers of events passing the event selection for an integrated luminosity of 500fb^{-1} .

the candidate $Z \rightarrow q\bar{q}$ decay, are: the 2D distribution of $m_{q\bar{q}}$ and m_{rec} ; the polar angle of the Z candidate, $|\cos \theta_Z|$; and the modulus of angle of jets from the Z decay relative to its direction after boosting into its rest frame, $|\cos \theta_q|$. The clearest separation between signal and background is obtained from $m_{q\bar{q}}$ and the recoil mass m_{rec} , as shown in Figure 8 for events passing the preselection. The signal is clearly peaked at $m_{q\bar{q}} \approx m_Z$ and $m_{\text{rec}} \approx m_H$. The use of 2D mass distributions accounts for the most significant correlations between the likelihood variables.

In this high-statistics limit, the fractional error on the number of signal events (where the Higgs decays to visible final states), s_{vis} , given a background b is:

$$\frac{\Delta s_{\text{vis}}}{s_{\text{vis}}} = \frac{\sqrt{s_{\text{vis}} + b}}{s_{\text{vis}}},$$

and this is minimised with the selection requirement $\mathcal{L} > 0.65$. The selection efficiencies and expected numbers of events for the signal dominated region, $\mathcal{L} > 0.65$, are listed in Table 7, corresponding to a fractional error on the number of signal events of 1.9%. By fitting the shape of the likelihood distribution to signal and background contributions, this uncertainty is reduced to:

$$\frac{\Delta s_{\text{vis}}}{s_{\text{vis}}} = 1.7\%.$$

5.1.4 Model-Independent ZH Cross Section

By combining the two analyses for ZH production where $Z \rightarrow q\bar{q}$ and the Higgs decays either to invisible final states (see Section 5.1.2) or to visible final states (see Section 5.1.3), it is possible to determine the absolute cross section for $e^+e^- \rightarrow ZH$ in an essentially model-independent manner:

$$\sigma(\text{ZH}) = \frac{\sigma_{\text{vis}} + \sigma_{\text{invis}}}{BR(Z \rightarrow q\bar{q})}.$$

Decay mode	$\Delta(BR)$	$\sigma^{\text{vis}} + \sigma^{\text{invis}}$ Bias
$H \rightarrow \text{invis}$	+5 %	-0.01 %
$H \rightarrow q\bar{q}$	+5 %	+0.05 %
$H \rightarrow WW^*$	+5 %	-0.18 %
$H \rightarrow ZZ^*$	+5 %	-0.30 %
$H \rightarrow \tau^+\tau^-$	+5 %	+0.60 %
$H \rightarrow \gamma\gamma$	+5 %	+0.79 %
$H \rightarrow Z\gamma$	+5 %	-0.74 %
$H \rightarrow WW^* \rightarrow q\bar{q}q\bar{q}$	+5 %	-0.49 %
$H \rightarrow WW^* \rightarrow q\bar{q}l\nu$	+5 %	+0.10 %
$H \rightarrow WW^* \rightarrow \tau\nu\tau\nu$	+5 %	-0.98 %

Table 8: Biases in the extracted $H(Z \rightarrow q\bar{q})$ cross section if the Higgs branching ratio to a specific final state is increased by 5 %, i.e. $BR(H \rightarrow X) \rightarrow BR(H \rightarrow X) + 0.05$.

Here a slightly modified version of the invisible Higgs analysis is employed. With the exception of the cuts on y_{23} and y_{34} , the invisible Higgs analysis employs the same preselection as for the visible Higgs analysis and a likelihood multivariate discriminant is used.

Since the fractional uncertainties (relative to the total cross section) on the visible and invisible cross sections are 1.7 % and 0.6 % respectively, the fractional uncertainty on the total cross section will be (at most) the quadrature sum of the two fractional uncertainties, namely 1.8 %. This measurement is only truly model-independent if the overall selection efficiencies are independent of the Higgs decay mode. For all final state topologies, the combined (visible + invisible) selection efficiency lies in the range 19 – 26 % regardless of the Higgs decay mode, covering a very wide range of event topologies. To assess the level of model independence, the Higgs decay modes in the MC samples are modified and the total (visible + invisible) cross section is extracted assuming the SM Higgs branching ratio. Table 8 shows the resulting biases in the extracted total cross section for the case when a $BR(H \rightarrow X) \rightarrow BR(H \rightarrow X) + 0.05$. Even for these very large modifications of the Higgs branching ratios over a wide range of final-state topologies, the resulting biases in the extracted total ZH cross section are less than 1 % (compared to the 1.8 % statistical uncertainty). However, such large deviations would have significant observable effects on the exclusive Higgs branching ratio analyses (at the LHC and CLIC) and it is concluded that the analysis can be considered to give an effectively model-independent measurement of the $(Z \rightarrow q\bar{q})H$ cross section (unless there are very large BSM effects on the Higgs branching ratios which would already be apparent).

Combining the model-independent measurements of the ZH cross section from $Z \rightarrow l^+l^-$ and $Z \rightarrow q\bar{q}$ gives an absolute

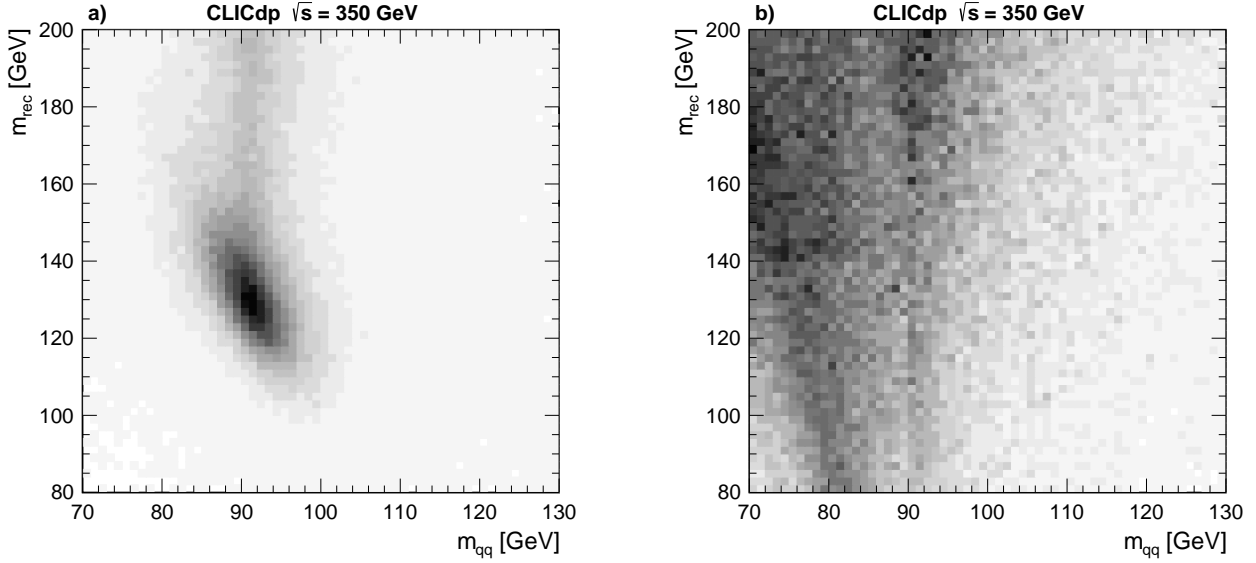


Fig. 8: Reconstructed di-jet invariant mass versus reconstructed recoil mass distributions for $ZH \rightarrow q\bar{q}X$ candidate events at $\sqrt{s} = 350 \text{ GeV}$, showing ZH signal (a) and all non-Higgs background (b) passing the preselection.

measurement of the ZH cross section with a precision of:

$$\frac{\Delta\sigma(\text{ZH})}{\sigma(\text{ZH})} = 1.65\%,$$

and, consequently, the absolute coupling of the H boson to the Z boson is determined to:

$$\frac{\Delta g_{\text{HZZ}}}{g_{\text{HZZ}}} = 0.8\%.$$

The hadronic recoil mass analysis was repeated assuming $\sqrt{s} = 250 \text{ GeV}$ and $\sqrt{s} = 420 \text{ GeV}$ [48]. Compared to $\sqrt{s} = 350 \text{ GeV}$, the sensitivity is significantly worse in both cases.

5.2 Exclusive Higgs Branching Ratio Measurements at $\sqrt{s} = 350 \text{ GeV}$

The previous section focussed on inclusive measurements of the $e^+e^- \rightarrow ZH$ production cross section, which provide a model-independent determination of the coupling at the HZZ vertex. In contrast, measurements of Higgs production and decay to exclusive final states, provides a determination of the product $\sigma(\text{ZH}) \times BR(\text{H} \rightarrow X)$, where X is a particular final state. This section focuses on the exclusive measurements of the Higgs decay branching ratios at $\sqrt{s} = 350 \text{ GeV}$. Higgs boson decays to $b\bar{b}$, $c\bar{c}$ and gg are studied in Section 5.2.1. The measurement of $\text{H} \rightarrow \tau^+\tau^-$ decays is described in Section 5.2.2, and the $\text{H} \rightarrow WW^*$ decay mode is described in Section 5.2.3.

5.2.1 $\text{H} \rightarrow b\bar{b}, c\bar{c}, gg$

As can be seen from Table 1, at $\sqrt{s} = 350 \text{ GeV}$ the $e^+e^- \rightarrow ZH$ (Higgsstrahlung) cross section is approximately four times larger than the $e^+e^- \rightarrow \text{H}\nu_e\bar{\nu}_e$ (mostly WW-fusion) cross section for unpolarised beams (or approximately a factor 2.5 with -80% electron beam polarisation). For Higgsstrahlung, the signature of $\text{H} \rightarrow b\bar{b}, c\bar{c}, gg$ events depends on the Z decay mode, resulting in three distinct final state topologies, jjjj, jjll, and jjvv, where j represents a quark or gluon jet from the Z or H decay. It should be noted that the jjvv final state contains approximately equal contributions from Higgsstrahlung and WW-fusion events, although the event kinematics are very different.

To maximise the statistical power of the $\text{H} \rightarrow b\bar{b}, c\bar{c}, gg$ branching ratio measurements, two topologies are considered: four jets and two jets plus missing momentum (from the unobserved neutrinos). All events are reconstructed assuming both topologies and the decision for one category is performed at a later stage of the event selection procedure described below. The impact of Higgsstrahlung events with leptonic Z decays is found to be negligible. To minimize the impact of ISR on the jet reconstruction, photons with a reconstructed energy higher than 15 GeV are removed from the events first.

The hadronic final states are reconstructed using the Durham algorithm. For the four-jet topology, the most probable Z and H candidates are selected by choosing the jet combination that minimises:

$$\chi^2 = (m_{ij} - m_{\text{H}})^2 / \sigma_{\text{H}}^2 + (m_{kl} - m_{\text{Z}})^2 / \sigma_{\text{Z}}^2,$$

Process	σ/fb	ϵ_{BDT} , classified as		N_{BDT} , classified as	
		Hv $\bar{\nu}$	Hq \bar{q}	Hv $\bar{\nu}$	Hq \bar{q}
$e^+e^- \rightarrow \text{Hv}\bar{\nu}; \text{H} \rightarrow b\bar{b}$	28.9	55.0 %	0 %	8000	0
$e^+e^- \rightarrow \text{Hv}\bar{\nu}; \text{H} \rightarrow c\bar{c}$	1.46	51.0 %	0 %	372	0
$e^+e^- \rightarrow \text{Hv}\bar{\nu}; \text{H} \rightarrow g\bar{g}$	4.37	58.0 %	0 %	1270	0
$e^+e^- \rightarrow \text{Hv}\bar{\nu}; \text{H} \rightarrow \text{other}$	17.8	6.1 %	0 %	513	0
$e^+e^- \rightarrow \text{Hq}\bar{q}; \text{H} \rightarrow b\bar{b}$	52.3	0 %	42.3 %	0	11100
$e^+e^- \rightarrow \text{Hq}\bar{q}; \text{H} \rightarrow c\bar{c}$	2.64	0 %	32.8 %	0	434
$e^+e^- \rightarrow \text{Hq}\bar{q}; \text{H} \rightarrow g\bar{g}$	7.92	0 %	37.4 %	0	1480
$e^+e^- \rightarrow \text{Hq}\bar{q}; \text{H} \rightarrow \text{other}$	30.5	12.6 %	0.12 %	20	1920
$e^+e^- \rightarrow q\bar{q}\nu\bar{\nu}$	325	1.3 %	0 %	2110	0
$e^+e^- \rightarrow q\bar{q}l\nu$	5910	0.07 %	0.002 %	2090	60
$e^+e^- \rightarrow q\bar{q}ll$	1700	0.012 %	0.01 %	104	89
$e^+e^- \rightarrow q\bar{q}q\bar{q}$	5530	0.01 %	0.36 %	30	9990
$e^+e^- \rightarrow q\bar{q}$	24400	0.01 %	0.093 %	1230	11400

Table 9: Summary of the expected numbers of events for the different Higgs and non-Higgs final states passing the hadronic Higgs decay signal selection for 500fb^{-1} at $\sqrt{s} = 350\text{GeV}$ (unpolarised beams). No preselection is applied in this analysis.

where m_{ij} and m_{kl} are the invariant masses of the jet pairs used to reconstruct the Higgs and Z boson candidates, respectively, and $\sigma_{\text{H,Z}}$ are the estimated invariant mass resolutions for Higgs and Z boson candidates. In the case of the two jets plus missing energy final state, either from ZH with $Z \rightarrow \nu\bar{\nu}$ or from $\text{Hv}\bar{\nu}$, the event is clustered into two jets forming the H candidate.

To help veto backgrounds with leptonic final states, isolated electrons or muons with $E > 10\text{GeV}$ are identified with the additional requirement that there should be less than 20GeV of energy from other particles within a cone with an opening angle of 20° around the lepton direction. All events are then classified by BDTs with gradient boost using reconstructed kinematic variables from each of the two event topology hypotheses described above. The variables used include jet energies, event shape variables (such as thrust and sphericity), the masses of H and Z candidates as well as their decay angles and transverse momenta, and the number of isolated leptons in the final state. The total number of variables is about 50, which is larger compared to other studies presented in this paper, because each event is reconstructed assuming two different final state configurations and information from the H candidate decay can be included here in contrast to the recoil mass analysis described in Section 5.1.

Two separate BDT classifiers are used, one for each signal final state (Hq \bar{q} and Hv $\bar{\nu}$), irrespective of the nature of the hadronic Higgs decay mode. The non-Higgs background channels, dominated by the two-fermions final state $q\bar{q}$, and the four-fermion final states $q\bar{q}\nu\bar{\nu}$, $q\bar{q}l\nu$, $q\bar{q}ll$ and $q\bar{q}q\bar{q}$ as well as other Higgs decay modes are taken as background for both classifiers. In addition, the other signal mode is included in the background for a given classifier. The training is performed using a dedicated training sample, simultane-

ously training both classifiers. At this point, no flavour tagging information is used.

Each event is evaluated with both classifiers. An event is only accepted if exactly one of the signal classifiers is above a positive threshold and the other classifier is below a corresponding negative threshold. The event is then tagged as a candidate for the corresponding signal process. If none of the classifiers passes the selection threshold, the event is considered as background and is rejected from the analysis. The number of events for which both signal classifiers are above the positive threshold is negligible. Such events with unclear final state classification are rejected from the analysis. Table 9 summarises the classification of all events into the two signal categories, with event numbers based on an integrated luminosity of 500fb^{-1} .

The second stage of the analysis is to measure the contributions of the hadronic Higgs decays into the $\text{H} \rightarrow b\bar{b}$, $\text{H} \rightarrow c\bar{c}$ and $\text{H} \rightarrow g\bar{g}$ exclusive final states, separated in the two production modes Higgsstrahlung and WW-fusion. This is achieved by a multi-dimensional template fit using flavour tagging information and, in the case of the Hv $\bar{\nu}$ final state, the transverse momentum of the Higgs candidate.

The jets forming the Higgs candidate are classified with the LCFIPLUS flavour tagging package. Each jet pair is assigned a $b\bar{b}$ likelihood and a $c\bar{c}$ likelihood:

$$b\bar{b} \text{ likelihood} = \frac{b_1 b_2}{b_1 b_2 + (1 - b_1)(1 - b_2)},$$

$$c\bar{c} \text{ likelihood} = \frac{c_1 c_2}{c_1 c_2 + (1 - c_1)(1 - c_2)},$$

where b_1 and b_2 (c_1 and c_2) are the b-tag (c-tag) values obtained for the two jets forming the Higgs candidate.

The resulting two-dimensional distributions of the $b\bar{b}$ and $c\bar{c}$ likelihoods in Hq \bar{q} events are shown in Figure 9, where sep-

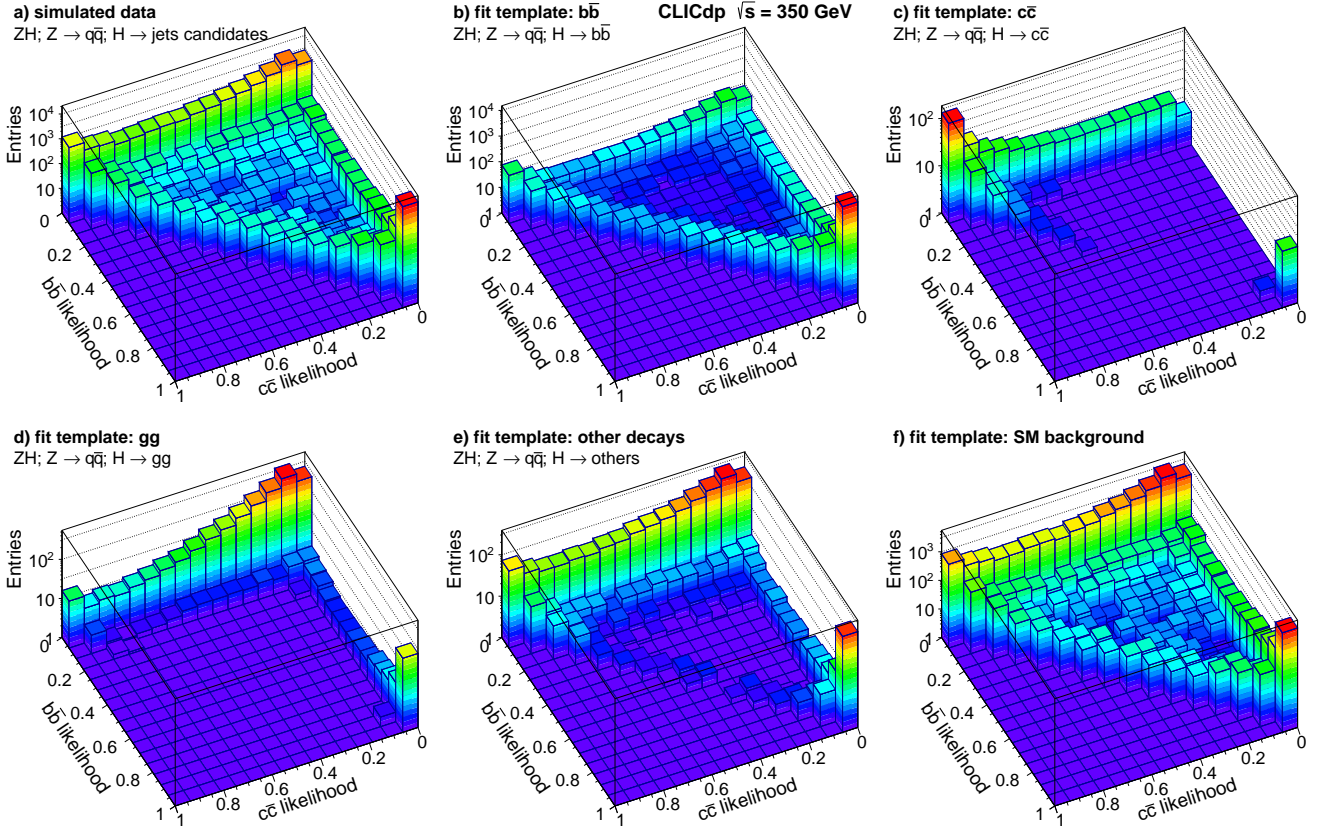


Fig. 9: $b\bar{b}$ likelihood versus $c\bar{c}$ likelihood distributions for $e^+e^- \rightarrow ZH$ events at $\sqrt{s} = 350\text{ GeV}$, for (a) all events and for the different event classes: (b) $H \rightarrow b\bar{b}$, (c) $H \rightarrow c\bar{c}$, (d) $H \rightarrow gg$, background from (e) other Higgs decays and (f) non-Higgs SM background. All distributions are normalised to an integrated luminosity of 500 fb^{-1} .

aration between the different event categories can be seen. These distributions form the templates used to determine the contribution of the different signal categories for the $Hq\bar{q}$ final states.

Signal and background templates as described above are also obtained for the $H\nu\bar{\nu}$ final state, which has roughly equal contributions from the Higgsstrahlung and the WW-fusion process. In addition to the separation into the different signal and background final states as in the $Hq\bar{q}$ case, a separation into the two production processes is required. This is achieved by adding an additional third dimension to the templates, given by the transverse momentum distribution of the Higgs candidate. This exploits the fact that this variable is substantially different for Higgsstrahlung and WW-fusion events as illustrated in Figure 10 for events with a high $b\bar{b}$ likelihood which provide a high signal purity. Here, the Higgsstrahlung and WW-fusion contributions are shown separately.

The contributions from events with $H \rightarrow b\bar{b}$, $H \rightarrow c\bar{c}$ and $H \rightarrow gg$ decays, separated by production mode, are extracted in a template fit maximizing the combined likelihood of the

$Hq\bar{q}$ and $H\nu\bar{\nu}$ templates describing the simulated data distribution. For this fit, the normalisations of the contributions from other Higgs decays and the non-Higgs events are fixed and expected to be provided by other measurements.

The results of the above analysis are summarised in Table 10, giving the statistical uncertainties of the various $\sigma \times BR$ measurements. Since the parameters in this analysis are determined in a combined extraction from overlapping distributions, the results are correlated. In particular the Higgsstrahlung and WW-fusion results for the same final states show sizeable anti-correlations, as large as -38% for the cases of $H \rightarrow c\bar{c}$ and $H \rightarrow gg$. These correlations are taken into account in the global fits described in Section 11.

5.2.2 $H \rightarrow \tau^+\tau^-$

Because of the neutrino(s) produced in τ decays, the signature for $H \rightarrow \tau^+\tau^-$ is less distinct than that for other decay modes. The invariant mass of the visible decay products of the $\tau^+\tau^-$ system will be less than m_H , and it is difficult to identify $H \rightarrow \tau^+\tau^-$ decays from the WW-fusion process

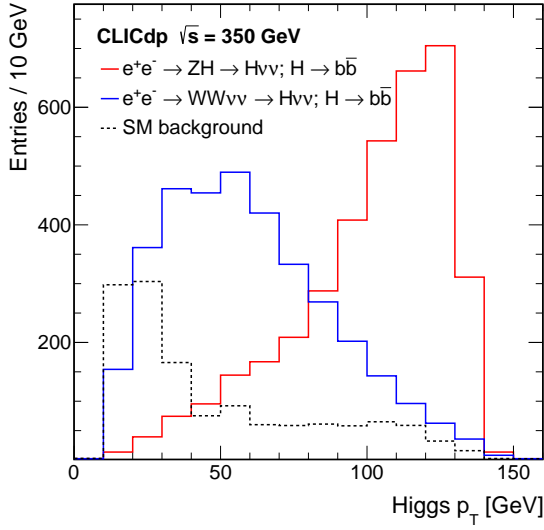


Fig. 10: Reconstructed Higgs candidate transverse momentum distributions for selected $H\nu\bar{\nu}$ events at $\sqrt{s} = 350\text{ GeV}$, showing the contributions from Higgsstrahlung, WW-fusion and non-Higgs background. The distributions are normalised to an integrated luminosity of 500 fb^{-1} .

Decay	Statistical uncertainty	
	Higgsstrahlung	WW-fusion
$H \rightarrow b\bar{b}$	0.84 %	1.9 %
$H \rightarrow c\bar{c}$	10.3 %	14.3 %
$H \rightarrow g\bar{g}$	4.5 %	5.7 %

Table 10: Summary of statistical uncertainties for events with a $H \rightarrow b\bar{b}$, $H \rightarrow c\bar{c}$ or $H \rightarrow g\bar{g}$ decay, where the Higgs boson is produced by Higgsstrahlung or WW-fusion, at $\sqrt{s} = 350\text{ GeV}$ derived from the template fit as described in the text. All numbers correspond to an integrated luminosity of 500 fb^{-1} .

or from Higgsstrahlung events where $Z \rightarrow \nu\bar{\nu}$. For this reason, the product of $\sigma(\text{ZH}) \times \text{BR}(H \rightarrow \tau^+\tau^-)$ is only determined for the case of hadronic Z decays at $\sqrt{s} = 350\text{ GeV}$. Here the experimental signature is two hadronic jets from $Z \rightarrow q\bar{q}$ and two isolated low-multiplicity narrow jets from the two tau decays [49]. Candidate τ leptons are identified using the TAU-FINDER algorithm [50], which is a seeded-cone based jet-clustering algorithm. The algorithm was optimised to distinguish the tau lepton decay products from hadronic gluon or quark jets. Tau cones are seeded from single tracks ($p_T > 5\text{ GeV}$). The seeds are used to define narrow cones of 0.05 radian half-angle. The cones are required to contain either one or three charged particles (from one- and three-prong tau decays) and further rejection of background from hadronic jets is implemented using cuts on isolation-related variables. Tau cones which contain identified elec-

Process	σ/fb	ϵ_{presel}	ϵ_{BDT}	N_{BDT}
$e^+e^- \rightarrow \text{ZH};$ $Z \rightarrow q\bar{q}, H \rightarrow \tau^+\tau^-$	5.8	18 %	59 %	312
$e^+e^- \rightarrow \text{ZH};$ $Z \rightarrow \tau^+\tau^-, H \rightarrow X$	4.6	15 %	2.6 %	9
$e^+e^- \rightarrow q\bar{q}\tau\tau(\text{non-Higgs})$	70	10 %	3.3 %	117
$e^+e^- \rightarrow q\bar{q}\tau\nu\nu$	1.6	9.7 %	5.1 %	4
$e^+e^- \rightarrow q\bar{q}q\bar{q}$	5900	0.13 %	0.54 %	21

Table 11: Cross sections and numbers of preselected and selected events with $\text{BDT} > 0.08$ (see Figure 11) for $e^+e^- \rightarrow \text{ZH}(Z \rightarrow q\bar{q}, H \rightarrow \tau^+\tau^-)$ signal events and the dominant backgrounds at $\sqrt{s} = 350\text{ GeV}$ assuming an integrated luminosity of 500 fb^{-1} .

trons or muons are rejected and only the hadronic one- and three-prong τ decays are retained. The τ identification efficiency for hadronic tau decays is found to be 73% and the fake rate to mistake a quark for a τ is 5%. The fake rate is relatively high, but is acceptable as the background from final states with quarks can be suppressed using global event properties.

Events with two identified hadronic tau candidates (with opposite net charge) are considered as $H \rightarrow \tau^+\tau^-$ decays. Further separation of the signal and background events is achieved using a BDT classifier based on the properties of the tau candidates and global event properties. The seventeen input discriminating variables are: the total p_T of the full event; the event thrust; the thrust and oblateness of the $\tau^+\tau^-$ system; the thrust and oblateness of the quark system; the sum of the transverse momenta of both τ candidates and of the quark jets; the cosines of the polar angle of both τ candidates; the invariant mass of the $\tau^+\tau^-$ system; the invariant mass of the quark system; the angle between the two τ candidates; the angle between the two quark jets; the polar angle of the missing momentum vector; the azimuthal angle between the two τ candidates; the azimuthal angle between the two quark jets; and the visible energy in the event. The resulting BDT distributions for the signal and the backgrounds are shown in Figure 11. Events passing a cut on the BDT output maximising the significance of the measurement are selected. The cross sections and numbers of selected events for the signal and the dominant background processes are listed in Table 11. The contribution from background processes with photons in the initial state is negligible after the event selection. A template fit to the BDT output distributions leads to:

$$\frac{\Delta[\sigma(\text{ZH}) \times \text{BR}(H \rightarrow \tau^+\tau^-)]}{\sigma(\text{ZH}) \times \text{BR}(H \rightarrow \tau^+\tau^-)} = 6.2\%.$$

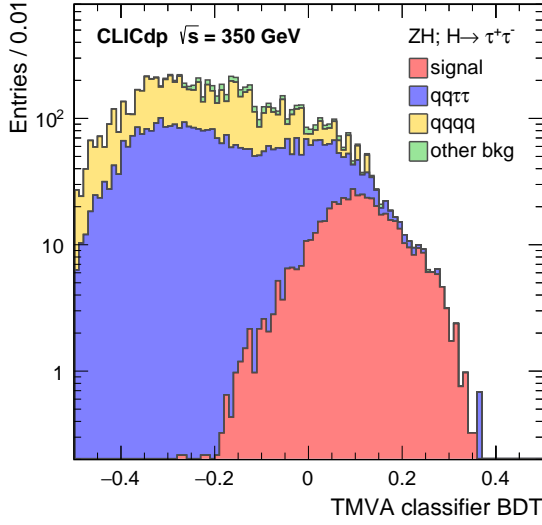


Fig. 11: BDT classifier distributions for $H \rightarrow \tau^+\tau^-$ events at $\sqrt{s} = 350$ GeV, showing the signal and main backgrounds as stacked histograms. The distributions are normalised to an integrated luminosity of 500 fb^{-1} .

5.2.3 $H \rightarrow WW^*$

In case the Higgs boson decays to a pair of W bosons, only the fully hadronic channel, $H \rightarrow WW^* \rightarrow q\bar{q}q\bar{q}$, allows the reconstruction of the Higgs invariant mass. Two final states in $e^+e^- \rightarrow ZH$ events have been studied depending on the Z boson decay mode: $Z \rightarrow l^+l^-$, where l is an electron or muon, and $Z \rightarrow q\bar{q}$.

First, isolated electrons and muons from Z decays are identified. To recover the effect of bremsstrahlung photons radiated off the leptons, all photons in a cone with an opening angle of 3° around the flight direction of a lepton candidate are added to its four-momentum. The impact of the bremsstrahlung recovery on the reconstruction of the $Z \rightarrow e^+e^-$ decays is illustrated in Figure 12. The bremsstrahlung effect leads to a tail at lower values in the Z candidate invariant mass distribution. This loss can be recovered by the procedure described above. It is also visible that a too large opening angle of the recovery cone leads to a tail at higher masses.

If a leptonic Z candidate is found, four jets are reconstructed from all particles not originating from the Z decay. The combination of two jet pairs where the invariant mass of one jet pair is closest to the W boson mass is selected. The events are considered further if the invariant mass of the Z boson candidate is in the range between 70 and 110 GeV and at least 20 particles are reconstructed.

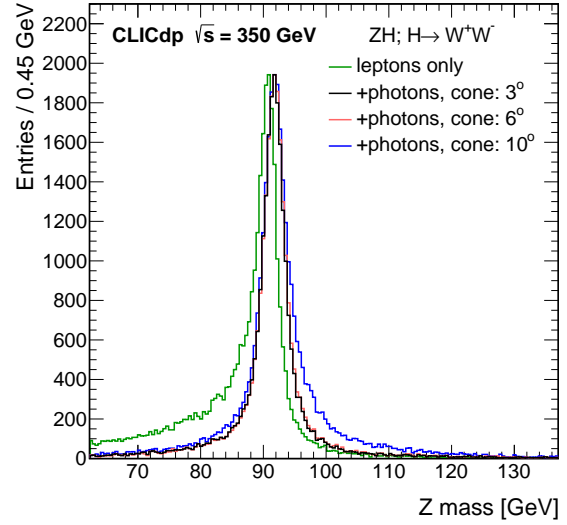


Fig. 12: Reconstructed invariant mass of $Z \rightarrow e^+e^-$ candidates in $e^+e^- \rightarrow ZH \rightarrow ZWW^*$ events at $\sqrt{s} = 350$ GeV. Bremsstrahlung photons in cones of different opening angles around the electron direction are recovered as described in the text. The normalisation is arbitrary.

Six jets are reconstructed in events without a leptonic Z candidate. These jets are grouped into W, Z and Higgs boson candidates minimising:

$$\chi^2 = \frac{(m_{ij} - m_W)^2}{\sigma_W^2} + \frac{(m_{kl} - m_Z)^2}{\sigma_Z^2} + \frac{(m_{ijmn} - m_H)^2}{\sigma_H^2},$$

where m_{ij} is the invariant mass of the jet pair used to reconstruct the W candidate, m_{kl} is the invariant mass of the jet pair used to reconstruct the Z candidate, m_{ijmn} is the invariant mass of the four jets used to reconstruct the Higgs candidate and $\sigma_{W,Z,H}$ are the estimated invariant mass resolutions for W, Z and Higgs boson candidates. The preselection cuts for this final state are:

- invariant mass of the Z candidate greater than 40 GeV;
- at least 50 reconstructed particles;
- event thrust of less than 0.95;
- no jet with a b-tag probability of more than 0.95;
- topology of the hadronic system consistent with six jets:
 - $-\log_{10}(y_{12}) < 2.0$, $-\log_{10}(y_{23}) < 2.6$, $-\log_{10}(y_{34}) < 3.0$,
 - $-\log_{10}(y_{45}) < 3.5$ and $-\log_{10}(y_{56}) < 4.0$.

For both final states, BDT classifiers are used to suppress the backgrounds further. The event selection for the signal processes and the most relevant background samples is summarised in Table 12. The expected precisions for the measurement of the investigated processes are summarised in Table 13. The best precision is achieved using the $Z \rightarrow q\bar{q}$ decay due to its large branching ratio compared to leptonic decays. The selection of $Z \rightarrow e^+e^-$ events is more difficult

Process	σ/fb	ϵ_{presel}	ϵ_{BDT}	N_{BDT}
$e^+e^- \rightarrow \text{ZH}; Z \rightarrow e^+e^-;$ $H \rightarrow \text{WW}^* \rightarrow q\bar{q}q\bar{q}$	0.45	80.2 %	45.5 %	95
$e^+e^- \rightarrow \text{ZH}; Z \rightarrow e^+e^-;$ $H \rightarrow \text{other}$	4.1	68.8 %	2.3 %	48
$e^+e^- \rightarrow q\bar{q}l\bar{l}$	1700	3.60 %	0.24 %	75
$e^+e^- \rightarrow \text{WWZ}$	10	3.1 %	5.9 %	9
$e^+e^- \rightarrow \text{ZH}; Z \rightarrow \mu^+\mu^-;$ $H \rightarrow \text{WW}^* \rightarrow q\bar{q}q\bar{q}$	0.45	86.8 %	64.8 %	125
$e^+e^- \rightarrow \text{ZH}; Z \rightarrow \mu^+\mu^-;$ $H \rightarrow \text{other}$	4.1	68.8 %	5.6 %	74
$e^+e^- \rightarrow q\bar{q}l\bar{l}$	1700	1.69 %	0.35 %	51
$e^+e^- \rightarrow \text{WWZ}$	10	2.6 %	7.1 %	9
$e^+e^- \rightarrow \text{ZH}; Z \rightarrow q\bar{q};$ $H \rightarrow \text{WW}^* \rightarrow q\bar{q}q\bar{q}$	9.2	70.9 %	40.9 %	1328
$e^+e^- \rightarrow \text{ZH}; Z \rightarrow q\bar{q};$ $H \rightarrow \text{other}$	84	16.6 %	10.4 %	730
$e^+e^- \rightarrow q\bar{q}q\bar{q}$	5850	18.1 %	0.098 %	2849
$e^+e^- \rightarrow t\bar{t}$	450	19.0 %	2.5 %	1071
$e^+e^- \rightarrow \text{WWZ}$	10	19.7 %	18.2 %	179

Table 12: Preselection and selection efficiencies for the ZH signal and most important background processes of the $H \rightarrow \text{WW}^*$ analysis in all three considered Z decay channels. The numbers assume an integrated luminosity of 500fb^{-1} at $\sqrt{s} = 350\text{GeV}$.

Process	Stat. uncertainty
$e^+e^- \rightarrow \text{ZH}; Z \rightarrow e^+e^-; H \rightarrow \text{WW}^* \rightarrow q\bar{q}q\bar{q}$	16.1 %
$e^+e^- \rightarrow \text{ZH}; Z \rightarrow \mu^+\mu^-; H \rightarrow \text{WW}^* \rightarrow q\bar{q}q\bar{q}$	13.1 %
$e^+e^- \rightarrow \text{ZH}; Z \rightarrow q\bar{q}; H \rightarrow \text{WW}^* \rightarrow q\bar{q}q\bar{q}$	5.9 %

Table 13: Statistical precisions for the listed processes at $\sqrt{s} = 350\text{GeV}$ for an integrated luminosity of 500fb^{-1} .

compared to $Z \rightarrow \mu^+\mu^-$ events because the $e^+e^- \rightarrow q\bar{q}l\bar{l}$ background sample contains more events with electron pairs than events with muon pairs. Hence the precision achieved using $Z \rightarrow \mu^+\mu^-$ decays is somewhat better compared to that obtained using $Z \rightarrow e^+e^-$ decays. The combined precision for an integrated luminosity of 500fb^{-1} is:

$$\frac{\Delta[\sigma(\text{ZH}) \times BR(H \rightarrow \text{WW}^*)]}{\sigma(\text{ZH}) \times BR(H \rightarrow \text{WW}^*)} = 5.1\%,$$

which is dominated by the final state with hadronic Z boson decays.

6 WW-fusion at $\sqrt{s} > 1\text{TeV}$

This section presents measurements of Higgs decays from the WW-fusion process at CLIC with centre-of-mass energies of 1.4 TeV and 3 TeV. The Higgs self-coupling mea-

surement, which is also accessed in WW-fusion production, is discussed in Section 9. The cross section of the Higgs production via the vector boson fusion process $e^+e^- \rightarrow \text{Hv}_e\bar{\text{v}}_e$ scales with $\log(s)$ and becomes the dominating Higgs production process in e^+e^- collisions with $\sqrt{s} > 500\text{GeV}$. The respective cross sections for $e^+e^- \rightarrow \text{Hv}_e\bar{\text{v}}_e$ at $\sqrt{s} = 1.4\text{TeV}$ and 3 TeV are approximately 244 fb and 415 fb, respectively, including the effects of the CLIC beamstrahlung spectrum and ISR. The relatively large cross sections at the higher energies allow the Higgs decay modes to be probed with high statistical precision and provide access to rarer Higgs decays, such as $H \rightarrow \mu^+\mu^-$.

Since WW-fusion $e^+e^- \rightarrow \text{Hv}_e\bar{\text{v}}_e$ proceeds through the t -channel, the Higgs boson is typically boosted along the beam direction and the presence of neutrinos in the final state can result in significant missing p_T . Because of the missing transverse and longitudinal momentum, the experimental signatures for $\text{Hv}_e\bar{\text{v}}_e$ production are relatively well separated from most SM backgrounds. At $\sqrt{s} = 350\text{GeV}$, the main SM background processes are two- and four-fermion production, $e^+e^- \rightarrow 2f$ and $e^+e^- \rightarrow 4f$. At higher energies, backgrounds from $\gamma\gamma$ and γe^\pm hard interactions become increasingly relevant for measurements of Higgs boson production in WW-fusion. Additionally, pile-up of relatively soft $\gamma\gamma \rightarrow \text{hadrons}$ events with the primary interaction occurs. However, this background of relatively low- p_T particles is largely mitigated through the timing cuts and jet finding strategy outlined in Section 4.

6.1 $H \rightarrow b\bar{b}, c\bar{c}, gg$

The physics potential for the measurement of hadronic Higgs decays at the centre-of-mass energies of 1.4 TeV and 3 TeV was studied using the CLIC_SiD detector model. The signatures for $H \rightarrow b\bar{b}$, $H \rightarrow c\bar{c}$ and $H \rightarrow gg$ decays in $e^+e^- \rightarrow \text{Hv}_e\bar{\text{v}}_e$ events are two jets and missing energy. Flavour tagging information from LCFIPLUS is used to separate the investigated Higgs boson decay modes in the selected event sample. The invariant mass of the reconstructed di-jet system provides rejection against background processes, e.g. hadronic Z boson decays.

At both centre-of-mass energies, an invariant mass of the di-jet system in the range from 60 to 160 GeV and a distance between both jets in the $\eta - \phi$ plane of less than 4 are required. The energy sum of the two jets must exceed 75 GeV and a missing momentum of at least 20 GeV is required. The efficiencies of these preselection cuts on the signal and dominant background samples are listed in Table 14 and Table 15 for the centre-of-mass energies of 1.4 and 3 TeV, respectively.

Process	σ/fb	$\epsilon_{\text{presele}}$	ϵ_{BDT}	N_{BDT}
$e^+e^- \rightarrow H\nu_e\bar{\nu}_e; H \rightarrow b\bar{b}$	136.9	84.5 %	37.7 %	65400
$e^+e^- \rightarrow H\nu_e\bar{\nu}_e; H \rightarrow c\bar{c}$	6.91	86.8 %	42.1 %	3740
$e^+e^- \rightarrow H\nu_e\bar{\nu}_e; H \rightarrow gg$	20.7	82.2 %	39.6 %	10100
$e^+e^- \rightarrow q\bar{q}\nu\bar{\nu}$	788	75.6 %	2.1 %	18500
$e^+e^- \rightarrow q\bar{q}l\nu$	4313	40.0 %	0.91 %	23600
$e^\pm\gamma \rightarrow q\bar{q}e$	16600	13.7 %	0.54 %	18500
$e^\pm\gamma \rightarrow q\bar{q}\nu$	29300	60.2 %	0.64 %	170000
$\gamma\gamma \rightarrow q\bar{q}$	76600	4.2 %	0.47 %	22200

Table 14: Preselection and selection efficiencies for the signal and most important background processes in the $H \rightarrow b\bar{b}$, $H \rightarrow c\bar{c}$ and $H \rightarrow gg$ analysis. The numbers of events correspond to 1.5 ab^{-1} at $\sqrt{s} = 1.4 \text{ TeV}$.

Process	σ/fb	$\epsilon_{\text{presele}}$	ϵ_{BDT}	N_{BDT}
$e^+e^- \rightarrow H\nu_e\bar{\nu}_e; H \rightarrow b\bar{b}$	232.8	74.4 %	34.7 %	120000
$e^+e^- \rightarrow H\nu_e\bar{\nu}_e; H \rightarrow c\bar{c}$	11.7	75.3 %	36.2 %	6340
$e^+e^- \rightarrow H\nu_e\bar{\nu}_e; H \rightarrow gg$	35.2	68.8 %	34.6 %	16800
$e^+e^- \rightarrow q\bar{q}\nu\bar{\nu}$	1305	67.2 %	2.7 %	47400
$e^+e^- \rightarrow q\bar{q}e\nu$	5255	45.0 %	1.1 %	52200
$e^\pm\gamma \rightarrow q\bar{q}e$	20500	12.7 %	2.3 %	118000
$e^\pm\gamma \rightarrow q\bar{q}\nu$	46400	45.9 %	0.92 %	394000
$\gamma\gamma \rightarrow q\bar{q}$	92200	7.0 %	1.6 %	207000

Table 15: Preselection and selection efficiencies for the signal and most important background processes in the $H \rightarrow b\bar{b}$, $H \rightarrow c\bar{c}$ and $H \rightarrow gg$ analysis. The numbers of events correspond to 2 ab^{-1} at $\sqrt{s} = 3 \text{ TeV}$.

The backgrounds are suppressed further using a single BDT at each energy. The samples of signal events used to train these classifiers consist of equal amounts of $H \rightarrow b\bar{b}$, $H \rightarrow c\bar{c}$ and $H \rightarrow gg$ events while the different processes in the background sample were normalised according to their respective cross sections. No flavour tagging information is used in the event selection. This leads to classifiers with similar selection efficiencies for events with the different signal Higgs decays.

The fractions of signal events with $H \rightarrow b\bar{b}$, $H \rightarrow c\bar{c}$ and $H \rightarrow gg$ decays in the selected event samples are extracted from the two-dimensional distributions of the $b\bar{b}$ versus $c\bar{c}$ likelihood variables for the two reconstructed jets as defined in Section 5.2. The normalisations of the backgrounds from other Higgs decays and non-Higgs events are fixed and expected to be provided by other measurements. The results of these fits are shown in Table 16 and Table 17 at 1.4 and 3 TeV, respectively.

The expected precisions obtained at 1.4 and 3 TeV are similar although the number of signal events is about twice as large at 3 TeV compared to 1.4 TeV. The main reasons for

Process	Statistical uncertainty
$e^+e^- \rightarrow H\nu_e\bar{\nu}_e; H \rightarrow b\bar{b}$	0.4 %
$e^+e^- \rightarrow H\nu_e\bar{\nu}_e; H \rightarrow c\bar{c}$	6.1 %
$e^+e^- \rightarrow H\nu_e\bar{\nu}_e; H \rightarrow gg$	5.0 %

Table 16: Statistical precisions for the listed processes from the fit described in the text at $\sqrt{s} = 1.4 \text{ TeV}$ for an integrated luminosity of 1.5 ab^{-1} .

Process	Statistical uncertainty
$e^+e^- \rightarrow H\nu_e\bar{\nu}_e; H \rightarrow b\bar{b}$	0.3 %
$e^+e^- \rightarrow H\nu_e\bar{\nu}_e; H \rightarrow c\bar{c}$	6.9 %
$e^+e^- \rightarrow H\nu_e\bar{\nu}_e; H \rightarrow gg$	4.3 %

Table 17: Statistical precisions for the listed processes from the fit described in the text at $\sqrt{s} = 3 \text{ TeV}$ for an integrated luminosity of 2 ab^{-1} .

this are that the jet reconstruction and flavour tagging are more challenging at 3 TeV since the jets from the Higgs decay tend more towards the beam axis and the impact of the beam-induced backgrounds is larger compared to 1.4 TeV. In addition, the cross sections for the most important background processes rise with \sqrt{s} (see Table 16 and Table 17).

6.2 $H \rightarrow \tau^+\tau^-$

The sensitivity for the measurement of $\sigma(e^+e^- \rightarrow H\nu_e\bar{\nu}_e) \times BR(H \rightarrow \tau^+\tau^-)$ at CLIC has been studied using the CLIC_ILD detector model at centre-of-mass energies of 1.4 TeV and 3 TeV [51]. For a SM Higgs with a mass of 126 GeV, $BR(H \rightarrow \tau^+\tau^-) = 6.15 \%$, resulting in an effective signal cross section of 15.0 fb at $\sqrt{s} = 1.4 \text{ TeV}$ and 25.5 fb at $\sqrt{s} = 3 \text{ TeV}$.

The experimental signature is two relatively high-momentum narrow jets from the two tau decays and significant missing transverse and longitudinal momenta. A typical event display is shown in Figure 13. The analysis is restricted to hadronic τ decays, which are identified using the TAU-FINDER algorithm, as described in Section 5.2.2. The TAU-FINDER algorithm parameters were tuned using the $H \rightarrow \tau^+\tau^-$ signal events and $e^+e^- \rightarrow q\bar{q}\nu\bar{\nu}$ background events. The working point has a τ selection efficiency of 70 % (60 %) with a quark jet fake rate of 7 % (9 %) at $\sqrt{s} = 1.4 \text{ TeV}$ ($\sqrt{s} = 3 \text{ TeV}$). All relevant SM backgrounds are taken into account, including $\gamma\gamma$ and γe^\pm collisions. The most significant backgrounds are $e^+e^- \rightarrow \tau^+\tau^-\nu\bar{\nu}$, $e^\pm\gamma \rightarrow \tau^+\tau^-e^\pm$ and $\gamma\gamma \rightarrow \tau^+\tau^-\nu\bar{\nu}$. The latter two processes become increasingly important at higher \sqrt{s} , due to the increasing number of beamstrahlung photons.

Process	σ/fb	ϵ_{presel}	ϵ_{BDT}	N_{BDT}
$e^+e^- \rightarrow H\nu_e\bar{\nu}_e; H \rightarrow \tau^+\tau^-$	15.0	9.3 %	38.9 %	814
$e^+e^- \rightarrow \tau^+\tau^-\nu\bar{\nu}$	38.5	5.0 %	18.0 %	528
$e^\pm\gamma \rightarrow \tau^+\tau^-e^\pm$	2580	1.9 %	0.075 %	45
$\gamma\gamma \rightarrow \tau^+\tau^-(\nu\bar{\nu} \text{ or } l^-l^+)$	128.1	2.7 %	2.25 %	79

Table 18: Preselection and selection efficiencies for the signal and most important background processes in the $H \rightarrow \tau^+\tau^-$ analysis. The numbers of events correspond to 1.5 ab^{-1} at $\sqrt{s} = 1.4 \text{ TeV}$. The cross sections for the backgrounds include cuts on the kinematic properties of the tau lepton pair applied on generator level. The preselection efficiencies include the reconstruction of two hadronic tau lepton decays per event.

Process	σ/fb	ϵ_{presel}	ϵ_{BDT}	N_{BDT}
$e^+e^- \rightarrow H\nu_e\bar{\nu}_e; H \rightarrow \tau^+\tau^-$	25.5	9.2 %	23.2 %	787
$e^+e^- \rightarrow \tau^+\tau^-\nu\bar{\nu}$	39.2	8.3 %	11.1 %	498
$e^\pm\gamma \rightarrow \tau^+\tau^-e^\pm$	2770	2.8 %	0.26 %	246
$\gamma\gamma \rightarrow \tau^+\tau^-(\nu\bar{\nu} \text{ or } l^-l^+)$	218	2.8 %	0.14 %	9

Table 19: Preselection and selection efficiencies for the signal and most important background processes in the $H \rightarrow \tau^+\tau^-$ analysis. The numbers of events correspond to 2 ab^{-1} at $\sqrt{s} = 3 \text{ TeV}$. The cross sections for the backgrounds include cuts on the kinematic properties of the tau lepton pair applied on generator level. The preselection efficiencies include the reconstruction of two hadronic tau lepton decays per event.

Backgrounds from Higgs decays other than $H \rightarrow \tau^+\tau^-$ are expected to be negligible [52].

The event preselection requires two identified τ leptons, both of which must be within the polar angle range $15^\circ < \theta(\tau) < 165^\circ$ and have $p_T(\tau) > 25 \text{ GeV}$. To reject back-to-back or nearby tau leptons, the angle between the two tau candidates must satisfy $29^\circ < \Delta\theta(\tau\tau) < 177^\circ$. The visible invariant mass $m(\tau\tau)$ and the visible transverse mass $m_T(\tau\tau)$ of the two tau candidates must satisfy $45 \text{ GeV} < m(\tau\tau) < 130 \text{ GeV}$ and $m_T(\tau\tau) < 20 \text{ GeV}$. Finally the event thrust must be less than 0.99.

Events passing the preselection are classified as either signal or SM background using a BDT classifier. The kinematic variables used in the classifier are $m(\tau\tau)$, $m_T(\tau\tau)$, event shape variables (such as thrust and oblateness), the missing p_T , the polar angle of the missing momentum vector $|\cos\theta_{\text{miss}}|$ and the total reconstructed energy excluding the Higgs candidate. The event selection for the signal and the most relevant background processes is summarised in Table 18 for $\sqrt{s} = 1.4 \text{ TeV}$ and in Table 19 for $\sqrt{s} = 3 \text{ TeV}$. Rather than

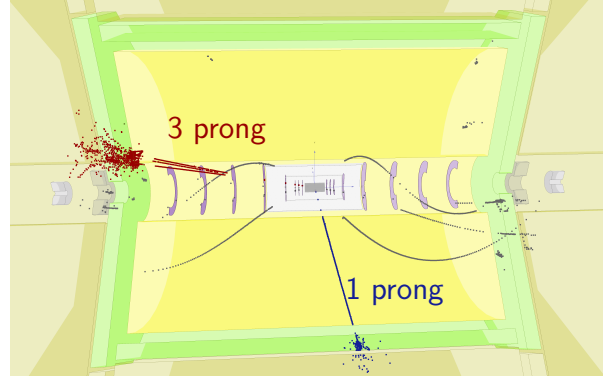


Fig. 13: Event display of a $H \rightarrow \tau^+\tau^-$ event at $\sqrt{s} = 1.4 \text{ TeV}$ in the CLIC_ILD detector. A 1-prong tau decay is visible in the central part of the detector (blue). The other tau lepton decays to three charged particles and is reconstructed in the forward direction (red). A few soft particles from beam-induced backgrounds are also visible (grey).

applying a simple cut, the full BDT shape information is utilised in a template fit. The resulting statistical uncertainties for 1.5 ab^{-1} at $\sqrt{s} = 1.4 \text{ TeV}$ and 2.0 ab^{-1} at $\sqrt{s} = 3 \text{ TeV}$ are:

$$\frac{\Delta[\sigma(H\nu_e\bar{\nu}_e) \times BR(H \rightarrow \tau^+\tau^-)]}{\sigma(H\nu_e\bar{\nu}_e) \times BR(H \rightarrow \tau^+\tau^-)} = 4.2 \% \text{ at } 1.4 \text{ TeV},$$

$$\frac{\Delta[\sigma(H\nu_e\bar{\nu}_e) \times BR(H \rightarrow \tau^+\tau^-)]}{\sigma(H\nu_e\bar{\nu}_e) \times BR(H \rightarrow \tau^+\tau^-)} = 4.4 \% \text{ at } 3 \text{ TeV}.$$

Similar to the observations described in Section 6.1, the expected precisions at 1.4 TeV and 3 TeV are similar. The identification of tau leptons is more challenging at 3 TeV where the impact of the beam-induced backgrounds is larger and the tau leptons from Higgs decays in signal events tend more towards the beam axis.

6.3 $H \rightarrow WW^*$

The signature for $H \rightarrow WW^*$ decays in $e^+e^- \rightarrow H\nu_e\bar{\nu}_e$ is less clearly defined than e.g. for $H \rightarrow q\bar{q}$. There is missing p_T from the $\nu_e\bar{\nu}_e$ system, but the final-state topology will depend on the WW^* decay modes. Since $m_H < 2m_W$, at least one of the W-bosons has to be off mass-shell. Studies for two different final states are described in the following. The presence of a charged lepton in the $WW^* \rightarrow q\bar{q}l\nu$ final state suppresses backgrounds from other Higgs decays. However, the invariant mass of the Higgs boson in $H \rightarrow WW^*$ decays can be reconstructed for fully-hadronic decays alone, $WW^* \rightarrow q\bar{q}q\bar{q}$.

6.3.1 $WW^* \rightarrow q\bar{q}q\bar{q}$

The experimental signature for $H\nu_e\bar{\nu}_e$ production with $H \rightarrow WW^* \rightarrow q\bar{q}q\bar{q}$ is a four-jet final state with missing p_T and a total invariant mass consistent with the Higgs mass, where one pair of jets has a mass consistent with m_W . There are two main sources of potential backgrounds. The first being other Higgs decays, in particular $H \rightarrow b\bar{b}$, $H \rightarrow c\bar{c}$ and $H \rightarrow gg$, which produce hadronic final states with an invariant mass consistent with the Higgs mass; here QCD radiation in the parton shower can lead to a four-jet topology. The second main source of potential background comes from non-Higgs processes such as $e^+e^- \rightarrow q\bar{q}\nu\bar{\nu}$ and $\gamma e^\pm \rightarrow q\bar{q}q\bar{q}\nu$.

The $H \rightarrow WW^*$ event selection has been studied at $\sqrt{s} = 1.4\text{TeV}$ using the CLIC_ILD detector model. It proceeds in two separate stages: a set of preselection cuts designed to reduce the backgrounds from large cross section processes such as $e^+e^- \rightarrow q\bar{q}$ and $e^+e^- \rightarrow q\bar{q}q\bar{q}$; followed by a likelihood-based multivariate event selection. The preselection variables are formed by forcing each event into four jets using the Durham jet finder. Of the three possible jet associations with candidate W bosons, (12)(34), (13)(24) or (14)(23), the one giving a di-jet invariant mass closest to m_W is selected. The preselection cuts require: $\log_{10}(y_{23}) > -2.75$ and $\log_{10}(y_{34}) > -3.5$; visible energy, $125\text{GeV} < E_{\text{vis}} < 600\text{GeV}$; missing transverse momentum, $p_T > 65\text{GeV}$; $\cos\theta_{\text{miss}} < 0.99$; one candidate on-shell W boson, $50\text{GeV} < m_{W1} < 95\text{GeV}$; one off-shell W boson, $m_{W2} < 65\text{GeV}$; total invariant mass consistent with a Higgs decay, $90\text{GeV} < m_H < 150\text{GeV}$; and the absence of a high-energy electron or muon, $E_{\text{lept}} < 30\text{GeV}$. In addition, in order to reject $H \rightarrow b\bar{b}$ decays, the event is forced into a two-jet topology and flavour tagging is applied to the two jets. Events where at least one jet has a b-tag probability of greater than 0.95 are rejected as part of the preselection. The cross sections and preselection efficiencies for the signal and main background processes are listed in Table 20. After the preselection, the main backgrounds are $e^+e^- \rightarrow q\bar{q}\nu\bar{\nu}$, $\gamma e^\pm \rightarrow q\bar{q}q\bar{q}\nu$ and other Higgs decay modes, predominantly $H \rightarrow b\bar{b}$ and $H \rightarrow gg$.

A relative likelihood selection is used to classify all events passing the preselection cuts. Five event categories including the signal are considered. The relative likelihood of an event being signal is defined as:

$$\mathcal{L} = \frac{L(H \rightarrow WW^* \rightarrow q\bar{q}q\bar{q})}{L(H \rightarrow WW^* \rightarrow q\bar{q}q\bar{q}) + L_1 + L_2 + L_3 + L_4},$$

where L_i represents the likelihood for four background categories: $H \rightarrow b\bar{b}$, $H \rightarrow gg$, $e^+e^- \rightarrow q\bar{q}\nu\bar{\nu}$ and $\gamma e^\pm \rightarrow q\bar{q}q\bar{q}\nu$. The absolute likelihood L for each event type is formed from normalised probability distributions $P_i(x_i)$ of the N likelihood discriminating variables x_i for that event type. For ex-

Process	σ/fb	ϵ_{prese1}	$\epsilon_{\mathcal{L}>0.35}$	$N_{\mathcal{L}>0.35}$
$H\nu_e\bar{\nu}_e$	244.1	14.61 %	3.0 %	11101
$H \rightarrow WW^* \rightarrow q\bar{q}q\bar{q}$		32.4 %	18.1 %	7518
$H \rightarrow WW^* \rightarrow q\bar{q}l\nu$		4.4 %	0.6 %	253
$H \rightarrow b\bar{b}$		1.9 %	0.4 %	774
$H \rightarrow c\bar{c}$		8.1 %	2.1 %	209
$H \rightarrow gg$		19.1 %	7.1 %	1736
$H \rightarrow ZZ^*$		12.0 %	5.0 %	556
$H \rightarrow \text{other}$		0.7 %	0.2 %	55
$e^+e^- \rightarrow q\bar{q}\nu\bar{\nu}$	788.0	4.6 %	0.2 %	2225
$e^+e^- \rightarrow q\bar{q}q\bar{q}l\nu$	115.3	0.1 %	<0.1 %	43
$e^+e^- \rightarrow q\bar{q}q\bar{q}\nu\bar{\nu}$	24.7	0.8 %	0.4 %	130
$\gamma e^+(\gamma e^-) \rightarrow q\bar{q}q\bar{q}\nu$	254.3	1.8 %	0.4 %	1389

Table 20: Summary of the $H \rightarrow WW^* \rightarrow q\bar{q}q\bar{q}$ event selection at $\sqrt{s} = 1.4\text{TeV}$, giving the raw cross sections, preselection efficiency, overall selection efficiency for a likelihood cut of $\mathcal{L} > 0.35$ and the expected numbers of events passing the event selection for an integrated luminosity of 1.5ab^{-1} .

ample, the distribution of the reconstructed Higgs mass for all events passing the preselection is shown in Figure 14, where it can be seen that good separation between signal and background is achievable. The discriminating variables are: the 2D distribution of reconstructed invariant masses m_H and m_W ; the 2D distribution of minimal k_t distances y_{23} , y_{34} ; and 2D distribution of b-tag probabilities when the event is forced into two jets. The use of 2D distributions accounts for the most significant correlations between the likelihood variables. The selection efficiencies and expected numbers of events for the signal dominated region, $\mathcal{L} > 0.35$, are listed in Table 20.

The expected precision on $BR(H \rightarrow WW^*)$ is extracted from a fit to the likelihood distribution. Given the non-negligible backgrounds from other Higgs decays, it is necessary to simultaneously fit the different components. A χ^2 fit to the expected \mathcal{L} distribution is performed by scaling independently five components: the $H \rightarrow WW^*$ signal; the $H \rightarrow b\bar{b}$, $H \rightarrow c\bar{c}$ and $H \rightarrow gg$ backgrounds; and all other backgrounds (dominated by $q\bar{q}\nu\bar{\nu}$ and $q\bar{q}q\bar{q}\nu$). The constraints on the $H \rightarrow b\bar{b}$, $H \rightarrow c\bar{c}$ and $H \rightarrow gg$ branching ratios, as described in Section 6.1, are implemented by modifying the χ^2 function to include penalty terms:

$$\chi^2 \rightarrow \chi^2 + \frac{(s_{b\bar{b}} - 1)^2}{\sigma_{b\bar{b}}^2} + \frac{(s_{c\bar{c}} - 1)^2}{\sigma_{c\bar{c}}^2} + \frac{(s_{gg} - 1)^2}{\sigma_{gg}^2} + \frac{(s_{ZZ^*} - 1)^2}{\sigma_{ZZ^*}^2} + \frac{(b - 1)^2}{\sigma_b^2}.$$

Here, for example, s_{gg} is the amount by which the $H \rightarrow gg$ complement is scaled in the fit and σ_{gg} is the expected statistical error on $BR(H \rightarrow gg)$ from the analysis of Section 6.1.

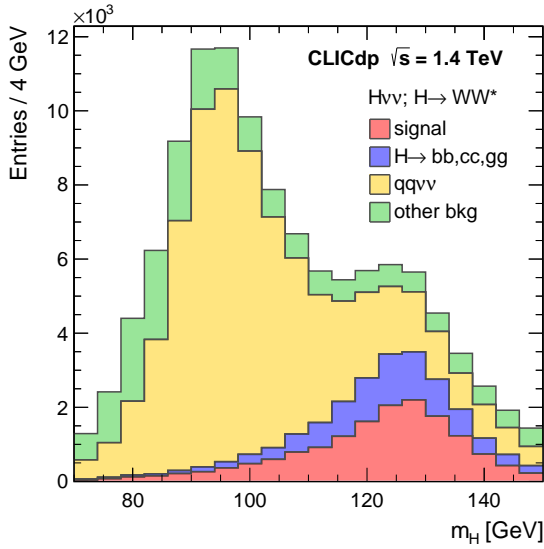


Fig. 14: Reconstructed Higgs invariant mass distributions for preselected $H \rightarrow WW^* \rightarrow q\bar{q}q\bar{q}$ events at $\sqrt{s} = 1.4$ TeV, showing the signal and main backgrounds as stacked histograms. The distributions are normalised to an integrated luminosity of 1.5 ab^{-1} .

The expected uncertainties on the contributions from $H \rightarrow b\bar{b}$ and $H \rightarrow c\bar{c}$ are taken from the same analysis. The uncertainty on the background from $H \rightarrow ZZ^*$ is assumed here to be known to 1 % from other measurements of g_{HZZ}^2 and g_{HZZ}^2/g_{HWW}^2 . The systematic uncertainty in the non-H background, denoted by b , is taken to be 1 %. The resulting statistical uncertainty on the $H \rightarrow WW^*$ branching ratio is:

$$\frac{\Delta[\sigma(H\nu_e\bar{\nu}_e) \times BR(H \rightarrow WW^*)]}{\sigma(H\nu_e\bar{\nu}_e) \times BR(H \rightarrow WW^*)} = 1.5 \%. \quad (6.3.2)$$

6.3.2 $WW^* \rightarrow q\bar{q}l\nu$

In a different approach, the $H \rightarrow WW^* \rightarrow q\bar{q}l\nu$ decay is reconstructed [53]. The study is performed at $\sqrt{s} = 1.4$ TeV using the CLIC_ILD detector model.

In the first stage of the analysis, isolated leptons from the leptonic W decay are searched for. An efficiency of 93 % is achieved for the identification of electrons and muons in signal events including the geometrical acceptance of the detector. Two jets are reconstructed from the rest of the particles not including the isolated lepton. Flavour tagging information is obtained from the LCFIPLUS package.

The following preselection cuts are imposed:

- energy of the W candidate less than 591 GeV;
- mass of the W candidate less than 231 GeV;
- energy of the H candidate less than 306 GeV;

Process	σ/fb	ϵ_{presel}	ϵ_{BDT}	N_{BDT}
$e^+e^- \rightarrow H\nu_e\bar{\nu}_e;$ $H \rightarrow WW^* \rightarrow q\bar{q}l\nu$	18.9	100.0 %	42.7 %	12100
$e^+e^- \rightarrow H\nu_e\bar{\nu}_e;$ $H \rightarrow WW^* \rightarrow q\bar{q}q\bar{q}$	25.6	100.0 %	1.79 %	687
$e^+e^- \rightarrow H\nu_e\bar{\nu}_e;$ $H \rightarrow \text{other}$	199.6	99.6 %	1.26 %	3767
$e^+e^- \rightarrow q\bar{q}\nu\bar{\nu}$	788	96.6 %	0.07 %	777
$e^+e^- \rightarrow q\bar{q}ll$	2726	89.8 %	<0.01 %	257
$e^+e^- \rightarrow q\bar{q}l\nu$	4310	66.4 %	0.07 %	4810
$\gamma e^+(\gamma e^-) \rightarrow q\bar{q}e^+(q\bar{q}e^-)$	88400	85.3 %	<0.01 %	1580

Table 21: Preselection and selection efficiencies for the signal and most important background processes in the $H \rightarrow WW^* \rightarrow q\bar{q}l\nu$ analysis. Numbers of events correspond to 1.5 ab^{-1} at $\sqrt{s} = 1.4$ TeV.

- total missing energy of the event in the range between 667 GeV and 1.4 TeV.

Nearly all signal events pass this preselection while more than 30 % of the most critical $e^+e^- \rightarrow q\bar{q}l\nu$ background events are rejected. The background processes are suppressed further using a BDT classifier with 19 input variables including the number of isolated leptons. The event selection is summarised in Table 21. The resulting statistical precision for 1.5 ab^{-1} is:

$$\frac{\Delta[\sigma(H\nu_e\bar{\nu}_e) \times BR(H \rightarrow WW^*)]}{\sigma(H\nu_e\bar{\nu}_e) \times BR(H \rightarrow WW^*)} = 1.3 \%. \quad (6.4)$$

When combining the results for the $H \rightarrow WW^* \rightarrow q\bar{q}q\bar{q}$ and $H \rightarrow WW^* \rightarrow q\bar{q}l\nu$ decays, the precision improves to 1.0 % at $\sqrt{s} = 1.4$ TeV for an integrated luminosity of 1.5 ab^{-1} .

6.4 $H \rightarrow ZZ^*$

The decay $H \rightarrow ZZ^*$ in $e^+e^- \rightarrow H\nu_e\bar{\nu}_e$ events can be studied using $Z^{(*)} \rightarrow q\bar{q}$ and $Z^{(*)} \rightarrow l^+l^-$ decays. The $ZZ^* \rightarrow q\bar{q}l^+l^-$ final state has been studied at $\sqrt{s} = 1.4$ TeV using the CLIC_ILD detector model. The experimental signature is given by two jets, a pair of oppositely charged leptons and missing p_T . The total invariant mass of all visible final-state particles is equal to the Higgs mass while either, the quarks or the charged lepton pair, have a mass consistent with m_Z . Due to the large background from $H \rightarrow WW^*$, the $ZZ^* \rightarrow q\bar{q}q\bar{q}$ final state is not considered here. In addition, the $ZZ^* \rightarrow l^+l^-l^+l^-$ signature is not expected to be competitive at CLIC due to the small number of expected events.

The analysis is performed in several steps. First, isolated electrons and muons with an impact parameter of less than 0.02 mm are searched for. Hadronic τ lepton decays are

Process	σ/fb	ϵ_{presel}	ϵ_{BDT}	N_{BDT}
$e^+e^- \rightarrow H\nu_e\bar{\nu}_e;$ $H \rightarrow ZZ^* \rightarrow q\bar{q}l^+l^-$	0.995	62 %	46 %	425
$e^+e^- \rightarrow H\nu_e\bar{\nu}_e;$ $H \rightarrow WW^* \rightarrow q\bar{q}q\bar{q}$	25.6	32 %	0.002 %	24
$e^+e^- \rightarrow H\nu_e\bar{\nu}_e; H \rightarrow b\bar{b}$	137	20.3 %	0.0006 %	23
$e^+e^- \rightarrow H\nu_e\bar{\nu}_e; H \rightarrow gg$	21	25 %	0.0005 %	4
$e^+e^- \rightarrow H\nu_e\bar{\nu}_e; H \rightarrow c\bar{c}$	6.9	23 %	0.0 %	0
$e^+e^- \rightarrow H\nu_e\bar{\nu}_e; H \rightarrow \text{other}$	51	50 %	0.003 %	98

Table 22: Preselection and selection efficiencies for the signal and the relevant background processes in the $H \rightarrow ZZ^*$ analysis. The numbers of events correspond to 1.5 ab^{-1} at $\sqrt{s} = 1.4 \text{ TeV}$. All background processes other than Higgs production were completely rejected by the event selection.

identified using the TAU-FINDER algorithm described in [Section 5.2.2](#), with the requirement $p_T > 10 \text{ GeV}$ for the seed track and $p_T > 4 \text{ GeV}$ for all other tracks within a search cone of 0.15 radian half-angle. In signal events, 87 % of the electron or muon pairs and 37 % of the tau leptons are found including the effect of the limited geometrical acceptance of the detector in the forward direction.

In events with exactly two identified leptons of the same flavour, two jets are reconstructed from the remaining particles. No other preselection cuts are applied. Flavour tagging information is obtained from the LCFIPLUS package.

A BDT classifier is used to suppress the background processes using 17 input variables, including:

- the invariant masses of the H, Z and Z^* candidates;
- the topology of the hadronic system: $-\log_{10}(y_{34})$, $-\log_{10}(y_{23})$ and $-\log_{10}(y_{12})$;
- the b-tag and c-tag probabilities for both jets;
- the visible energy and the missing transverse momentum of the event;
- the number of particles in the event.

The event selection is summarised in [Table 22](#). Only backgrounds from other Higgs decays pass the event selection while all other background processes are completely suppressed. The invariant mass distribution of the Higgs candidates in events with two isolated leptons and after the full selection chain including the BDT classifier is shown in [Figure 15](#). The resulting statistical uncertainty is:

$$\frac{\Delta[\sigma(H\nu_e\bar{\nu}_e) \times BR(H \rightarrow ZZ^*)]}{\sigma(H\nu_e\bar{\nu}_e) \times BR(H \rightarrow ZZ^*)} = 5.6 \%.$$

Process	σ/fb	ϵ_{presel}	ϵ_{BDT}	N_{BDT}
$e^+e^- \rightarrow H\nu_e\bar{\nu}_e; H \rightarrow \gamma\gamma$	0.56	84.9 %	40.4 %	337
$e^+e^- \rightarrow \nu\bar{\nu}\gamma$	29.5	34.2 %	2.5 %	1110
$e^+e^- \rightarrow \nu\bar{\nu}\gamma\gamma$	17.3	31.0 %	2.6 %	688
$e^+e^- \rightarrow \gamma\gamma$	27.2	19.8 %	0.14 %	55
$e^+e^- \rightarrow e^+e^-\gamma$	289.0	9.2 %	0.06 %	265
$e^+e^- \rightarrow e^+e^-\gamma\gamma$	12.6	5.2 %	0.01 %	2
$e^+e^- \rightarrow q\bar{q}\gamma$	67.0	0.8 %	0.0 %	0
$e^+e^- \rightarrow q\bar{q}\gamma\gamma$	16.6	1.4 %	0.01 %	2

Table 23: Signal and relevant background processes used in the $H \rightarrow \gamma\gamma$ analysis. Additional photons from ISR and FSR are present in each sample. The numbers of events correspond to 1.5 ab^{-1} at $\sqrt{s} = 1.4 \text{ TeV}$.

6.5 $H \rightarrow \gamma\gamma$

The measurement of the $H \rightarrow \gamma\gamma$ decay played a central role in the discovery of the Higgs boson at the LHC [1, 2]. In the SM, this decay is induced via loops of heavy charged particles, with dominant contributions due to W bosons and t quarks. For BSM scenarios, other heavy charged particles can appear in the loops, modifying the expected effective $H \rightarrow \gamma\gamma$ branching ratio. The sensitivity for the measurement of $BR(H \rightarrow \gamma\gamma)$ at CLIC has been studied using the CLIC_SiD detector model for $\sqrt{s} = 1.4 \text{ TeV}$ and an integrated luminosity of 1.5 ab^{-1} . The SM branching ratio for $m_H = 126 \text{ GeV}$ is 0.23 % which results in approximately 840 signal events. The experimental signature for $e^+e^- \rightarrow H\nu_e\bar{\nu}_e; H \rightarrow \gamma\gamma$ is two high p_T photons with $m(\gamma\gamma) \approx m_H$ and missing momentum from the $\nu_e\bar{\nu}_e$ system. All relevant SM background processes with one or two photons in the final state have been considered. In addition to the photons from the hard interaction, the MC samples include additional ISR and FSR photons.

The following preselection cuts are applied to restrict the analysis to relevant events. At least two reconstructed photons each with energy $E_\gamma > 15 \text{ GeV}$ and $p_T > 10 \text{ GeV}$ are required. The two highest energy photons passing these requirements are used to form the H candidate and the preselection requires an invariant mass consistent with m_H , $115 \text{ GeV} < m(\gamma\gamma) < 140 \text{ GeV}$. The highest energy photon in the event is required to have $p_T > 40 \text{ GeV}$. In addition, to remove contributions from FSR, both photons are required to be isolated with no reconstructed particle with $p_T > 5 \text{ GeV}$ within a cone of half-angle 500 mrad centred on the photon. Furthermore, the remaining reconstructed energy after excluding the Higgs candidate has to be below 250 GeV. The cross sections and efficiencies of the preselection cuts for the signal and the main backgrounds are listed in [Table 23](#). At this stage in the event selection the background dominates.

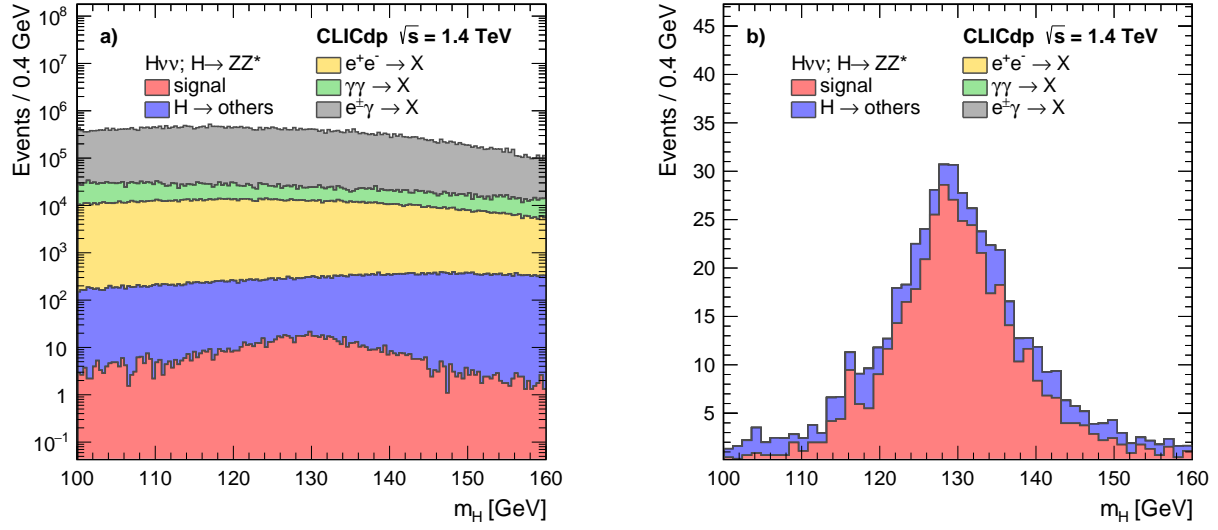


Fig. 15: Reconstructed Higgs invariant mass distributions of $H \rightarrow ZZ^* \rightarrow q\bar{q}l^+l^-$ events at $\sqrt{s} = 1.4$ TeV, showing the signal and main backgrounds as stacked histograms a) after preselection, and b) after the full event selection including a cut on the BDT classifier. The distributions are normalised to an integrated luminosity of 1.5 ab^{-1} .

To illustrate the photon reconstruction capabilities of the CLIC_SiD detector concept, the invariant mass of Higgs candidates in signal events after the preselection is shown in Figure 16. A fit to the distribution using a Gaussian function indicates an average mass resolution in the signal sample of $\sigma = 3.3 \text{ GeV}$.

The signal and background events are classified using a BDT. The 13 variables used to distinguish the signal from the backgrounds include:

- the invariant mass of the Higgs candidate;
- kinematic properties of the Higgs candidate;
- kinematic properties of the two photons;
- the angle between the two photons and the helicity angle of the Higgs candidate;
- the remaining reconstructed energy excluding the Higgs candidate.

For the optimal BDT cut, the total signal selection efficiency is 40.4%, corresponding to approximately 340 selected signal events in 1.5 ab^{-1} . The event selection for the signal and the main backgrounds is summarised in Table 23, leading to a statistical uncertainty of:

$$\frac{\Delta[\sigma(\text{Hv}_e\bar{\text{v}}_e) \times \text{BR}(H \rightarrow \gamma\gamma)]}{\sigma(\text{Hv}_e\bar{\text{v}}_e) \times \text{BR}(H \rightarrow \gamma\gamma)} = 14.7\%.$$

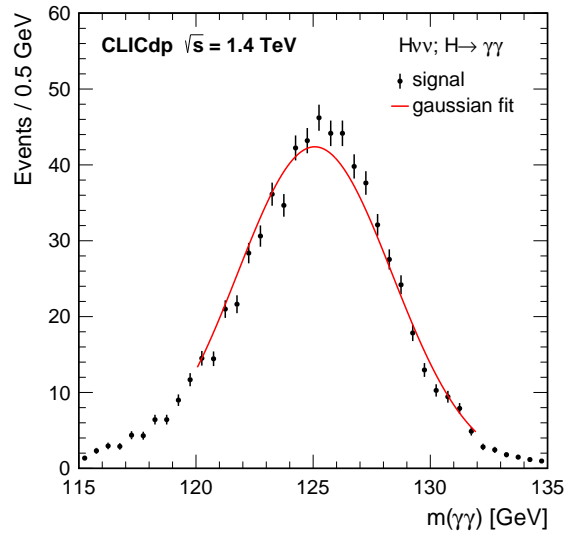


Fig. 16: Reconstructed di-photon invariant mass distribution of preselected signal $H \rightarrow \gamma\gamma$ events at $\sqrt{s} = 1.4$ TeV. The distribution is normalised to an integrated luminosity of 1.5 ab^{-1} . The statistical uncertainties correspond to the size of the simulated event sample. The line shows the fit described in the text.

6.6 $H \rightarrow Z\gamma$

As is the case for $H \rightarrow \gamma\gamma$, at lowest order, the SM decay $H \rightarrow Z\gamma$ is induced by loops of heavy charged particles. Contributions from BSM particles would lead to deviations from

the SM expectation for $BR(H \rightarrow Z\gamma)$. For $m_H = 126\text{ GeV}$, the decay $H \rightarrow Z\gamma$ is expected to have a branching ratio of $BR(H \rightarrow Z\gamma) = 0.16\%$. The potential to measure $\sigma(e^+e^- \rightarrow H\nu_e\bar{\nu}_e) \times BR(H \rightarrow Z\gamma)$ at CLIC has been studied at $\sqrt{s} = 1.4\text{ TeV}$ with the CLIC_SiD detector model, where 585 $H \rightarrow Z\gamma$ events would be expected in 1.5 ab^{-1} of data [54]. For the purpose of the event selection, only $Z \rightarrow q\bar{q}$ and $Z \rightarrow l^+l^-$ (with $l = e, \mu$) are useful, giving small event samples of 409 $q\bar{q}\gamma$, 21 $e^+e^-\gamma$ and 21 $\mu^+\mu^-\gamma$ events from $H \rightarrow Z\gamma$ in 1.5 ab^{-1} at $\sqrt{s} = 1.4\text{ TeV}$. A typical event display is shown in Figure 17.

The visible final states of the signal channels $q\bar{q}\gamma$ or $l^+l^-\gamma$ are also produced in several background processes, some of which have much larger cross sections than the signal. In addition to background with photons from the hard process, $e^+e^- \rightarrow q\bar{q}$ or $e^+e^- \rightarrow l^+l^-$ events with a FSR or ISR photon can mimic the signal.

The $H \rightarrow Z\gamma$ event selection requires at least one identified high- p_T photon and either two electrons, muons or quarks consistent with a Z decay. The reconstructed photon with the highest energy in the event is identified. Events are then considered as either $e^+e^-\gamma$, $\mu^+\mu^-\gamma$ or $q\bar{q}\gamma$ candidates. In the case where a e^+e^- or $\mu^+\mu^-$ pair is found, photons nearly collinear with the lepton trajectories (within 0.3°) are combined with the leptons under the assumption that these photons originate from bremsstrahlung. If neither a e^+e^- nor a $\mu^+\mu^-$ pair is found, all reconstructed particles except for the photon of highest energy are clustered into two jets assuming that the Z decayed into two quarks, using a jet radius of $R = 1.2$. In all cases, the selected Z decay candidate and the highest energy photon are combined to form the H candidate.

In order to reduce the number of background process events, two selection steps are performed. First, preselection cuts are applied: the Higgs candidate daughter photon and jets, electrons, or muons are only accepted if they have an energy of $E > 20\text{ GeV}$ and $p_T > 15\text{ GeV}$. In the $q\bar{q}\gamma$ channel, only jets with at least 5 particles are considered in order to suppress hadronic τ decays. In addition, the reconstructed Z and H masses in the event are required to be consistent with a $H \rightarrow Z\gamma$ decay. The second step in the event selection is three BDT selections (one for each signal final state). The input variables are the properties of the reconstructed H, Z, and γ such as mass, energy, momentum, and polar angle, event shapes such as sphericity and aplanarity, as well as missing energy distributions and particle multiplicity distributions.

For the optimal BDT cuts expected statistical significances of 2.2, 0.54 and 0.78 are found for the $q\bar{q}\gamma$, $e^+e^-\gamma$ and $\mu^+\mu^-\gamma$ channels respectively. The signal selection efficiencies and contributions from the most important backgrounds are sum-

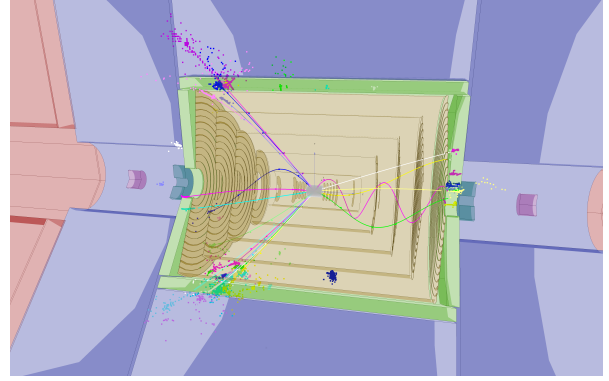


Fig. 17: Event display of a $H \rightarrow Z\gamma \rightarrow q\bar{q}\gamma$ event at $\sqrt{s} = 1.4\text{ TeV}$ in the CLIC_SiD detector. Both jets are visible. The photon creates a cluster in the central part of the electromagnetic calorimeter (blue).

Process	σ/fb	ϵ_{presel}	ϵ_{BDT}	N_{BDT}
$e^+e^- \rightarrow H\nu_e\bar{\nu}_e$; $H \rightarrow Z\gamma$; $Z \rightarrow q\bar{q}$	0.27	45.1 %	18.2 %	75
$e^+e^- \rightarrow \nu\bar{\nu}q\bar{q}\gamma$	37.3	12.3 %	0.9 %	504
$e^+e^- \rightarrow \nu\bar{\nu}q\bar{q}$	121.8	8.4 %	0.2 %	463
$e^\pm\gamma \rightarrow e^\pm q\bar{q}$	977.8	2.4 %	<0.01 %	70
$e^+e^- \rightarrow H\nu_e\bar{\nu}_e$; $H \rightarrow Z\gamma$; $Z \rightarrow e^+e^-$	0.014	38.3 %	17.3 %	4
$e^+e^- \rightarrow \nu\bar{\nu}l^+l^-\gamma$	9.6	1.6 %	0.10 %	15
$e^+e^- \rightarrow \nu\bar{\nu}l^+l^-$	23.3	1.0 %	0.03 %	12
$e^\pm\gamma \rightarrow e^\pm l^+l^-$	1942.1	0.22 %	<0.01 %	7
$e^+e^- \rightarrow H\nu_e\bar{\nu}_e$; $H \rightarrow Z\gamma$; $Z \rightarrow \mu^+\mu^-$	0.014	53.7 %	24.5 %	5
$e^+e^- \rightarrow \nu\bar{\nu}l^+l^-\gamma$	9.6	1.2 %	0.10 %	14
$e^+e^- \rightarrow \nu\bar{\nu}l^+l^-$	23.3	0.45 %	0.04 %	13
$e^\pm\gamma \rightarrow e^\pm l^+l^-$	1942.1	0.27 %	<0.01 %	9

Table 24: Preselection and selection efficiencies for $H \rightarrow Z\gamma$ events in all three considered Z decay channels. All numbers assume an integrated luminosity of 1.5 ab^{-1} at 1.4 TeV .

marised in Table 24. When the results from all three channels are combined, the achieved statistical precision at $\sqrt{s} = 1.4\text{ TeV}$ for an integrated luminosity of 1.5 ab^{-1} is:

$$\frac{\Delta[\sigma(H\nu_e\bar{\nu}_e) \times BR(H \rightarrow Z\gamma)]}{\sigma(H\nu_e\bar{\nu}_e) \times BR(H \rightarrow Z\gamma)} = 42\%.$$

With electron and/or positron polarisation the statistical precision can be increased, for example with -80% electron polarisation, $\Delta[\sigma(e^+e^- \rightarrow H\nu_e\bar{\nu}_e) \times BR(H \rightarrow Z\gamma)] \approx 31\%$. Further gains are expected from going to higher centre-of-mass energies, as the Higgs production cross section at $\sqrt{s} = 3\text{ TeV}$ is 70 % higher than at 1.4 TeV .

6.7 $H \rightarrow \mu^+\mu^-$

The measurement of the rare $H \rightarrow \mu^+\mu^-$ decay is challenging due to the very low SM branching ratio, which is about 2×10^{-4} . In the $e^+e^- \rightarrow H\nu_e\bar{\nu}_e$ production, the signature for $H \rightarrow \mu^+\mu^-$ decay is a $\mu^+\mu^-$ pair with invariant mass consistent with m_H and missing momentum. The efficient rejection of background relies on the excellent detector momentum resolution, which directly influences the width of the reconstructed di-muon invariant mass peak. Signal and background events have been simulated at $\sqrt{s} = 1.4\text{ TeV}$ and 3 TeV using the CLIC_ILD and CLIC_SiD detector models respectively [55, 56]. In contrast to all other studies, an electron beam polarisation of -80% is assumed due to the very small branching ratio for the $H \rightarrow \mu^+\mu^-$ decay. The two analyses were performed independently. They follow the same strategy but differ in some of the observables that are used in the event selection.

The most important background processes are those that include $\mu^+\mu^-\nu\bar{\nu}$ in the final state, as shown in Table 25 for 1.4 TeV and in Table 26 for 3 TeV . A significant fraction of these events are also produced from interactions involving beamstrahlung photons. Another important background is $e^+e^- \rightarrow e^+e^-\mu^+\mu^-$, where both electrons are usually emitted at very low polar angles and thus might not be detected. Tagging of these low angle electrons in the very forward calorimeters—LumiCal and BeamCal—is essential to keep this background under control.

The event selection requires two reconstructed, oppositely charged muons with a di-muon invariant mass within the relevant mass region of $105 - 145\text{ GeV}$. Events with one or more detected high-energy electrons ($E > 200\text{ GeV}$ at 1.4 TeV , $E > 250\text{ GeV}$ at 3 TeV) in the very forward calorimeters are vetoed. This introduces the possibility to veto signal events if they coincide with Bhabha scattering events. The $e^+e^- \rightarrow e^+e^-$ cross section is sufficiently high that the probability of such a coincidence within 20 bunch crossings (10 ns) is about 7% in both analyses. The cuts on the minimum energy and the minimum polar angle for vetoing forward electrons need to be chosen carefully. $e^+e^- \rightarrow e^+e^-\mu^+\mu^-$ and $e^\pm\gamma \rightarrow e^\pm\mu^+\mu^-$ events need to be rejected efficiently while a low probability for coincidence with Bhabha scattering events needs to be maintained.

The 3 TeV analysis includes some additional preselection cuts to remove phase space regions that do not include any signal events. These cuts reject events with a maximum energy of 100 GeV for any reconstructed non-muon object and a maximum energy of 20 GeV for reconstructed electrons in the central parts of the detector. The sum of the transverse momenta of the two muons, $p_T(\mu^-) + p_T(\mu^+)$, is required

to be above 50 GeV and the transverse momentum of the di-muon system should be above 25 GeV .

The final event selection uses a BDT classifier using various kinematic variables excluding the invariant mass of the di-muon system. The 1.4 TeV analysis uses visible energy of the event after removal of the di-muon system E_{vis} , transverse momentum of the di-muon system $p_T(\mu\mu)$, sum of the transverse momenta of the two muons $p_T(\mu^-) + p_T(\mu^+)$, the polar angle of the di-muon system $\theta_{\mu\mu}$, the boost of the di-muon system, $\beta_{\mu\mu}$, and the cosine of the helicity angle $\cos\theta^*$. The 3 TeV analysis uses the energy of the hardest non-muon object instead of the total visible energy and also includes the energy, transverse momentum, polar angle and azimuthal angle of both individual muons. This event selection reduces background from four-fermion processes by several orders of magnitude, whilst maintaining an overall signal selection efficiency of $\varepsilon = 30.5\%$ and $\varepsilon = 26.3\%$ at 1.4 TeV and 3 TeV respectively.

Process	σ/fb	$\varepsilon_{\text{presel}}$	ε_{BDT}	N_{BDT}
$e^+e^- \rightarrow H\nu_e\bar{\nu}_e; H \rightarrow \mu^+\mu^-$	0.094	82.5 %	30.5 %	43
$e^+e^- \rightarrow \nu_e\bar{\nu}_e\mu^+\mu^-$	232	1.1 %	0.30 %	1030
$e^\pm\gamma \rightarrow e^\pm\nu_\mu\bar{\nu}_\mu\mu^+\mu^-$	35	8.5 %	0.11 %	57
$\gamma\gamma \rightarrow \nu_\mu\bar{\nu}_\mu\mu^+\mu^-$	162	10.6 %	0.23 %	560

Table 25: List of the signal and the main backgrounds in the $H \rightarrow \mu^+\mu^-$ analysis at $\sqrt{s} = 1.4\text{ TeV}$ with the corresponding cross sections. The number of selected events assume an integrated luminosity of 1.5 ab^{-1} and -80% polarisation of the electron beam. Other processes, including $e^+e^- \rightarrow \mu^+\mu^-$ and $e^\pm\gamma \rightarrow e^\pm\mu^+\mu^-$, contribute a total of less than 10 events to the final selection.

Process	σ/fb	$\varepsilon_{\text{presel}}$	ε_{BDT}	N_{BDT}
$e^+e^- \rightarrow H\nu_e\bar{\nu}_e; H \rightarrow \mu^+\mu^-$	0.16	64 %	26 %	84
$e^+e^- \rightarrow \nu_e\bar{\nu}_e\mu^+\mu^-$	6.6	33 %	14 %	1797
$e^\pm\gamma \rightarrow e^\pm\mu^+\mu^-$	1210	6.9 %	0.011 %	262
$\gamma\gamma \rightarrow \nu_\mu\bar{\nu}_\mu\mu^+\mu^-$	413	4.3 %	0.021 %	176

Table 26: List of the signal and the most important background processes in the $H \rightarrow \mu^+\mu^-$ analysis at $\sqrt{s} = 3\text{ TeV}$ with the corresponding cross sections. The number of selected events assume an integrated luminosity of 2 ab^{-1} and -80% polarisation of the electron beam. All other processes contribute of the order of 10 events to the final event selection. The cross sections are calculated for events with invariant mass of the di-muon system between 100 GeV and 140 GeV .

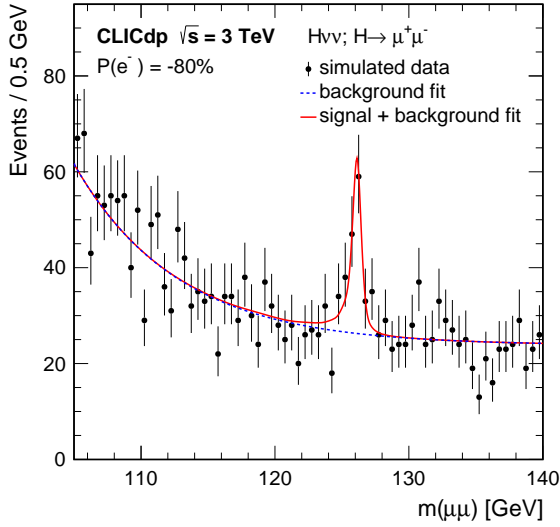


Fig. 18: Reconstructed di-muon invariant mass distribution of selected $H \rightarrow \mu^+\mu^-$ events at $\sqrt{s} = 3$ TeV. The simulated data is shown as dots while the solid line represents the fit function described in the text. The dotted line shows the background contribution of the fit function. The distribution is normalised to an integrated luminosity of 2 ab^{-1} , assuming -80% electron polarisation.

The number of signal events is extracted from the reconstructed invariant mass distribution after the event selection, as shown in Figure 18. Using a large MC sample, the signal and background shapes are extracted. The signal is described by a Gaussian distribution with asymmetric exponential tails. The combined background is parameterised as the sum of an exponential and a constant function. To assess the expected statistical precision, a large number of trial samples are generated from the expected signal and background reconstructed mass distributions and then fitted to signal and background components. For $P(e^-) = -80\%$, the expected relative uncertainty on the $\sigma(e^+e^- \rightarrow H\nu_e\bar{\nu}_e) \times BR(H \rightarrow \mu^+\mu^-)$ is 26.6 %, corresponding to a significance of 3.7, at 1.4 TeV, and 19.2 %, corresponding to a significance of 5.2, at 3 TeV. The corresponding uncertainties for unpolarised beams are:

$$\frac{\Delta[\sigma(H\nu_e\bar{\nu}_e) \times BR(H \rightarrow \mu^+\mu^-)]}{\sigma(H\nu_e\bar{\nu}_e) \times BR(H \rightarrow \mu^+\mu^-)} = 38\% \text{ at } 1.4 \text{ TeV},$$

$$\frac{\Delta[\sigma(H\nu_e\bar{\nu}_e) \times BR(H \rightarrow \mu^+\mu^-)]}{\sigma(H\nu_e\bar{\nu}_e) \times BR(H \rightarrow \mu^+\mu^-)} = 25\% \text{ at } 3 \text{ TeV}.$$

7 ZZ-fusion

Higgs boson production through the t -channel fusion of two Z bosons, $e^+e^- \rightarrow H e^+e^-$, is analogous to the WW-fusion process but gives access to complementary Higgs boson couplings. At $\sqrt{s} = 1.4$ TeV, ZZ-fusion is the sub-leading Higgs production process, with a cross section of around 25 fb, which is 10 % of that for the WW-fusion process. The potential for the measurement of the ZZ-fusion process has been investigated at $\sqrt{s} = 1.4$ TeV using the CLIC_ILD detector.

The characteristic signature of the ZZ-fusion process is two scattered beam electrons reconstructed in the forward regions of the detector, plus the Higgs boson decay products. Here, the scattered beam electrons are required to be fully reconstructed, and the final state $H \rightarrow b\bar{b}$ is considered.

Events are clustered into a four-jet topology using a k_t exclusive clustering algorithm with $R = 1.0$. For a well-reconstructed signal event, two of the resulting ‘jets’ are expected to be the reconstructed electrons, and the remaining two jets from the Higgs decay to $b\bar{b}$. The event selection requires two oppositely-charged electron candidates, separated by $|\Delta\eta| > 1$, each with $E > 100$ GeV. This preselection preserves 27 % of the $e^+e^- \rightarrow H e^+e^- \rightarrow b\bar{b} e^+e^-$ signal (3.6 fb), with the lost events almost entirely due to the scattered electrons falling outside the detector acceptance, as shown in Figure 19. After the preselection, the SM background consists mainly of events that have two real electrons and a $q\bar{q}$ pair, either from the continuum or from the decay of Z bosons. Although the preselection suppresses 98 % of the $e^+e^- \rightarrow q\bar{q} e^+e^-$ background, the accepted cross section is 48 fb, which is thirteen times larger than that for the remaining signal. A further requirement that one of the two jets associated with the Higgs decay has a b-tag value > 0.4 preserves 80 % of the remaining signal and rejects 80 % of the remaining background.

A relative likelihood classifier \mathcal{L}_1 , which treats ZZ-fusion events with $H \rightarrow b\bar{b}$ as signal and $H \rightarrow WW^*$ and $H \rightarrow ZZ^*$ as background, is used to reduce contributions from other Higgs decays. Seven variables are used to construct the likelihood: the jet clustering variable y_{45} ; the invariant mass of the two jets associated with the Higgs decay; the visible mass of the event with the scattered beam electrons removed; the higher of the b-tag values of the two jets associated with the Higgs decay; the c-tag value corresponding to the same jet; and the b-c-separation returned by the tagger, for both Higgs decay jets. Requiring a high signal likelihood, $\mathcal{L}_1 > 0.8$, reduces the $H \rightarrow b\bar{b}$ signal to 3000 events but leaves only 90 events from other Higgs decays, while also reducing the non-Higgs backgrounds to 4700 events.

Finally, to separate the signal from all backgrounds, a further relative likelihood classifier \mathcal{L}_2 is constructed using four variables that provide separation power between sig-

nal and background: the opening between the reconstructed electrons ΔR ; the recoil mass of the event determined from the momenta of the reconstructed electrons, m_{rec} ; the jet clustering variable y_{34} ; and the invariant mass of the two jets associated with the Higgs decay.

The resulting likelihood is shown in Figure 20 and gives good separation between signal and background. The likelihood distribution is fitted by signal and background components (where the normalisation is allowed to vary), giving:

$$\frac{\Delta[\sigma(\text{He}^+\text{e}^-) \times BR(\text{H} \rightarrow \text{b}\bar{\text{b}})]}{\sigma(\text{He}^+\text{e}^-) \times BR(\text{H} \rightarrow \text{b}\bar{\text{b}})} = 1.8\%$$

for 1.5 ab^{-1} at $\sqrt{s} = 1.4 \text{ TeV}$.

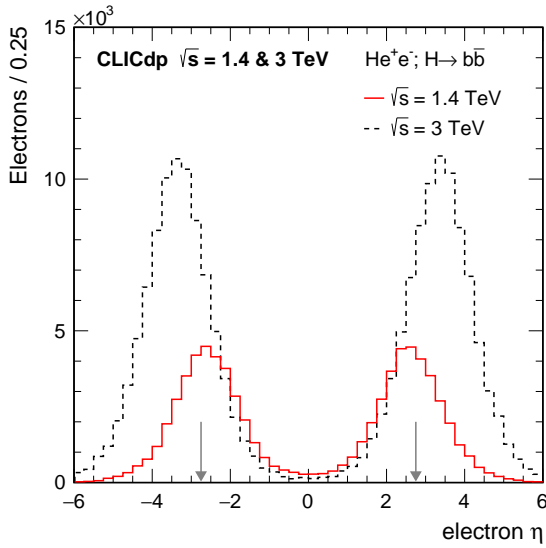


Fig. 19: Generated electron pseudorapidity distributions for $e^+e^- \rightarrow \text{He}^+e^-$ events at $\sqrt{s} = 1.4 \text{ TeV}$ and 3 TeV . The distributions are normalised to 1.5 ab^{-1} and 2 ab^{-1} respectively. The vertical arrows show the detector acceptance.

8 Top Yukawa Coupling

At an e^+e^- collider the top Yukawa coupling, y_t , can be determined from the production rate in the process where a Higgs boson is produced in association with a top quark pair, $e^+e^- \rightarrow t\bar{t}H$. The top quarks decay almost exclusively by $t \rightarrow bW$. The signal event topology thus depends on the nature of the W and Higgs boson decays. Here $H \rightarrow \text{b}\bar{\text{b}}$ decays have been studied for two $t\bar{t}H$ decay channels at $\sqrt{s} = 1.4 \text{ TeV}$ using the CLIC_SiD detector model [57, 58]:

- the fully-hadronic channel (where both W bosons decay hadronically), giving a $t\bar{t}H$ final state of eight jets, including four b jets;

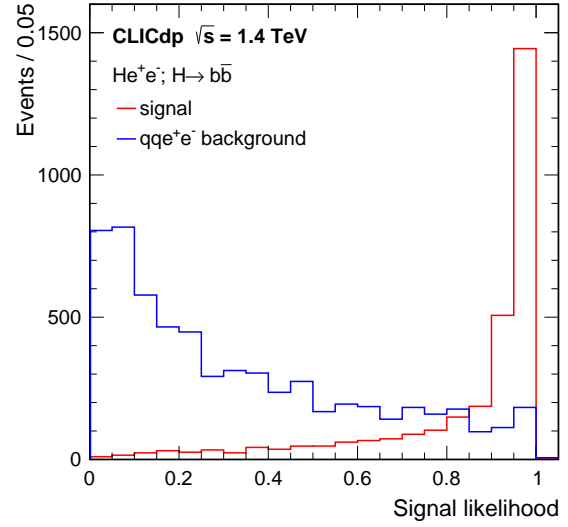


Fig. 20: Likelihood distributions for $H \rightarrow \text{b}\bar{\text{b}}$ events in the ZZ-fusion analysis at $\sqrt{s} = 1.4 \text{ TeV}$, shown for the signal and main background. The distributions are normalised to an integrated luminosity of 1.5 ab^{-1} .

- the semi-leptonic channel (where one W boson decays leptonically), giving a $t\bar{t}H$ final state of six jets (four b jets), one lepton and one neutrino,

The two channels are distinguished by first searching for isolated leptons (muons and electrons with an energy of at least 15 GeV and tau candidates from TAU-FINDER containing a track with $p_T > 10 \text{ GeV}$). If zero leptons are found, the event is classified as fully-hadronic. If one lepton is found, the event is classified as semi-leptonic. Events in which more than one lepton is found are not analysed further. The k_t algorithm is used to cluster the particles of each event into a specific number of jets, with some particles being associated with the beam jets. Events classified as fully-hadronic are clustered into eight jets. In semi-leptonic events, the lepton is removed and the remaining particles are clustered into six jets. A semi-leptonic event is shown in Figure 21. The particles clustered into the beam jets are removed from the event and the particles included in the remaining six or eight jets are then re-clustered using the e^+e^- Durham algorithm in LCFIPLUS, which performs flavour tagging for each jet, and prevents particles from displaced vertices being split between two or more jets. The jets are combined to form candidate primary particles in such a way so as to minimise a χ^2 function expressing the consistency of the reconstructed di- and tri-jet invariant masses with the $t\bar{t}(H \rightarrow \text{b}\bar{\text{b}})$ hypothesis. For example, in the case of the semi-leptonic channel, the jet assignment with the minimum of:

$$\chi^2 = \frac{(m_{ij} - m_W)^2}{\sigma_W^2} + \frac{(m_{jk} - m_t)^2}{\sigma_t^2} + \frac{(m_{lm} - m_H)^2}{\sigma_H^2},$$

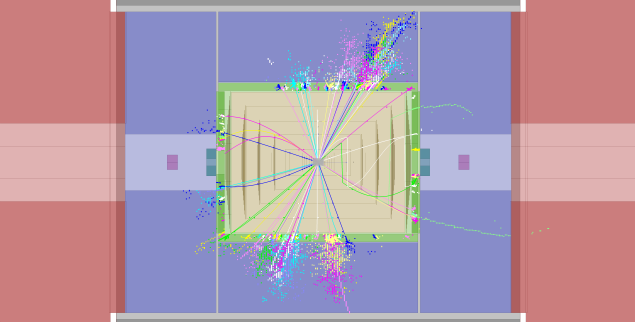


Fig. 21: Event display of a $t\bar{t}H \rightarrow b\bar{b}b\bar{b}q\bar{q}\tau^-\bar{\nu}_\tau$ event at $\sqrt{s} = 1.4\text{TeV}$ in the CLIC_SiD detector. The tau lepton decays hadronically.

gives the W, top and Higgs candidates, where m_{ij} is the invariant mass of the jet pair used to reconstruct the W candidate, m_{ijk} is the invariant mass of the three jets used to reconstruct the top quark candidate and m_{lm} is the invariant mass of the jet pair used to reconstruct the Higgs candidate. The expected invariant mass resolutions $\sigma_{W,t,H}$ were estimated from combinations of two or three reconstructed jets matched to W, top and Higgs particles on generator level.

Having forced each event into one of the two signal-like topologies, multivariate BDT classifiers (one for fully-hadronic events and one for semi-leptonic events) are used to separate signal and background. The discriminating variables include: kinematic quantities such as the reconstructed Higgs mass, the visible energy in the jets and the missing p_T ; angular variables such as the angles between the Higgs decay products in the rest frame of the Higgs candidate with respect to its flight direction and the angle between the momenta of the top and Higgs candidates; event variables such as thrust, sphericity and the number of particles in the event; and flavour tag variables for the four most likely b-jets. As an example, the BDT response distributions for the fully-hadronic channel are shown in Figure 22. The selection is chosen to maximise the signal significance. The expected numbers of selected events for 1.5ab^{-1} of $\sqrt{s} = 1.4\text{TeV}$ data are listed in Table 27. The contributions from other investigated background processes were found to be negligible. The $t\bar{t}H$ cross section can be measured with an accuracy of 12.3% in the semi-leptonic channel and 11.4% in the hadronic channel. The combined precision of the two channels is 8.4%.

To translate the measurement of the $t\bar{t}H$ cross section into a measurement of the top Yukawa coupling, a correction is applied to take into account the contribution from the Higgs-strahlung diagram, where the Higgs boson is radiated off the intermediate Z boson in $e^+e^- \rightarrow t\bar{t}$ [59, 60]. To evaluate the small degradation in sensitivity, the WHIZARD program is

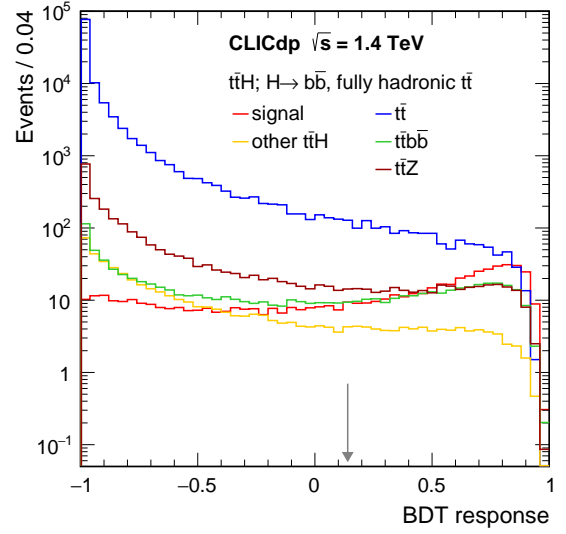


Fig. 22: BDT classifier distributions for fully-hadronic $t\bar{t}H$ events at $\sqrt{s} = 1.4\text{TeV}$, shown for the $t\bar{t}H$ signal and main backgrounds. The distributions are normalised to an integrated luminosity of 1.5ab^{-1} . The vertical arrow shows the value of the cut, chosen to give the highest significance.

Process	Events in 1.5ab^{-1}	Selected as	
		HAD	SL
$e^+e^- \rightarrow t\bar{t}H, 6 \text{ jet}, H \rightarrow b\bar{b}$	647	357	9
$e^+e^- \rightarrow t\bar{t}H, 4 \text{ jet}, H \rightarrow b\bar{b}$	623	62	233
$e^+e^- \rightarrow t\bar{t}H, 2 \text{ jet}, H \rightarrow b\bar{b}$	150	1	20
$e^+e^- \rightarrow t\bar{t}H, 6 \text{ jet}, H \not\rightarrow b\bar{b}$	473	38	8
$e^+e^- \rightarrow t\bar{t}H, 4 \text{ jet}, H \not\rightarrow b\bar{b}$	455	5	19
$e^+e^- \rightarrow t\bar{t}H, 2 \text{ jet}, H \not\rightarrow b\bar{b}$	110	0	1
$e^+e^- \rightarrow t\bar{t}b\bar{b}, 6 \text{ jet}$	824	287	8
$e^+e^- \rightarrow t\bar{t}b\bar{b}, 4 \text{ jet}$	794	44	175
$e^+e^- \rightarrow t\bar{t}b\bar{b}, 2 \text{ jet}$	191	1	14
$e^+e^- \rightarrow t\bar{t}Z, 6 \text{ jet}$	2,843	316	12
$e^+e^- \rightarrow t\bar{t}Z, 4 \text{ jet}$	2,738	49	170
$e^+e^- \rightarrow t\bar{t}Z, 2 \text{ jet}$	659	1	13
$e^+e^- \rightarrow t\bar{t}$	203,700	1,399	523
$e^+e^- \rightarrow q\bar{q}q\bar{q}l\nu(\text{non-}t\bar{t})$	68,300	11	70
$e^+e^- \rightarrow q\bar{q}q\bar{q}$	2.0×10^6	195	0

Table 27: Expected numbers of signal and background events in the fully-hadronic (HAD) and semi-leptonic (SL) channels for 1.5ab^{-1} at $\sqrt{s} = 1.4\text{TeV}$. The columns show the total numbers of events before selection and the numbers of events passing the fully-hadronic and semi-leptonic BDT selections. No preselection is applied in the analysis.

used to calculate the cross section for the inclusive process $e^+e^- \rightarrow t\bar{t}H$ as a function of the value of the top Yukawa coupling. The factor required to translate the measured cross section uncertainty into a coupling uncertainty is determined from the slope of the cross section at the SM value of the top Yukawa coupling, and is found to be:

$$\frac{\Delta y_t}{y_t} = 0.53 \frac{\Delta \sigma}{\sigma},$$

which is slightly larger than the factor of 0.50 expected without the Higgsstrahlung diagram. Thus, the expected precision on the top Yukawa coupling is:

$$\frac{\Delta y_t}{y_t} = 4.43\%,$$

for 1.5 ab^{-1} of data at $\sqrt{s} = 1.4 \text{ TeV}$ without beam polarisation. This value is expected to improve to about 4.0% for the same amount of data collected using the $P(e^-) = -80\%$ polarisation configuration [61]. Since the cross section for the $t\bar{t}H$ cross section falls with increasing \sqrt{s} (see Figure 2), the precision with 2 ab^{-1} at 3 TeV is not expected to be better than the result presented here.

9 Double Higgs Production

In e^+e^- collisions at high energy, double Higgs production, $e^+e^- \rightarrow HH\nu_e\bar{\nu}_e$, can occur through the processes shown in Figure 23. Despite the small cross section (0.15 fb and 0.59 fb for CLIC operated at $\sqrt{s} = 1.4 \text{ TeV}$ and 3 TeV, respectively), measurements of the double Higgs production rate can be used to extract the Higgs boson trilinear self-coupling parameter λ , that determines the shape of the fundamental Higgs potential. BSM physics scenarios can introduce deviations of λ from its SM value of up to tens of percent [62]. The physics potential for the measurement of this coupling has been studied using the CLIC_ILD detector model for 1.5 ab^{-1} of data at $\sqrt{s} = 1.4 \text{ TeV}$ and for 2 ab^{-1} of data at $\sqrt{s} = 3 \text{ TeV}$. The process $e^+e^- \rightarrow HHe^+e^-$ has not been included as its cross section is about an order of magnitude smaller compared to $e^+e^- \rightarrow HH\nu_e\bar{\nu}_e$.

The dominant signature for $e^+e^- \rightarrow HH\nu_e\bar{\nu}_e$ production occurs when both Higgs bosons decay to b quarks, resulting in an event signature of four b-jets and missing momentum. Consequently, events are first clustered into four jets using the k_t algorithm with a jet size of $R = 0.7$, which was found to minimise the overlap between reconstructed W and Z bosons in the $e^+e^- \rightarrow q\bar{q}q\bar{q}\nu\bar{\nu}$ process. Having forced the event into the four-jet topology, Higgs boson candidates are formed by combining the reconstructed jets into two jet pairs. In each event there are three possible jet-pairings to Higgs bosons. The most likely is selected by dividing the

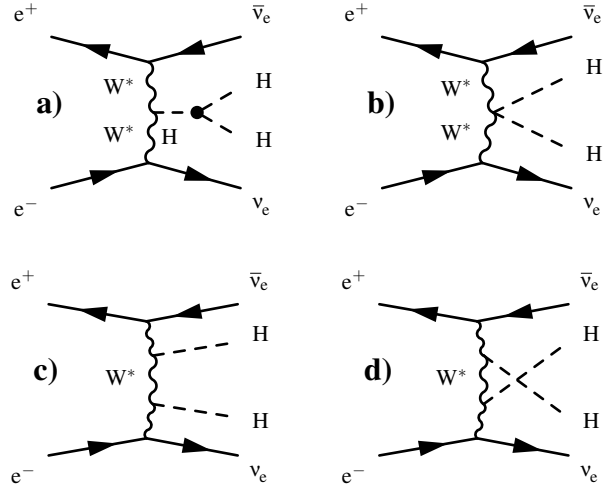


Fig. 23: Feynman diagrams of leading-order processes that produce two Higgs bosons and missing energy at CLIC at $\sqrt{s} = 1.4 \text{ TeV}$ and 3 TeV. The diagram (a) is sensitive to the trilinear Higgs self-coupling λ . The diagram (b) is sensitive to the quartic coupling g_{HHWW} . All four diagrams are included in the generated $e^+e^- \rightarrow HH\nu_e\bar{\nu}_e$ signal samples.

events into two hemispheres using the sign of the angle between the jet momentum vector and the event thrust axis. If exactly two jets are found in each hemisphere, the jets in the two hemispheres form the two Higgs candidates. Otherwise the pairing which minimises:

$$\Delta^2 = (m_{ij} - m_H)^2 + (m_{kl} - m_H)^2,$$

is chosen, where m_{ij} and m_{kl} are the invariant masses of the jet pairs used to reconstruct the Higgs candidates.

Signal and background events are separated using a neural network technique that exploits different event features including: the jet flavour tagging information; the number of isolated leptons (electrons, muons and taus); as well as kinematic distributions of the four jets and the two reconstructed Higgs bosons. All Higgs boson decays are considered as signal in the training of the neural network classifier. The most important background processes for this analysis are: $e^+e^- \rightarrow q\bar{q}q\bar{q}\nu\bar{\nu}$, $e^+e^- \rightarrow q\bar{q}q\bar{q}l\nu$ and $e^+e^- \rightarrow q\bar{q}q\bar{q}ll$. Assuming unpolarised beams, the expected uncertainties on the double Higgs production cross section for 1.5 ab^{-1} at $\sqrt{s} = 1.4 \text{ TeV}$ and 2 ab^{-1} at $\sqrt{s} = 3 \text{ TeV}$ are:

$$\frac{\Delta[\sigma(HH\nu_e\bar{\nu}_e)]}{\sigma(HH\nu_e\bar{\nu}_e)} = 34\% \text{ at } 1.4 \text{ TeV},$$

$$\frac{\Delta[\sigma(HH\nu_e\bar{\nu}_e)]}{\sigma(HH\nu_e\bar{\nu}_e)} = 16\% \text{ at } 3 \text{ TeV}.$$

The double Higgs production cross section is sensitive to the trilinear Higgs self-coupling λ . Since diagrams not in-

volving λ also contribute to the $e^+e^- \rightarrow HH\nu_e\bar{\nu}_e$ process, their effect must be taken into account. The relation between the relative uncertainty on the cross section and the relative uncertainty of the Higgs trilinear coupling can be approximated as:

$$\frac{\Delta\lambda}{\lambda} \approx \kappa \cdot \frac{\Delta[\sigma(HH\nu_e\bar{\nu}_e)]}{\sigma(HH\nu_e\bar{\nu}_e)}.$$

The value of κ can be determined from the WHIZARD generator by parameterising the $e^+e^- \rightarrow HH\nu_e\bar{\nu}_e$ cross section as a function of the input value for λ , as indicated in Figure 24. The fact that the slope is negative indicates that the main dependence on λ enters through interference with other SM diagrams. The value of κ is determined from the derivative of the cross section dependence as a function of λ , evaluated at its SM value, giving $\kappa = 1.22$ and $\kappa = 1.47$ at 1.4 TeV and 3 TeV, respectively. However, this method does not account for the possibility that the event selection might preferentially favour some diagrams over others, and hence change the analysis sensitivity to λ .

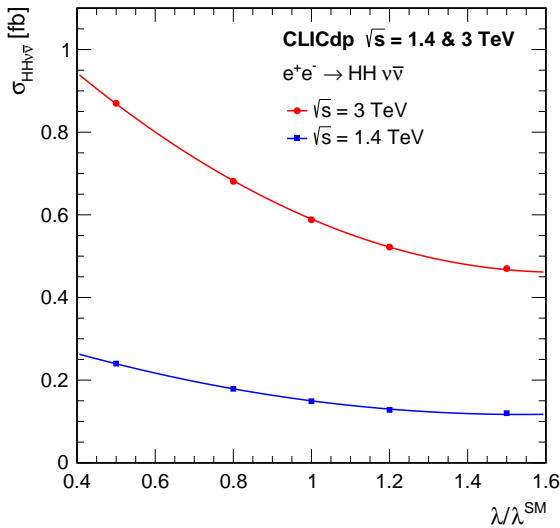


Fig. 24: Cross section for the $e^+e^- \rightarrow HH\nu_e\bar{\nu}_e$ process as a function of the ratio $\lambda/\lambda^{\text{SM}}$ at $\sqrt{s} = 1.4 \text{ TeV}$ and 3 TeV .

An alternative technique is to fit the output neural network distribution with a combination of templates from signal $e^+e^- \rightarrow HH\nu_e\bar{\nu}_e$ MC samples generated with various values of λ , in addition to the other SM background processes. This method has the advantage that it correctly accounts for the possibility that the event selection favours some diagrams over others. The template method is used to extract the experiment sensitivity to λ , while the cross section dependence described above is used as a cross check. In the case

of zero beam polarisation, the template fit method gives:

$$\Delta\lambda/\lambda = 32\% \text{ at } \sqrt{s} = 1.4 \text{ TeV},$$

$$\Delta\lambda/\lambda = 16\% \text{ at } \sqrt{s} = 3 \text{ TeV}.$$

Because the process involving the trilinear Higgs coupling involves t -channel WW-fusion, it can be enhanced by operating with polarised beams. For the case of $P(e^-) = -80\%$, this yields:

$$\Delta\lambda/\lambda = 24\% \text{ at } \sqrt{s} = 1.4 \text{ TeV},$$

$$\Delta\lambda/\lambda = 12\% \text{ at } \sqrt{s} = 3 \text{ TeV}.$$

The statistical precision on λ improves to 11% when combining both energy stages.

10 Higgs Mass

At a centre-of-mass energy of $\sqrt{s} = 350 \text{ GeV}$, the Higgs mass parameter can be measured in the $e^+e^- \rightarrow ZH$ process. The Higgs mass can be extracted from the four-momentum recoiling against in Z boson using $Z \rightarrow e^+e^-$ or $Z \rightarrow \mu^+\mu^-$ events as described in Section 5. Due to the small branching ratios for leptonic Z boson decay channels and the impact of the CLIC beamstrahlung spectrum, the achievable precision is limited to 110 MeV.

In a different approach, the Higgs mass is reconstructed from the measured four-vectors of its decay products. The best precision is expected using $H \rightarrow b\bar{b}$ decays in $e^+e^- \rightarrow H\nu_e\bar{\nu}_e$ events at high energy. For this purpose, the analysis described in Section 6.1 has been modified. After the preselection, a single BDT is used at each energy to select $H \rightarrow b\bar{b}$ decays. In contrast to the coupling measurement, the flavour tagging information is included in the BDT classifier.

The invariant mass distribution for selected events at $\sqrt{s} = 1.4 \text{ TeV}$ is shown in Figure 25. The Higgs mass is extracted in the range $105 < m_{b\bar{b}} < 145 \text{ GeV}$ where good purity of the signal channel is achieved. At the nominal Z boson mass, a second peak from $e^+e^- \rightarrow H\nu_e\bar{\nu}_e; Z \rightarrow b\bar{b}$ events is visible. These events can be used to calibrate the jet energy scale for the precision measurement of the Higgs boson mass.

A template fit using $e^+e^- \rightarrow H\nu_e\bar{\nu}_e; H \rightarrow b\bar{b}$ event samples generated using slightly shifted values for the Higgs mass parameter is performed. The Higgs mass and production cross section are extracted simultaneously. The following statistical precisions on the Higgs mass are achieved:

$$\Delta(m_H) = 47 \text{ MeV at } 1.4 \text{ TeV},$$

$$\Delta(m_H) = 44 \text{ MeV at } 3 \text{ TeV}.$$

A combination of both energy stages would lead to a precision of 32 MeV.

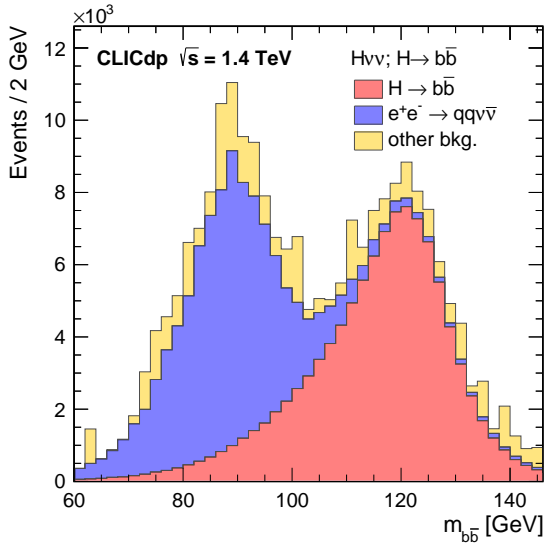


Fig. 25: Reconstructed di-jet invariant mass distribution of selected $H \rightarrow b\bar{b}$ events at $\sqrt{s} = 1.4$ TeV, showing the signal and backgrounds as stacked histograms. The distributions are normalised to an integrated luminosity of 1.5 ab^{-1} .

11 Combined Fits

The results discussed in the preceding sections are summarised in Table 28 and Table 29. From the σ and $\sigma \times BR$ measurements given in the tables the Higgs coupling parameters and total width are extracted by a global fit as described below. Here, a -80% electron polarisation is assumed for the 1.4 TeV and the 3 TeV stages. The increase in cross section is taken into account by multiplying the event rates with a factor of 1.8 (see Table 3), resulting in a reduction of the uncertainties by a factor of $\sqrt{1.8}$. This approach is conservative since it assumes that all backgrounds including those from s -channel processes, which do not receive the same enhancement by polarisation, scale with the same factor.

A few of the observables listed in Table 29 were studied only at $\sqrt{s} = 1.4$ TeV, but not at $\sqrt{s} = 3$ TeV. In cases where those observables have a significant impact on the combined fits described in this section, the precisions obtained at $\sqrt{s} = 1.4$ TeV were extrapolated to $\sqrt{s} = 3$ TeV. The extrapolation is based on the ratio of signal events within the detector acceptance at 1.4 TeV and 3 TeV. It is assumed that the background processes scale in the same way with \sqrt{s} as the signal events. This is conservative, because the signal Higgs bosons are produced in vector boson fusion while several backgrounds are dominated by s -channel diagrams which decrease with increasing \sqrt{s} .

Since the physical observables (σ or $\sigma \times BR$) typically depend on several coupling parameters and on the total width, these parameters are extracted with a combined fit of all

measurements. To provide a first indication of the overall impact of the CLIC physics programme, simple fits considering only the statistical uncertainties of the measurements are performed. Two types of fits are used: A model-independent fit making minimal theoretical assumptions, and a model-dependent fit following the strategies used for the interpretation of LHC Higgs results.

Both fits are based on a χ^2 minimisation using the MINUIT package [63]. The global χ^2 is constructed from the sum of individual χ^2 values for each independent measurement and its respective statistical uncertainty. These measurements, presented in detail in the preceding sections, are either a total cross section σ in the case of the measurement of $e^+e^- \rightarrow ZH$ via the recoil mass technique or cross section \times branching ratio $\sigma \times BR$ for specific Higgs production modes and decays. To obtain the expected sensitivity for CLIC it is assumed that for all measurements the value expected in the SM has been measured, so only the statistical uncertainties of each measurement are used in the χ^2 calculation. The χ^2 for one individual measurement is then given by:

$$\chi_i^2 = \frac{(C_i/C_i^{\text{SM}} - 1)^2}{\Delta F_i^2},$$

where C_i is the fitted value of the relevant combination of relevant Higgs couplings (and total width) describing the particular measurement, C_i^{SM} is the SM expectation, and ΔF_i is the statistical uncertainty of the measurement of the considered process. The full χ^2 then is given by:

$$\chi^2 = \sum_i \frac{(C_i/C_i^{\text{SM}} - 1)^2}{\Delta F_i^2}.$$

The C_i 's depend on the particular measurements and on the type of fit (model independent or model dependent), given in detail below. In addition, correlations between measurements are taken into account in cases where they are expected to be large. This applies to the measurements of $\sigma \times BR$ for $H \rightarrow b\bar{b}, c\bar{c}, gg$ in Higgsstrahlung and WW-fusion events at 350 GeV, which are extracted in a combined fitting procedure.

11.1 Model-independent Fit

The model-independent fit makes minimal assumptions, such as the narrow width approximation, to provide the description of the individual measurements in terms of Higgs couplings and of the total width, Γ_H . Here, the total cross section of $e^+e^- \rightarrow ZH$ depends on:

$$C_{ZH} = g_{HZZ}^2,$$

Channel	Measurement	Observable	Statistical precision
			350 GeV 500 fb ⁻¹
ZH	Recoil mass distribution	m_H	110 MeV
ZH	$\sigma(\text{ZH}) \times BR(H \rightarrow \text{invisible})$	Γ_{inv}	0.6 %
ZH	$\sigma(\text{ZH}) \times BR(Z \rightarrow l^+ l^-)$	g_{HZZ}^2	3.8 %
ZH	$\sigma(\text{ZH}) \times BR(Z \rightarrow q \bar{q})$	g_{HZZ}^2	1.8 %
ZH	$\sigma(\text{ZH}) \times BR(H \rightarrow b \bar{b})$	$g_{\text{HZZ}}^2 g_{\text{Hbb}}^2 / \Gamma_H$	0.84 %
ZH	$\sigma(\text{ZH}) \times BR(H \rightarrow c \bar{c})$	$g_{\text{HZZ}}^2 g_{\text{Hcc}}^2 / \Gamma_H$	10.3 %
ZH	$\sigma(\text{ZH}) \times BR(H \rightarrow g g)$		4.5 %
ZH	$\sigma(\text{ZH}) \times BR(H \rightarrow \tau^+ \tau^-)$	$g_{\text{HZZ}}^2 g_{\text{H}\tau\tau}^2 / \Gamma_H$	6.2 %
ZH	$\sigma(\text{ZH}) \times BR(H \rightarrow WW^*)$	$g_{\text{HZZ}}^2 g_{\text{HWW}}^2 / \Gamma_H$	5.1 %
Hv _e $\bar{\nu}_e$	$\sigma(\text{Hv}_e \bar{\nu}_e) \times BR(H \rightarrow b \bar{b})$	$g_{\text{HWW}}^2 g_{\text{Hbb}}^2 / \Gamma_H$	1.9 %
Hv _e $\bar{\nu}_e$	$\sigma(\text{Hv}_e \bar{\nu}_e) \times BR(H \rightarrow c \bar{c})$	$g_{\text{HWW}}^2 g_{\text{Hcc}}^2 / \Gamma_H$	14.3 %
Hv _e $\bar{\nu}_e$	$\sigma(\text{Hv}_e \bar{\nu}_e) \times BR(H \rightarrow g g)$		5.7 %

Table 28: Summary of the precisions obtainable for the Higgs observables in the first stage of CLIC for an integrated luminosity of 500 fb⁻¹ at $\sqrt{s} = 350$ GeV, assuming unpolarised beams. For the branching ratios, the measurement precision refers to the expected statistical uncertainty on the product of the relevant cross section and branching ratio; this is equivalent to the expected statistical uncertainty of the product of couplings divided by Γ_H as indicated in the third column.

Channel	Measurement	Observable	Statistical precision	
			1.4 TeV 1.5 ab ⁻¹	3 TeV 2.0 ab ⁻¹
Hv _e $\bar{\nu}_e$	H $\rightarrow b \bar{b}$ mass distribution	m_H	47 MeV	44 MeV
Hv _e $\bar{\nu}_e$	$\sigma(\text{Hv}_e \bar{\nu}_e) \times BR(H \rightarrow b \bar{b})$	$g_{\text{HWW}}^2 g_{\text{Hbb}}^2 / \Gamma_H$	0.4 %	0.3 %
Hv _e $\bar{\nu}_e$	$\sigma(\text{Hv}_e \bar{\nu}_e) \times BR(H \rightarrow c \bar{c})$	$g_{\text{HWW}}^2 g_{\text{Hcc}}^2 / \Gamma_H$	6.1 %	6.9 %
Hv _e $\bar{\nu}_e$	$\sigma(\text{Hv}_e \bar{\nu}_e) \times BR(H \rightarrow g g)$		5.0 %	4.3 %
Hv _e $\bar{\nu}_e$	$\sigma(\text{Hv}_e \bar{\nu}_e) \times BR(H \rightarrow \tau^+ \tau^-)$	$g_{\text{HWW}}^2 g_{\text{H}\tau\tau}^2 / \Gamma_H$	4.2 %	4.4 %
Hv _e $\bar{\nu}_e$	$\sigma(\text{Hv}_e \bar{\nu}_e) \times BR(H \rightarrow \mu^+ \mu^-)$	$g_{\text{HWW}}^2 g_{\text{H}\mu\mu}^2 / \Gamma_H$	38 %	25 %
Hv _e $\bar{\nu}_e$	$\sigma(\text{Hv}_e \bar{\nu}_e) \times BR(H \rightarrow \gamma \gamma)$		15 %	10 %*
Hv _e $\bar{\nu}_e$	$\sigma(\text{Hv}_e \bar{\nu}_e) \times BR(H \rightarrow Z \gamma)$		42 %	30 %*
Hv _e $\bar{\nu}_e$	$\sigma(\text{Hv}_e \bar{\nu}_e) \times BR(H \rightarrow WW^*)$	$g_{\text{HWW}}^4 / \Gamma_H$	1.0 %	0.7 %*
Hv _e $\bar{\nu}_e$	$\sigma(\text{Hv}_e \bar{\nu}_e) \times BR(H \rightarrow ZZ^*)$	$g_{\text{HWW}}^2 g_{\text{HZZ}}^2 / \Gamma_H$	5.6 %	3.9 %*
He ⁺ e ⁻	$\sigma(\text{He}^+ e^-) \times BR(H \rightarrow b \bar{b})$	$g_{\text{HZZ}}^2 g_{\text{Hbb}}^2 / \Gamma_H$	1.8 %	2.3 %*
t \bar{t} H	$\sigma(t \bar{t} H) \times BR(H \rightarrow b \bar{b})$	$g_{\text{Htt}}^2 g_{\text{Hbb}}^2 / \Gamma_H$	8.4 %	—
HHv _e $\bar{\nu}_e$	$\sigma(\text{HHv}_e \bar{\nu}_e)$	λ	32 %	16 %
HHv _e $\bar{\nu}_e$	with -80 % e ⁻ polarisation	λ	24 %	12 %

Table 29: Summary of the precisions obtainable for the Higgs observables in the higher-energy CLIC stages for integrated luminosities of 1.5 ab⁻¹ at $\sqrt{s} = 1.4$ TeV, and 2.0 ab⁻¹ at $\sqrt{s} = 3$ TeV. In both cases unpolarised beams have been assumed. The ‘—’ indicates that a measurement is not possible or relevant at this centre-of-mass energy. Numbers marked with * were extrapolated from $\sqrt{s} = 1.4$ TeV to $\sqrt{s} = 3$ TeV as explained in the text. For the branching ratios, the measurement precision refers to the expected statistical uncertainty on the product of the relevant cross section and branching ratio; this is equivalent to the expected statistical uncertainty of the product of couplings divided by Γ_H , as indicated in the third column. For the measurements from the HHv_e $\bar{\nu}_e$ process, the measurement precisions give the expected statistical uncertainties on the self-coupling parameter λ .

while for specific final states such as $e^+e^- \rightarrow ZH$; $H \rightarrow b\bar{b}$ and $e^+e^- \rightarrow H\nu_e\bar{\nu}_e$; $H \rightarrow b\bar{b}$:

$$C_{ZH, H \rightarrow b\bar{b}} = \frac{g_{HZZ}^2 g_{Hbb}^2}{\Gamma_H}$$

and:

$$C_{H\nu_e\bar{\nu}_e, H \rightarrow b\bar{b}} = \frac{g_{HWW}^2 g_{Hbb}^2}{\Gamma_H},$$

respectively.

The fit is performed with 11 free parameters: g_{HZZ} , g_{HWW} , g_{Hbb} , g_{Hcc} , $g_{H\tau\tau}$, $g_{H\mu\mu}$, g_{Htt} and Γ_H , as well as the three effective couplings g_{Hgg}^\dagger , $g_{H\gamma\gamma}^\dagger$ and $g_{HZ\gamma}^\dagger$. The latter three parameters are treated in the same way as the physical Higgs couplings in the fit.

Parameter	Relative precision		
	350 GeV 500 fb ⁻¹	+ 1.4 TeV + 1.5 ab ⁻¹	+ 3 TeV + 2 ab ⁻¹
g_{HZZ}	0.8 %	0.8 %	0.8 %
g_{HWW}	1.3 %	0.9 %	0.9 %
g_{Hbb}	2.8 %	1.0 %	0.9 %
g_{Hcc}	6.0 %	2.3 %	1.9 %
$g_{H\tau\tau}$	4.2 %	1.7 %	1.4 %
$g_{H\mu\mu}$	—	14.1 %	7.8 %
g_{Htt}	—	4.4 %	4.4 %
g_{Hgg}^\dagger	3.6 %	1.7 %	1.4 %
$g_{H\gamma\gamma}^\dagger$	—	5.7 %	3.2 %
$g_{HZ\gamma}^\dagger$	—	15.6 %	9.1 %
Γ_H	6.4 %	3.7 %	3.6 %

Table 30: Results of the model-independent fit. Values marked "—" can not be measured with sufficient precision at the given energy. For g_{Htt} , the 3 TeV case has not yet been studied, but is not expected to result in substantial improvement due to the significantly reduced cross section at high energy. The three effective couplings g_{Hgg}^\dagger , $g_{H\gamma\gamma}^\dagger$ and $g_{HZ\gamma}^\dagger$ are also included in the fit. Operation with -80% electron beam polarisation is assumed above 1 TeV.

The fit is performed in three stages, taking the statistical uncertainties obtainable from CLIC at the three considered energy stages (350 GeV, 1.4 TeV, 3 TeV) successively into account. Each new stage also includes all measurements of the previous stages. Table 30 summarises the results. They are graphically illustrated in Figure 26. Since the model-independence of the analysis hinges on the absolute measurement of $\sigma(ZH)$ at 350 GeV, which provides the coupling g_{HZZ} , the precision of all other couplings is ultimately limited by this uncertainty.

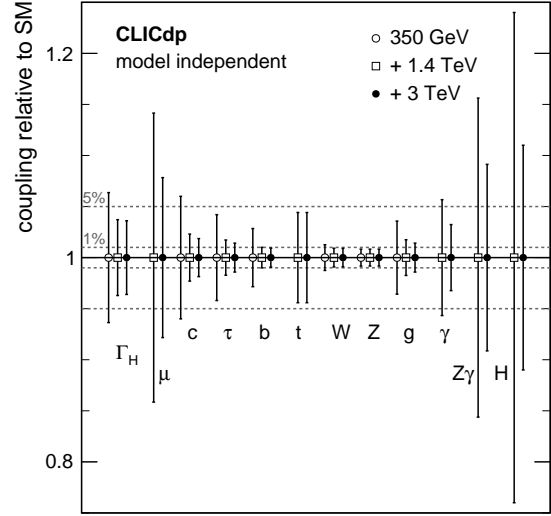


Fig. 26: Illustration of the precision of the Higgs couplings of the three-stage CLIC programme determined in a model-independent fit. The dotted lines show the relative precisions of 1 % and 5 %.

11.2 Model-dependent Fit

For the model-dependent fit, it is assumed that the Higgs decay properties can be described by ten independent parameters κ_{HZZ} , κ_{HWW} , κ_{Hbb} , κ_{Hcc} , $\kappa_{H\tau\tau}$, $\kappa_{H\mu\mu}$, κ_{Htt} , κ_{Hgg} , $\kappa_{H\gamma\gamma}$ and $\kappa_{HZ\gamma}$. These factors are defined by the ratio of the Higgs partial width divided by the partial width expected in the Standard Model as:

$$\kappa_i^2 = \Gamma_i / \Gamma_i^{\text{SM}}.$$

In this scenario, the total width is given by the sum of the ten partial widths considered, which is equivalent to assuming no invisible Higgs decays. The ratio of the total width to its SM value is thus given by:

$$\frac{\Gamma_{H,\text{md}}}{\Gamma_H^{\text{SM}}} = \sum_i \kappa_i^2 BR_i, \quad (1)$$

where BR_i is the SM branching fraction for the respective final state and the subscript "md" stands for "model-dependent". To obtain these branching fractions, a fixed value for the Higgs mass has to be imposed. For the purpose of this study, 126 GeV is assumed. The branching ratios are taken from the LHC Higgs cross section working group [20], ignoring theoretical uncertainties. To exclude effects from numerical rounding errors, the total sum of BR 's is normalised to unity.

With these definitions, the C_i 's in the χ^2 take the following forms: for the total $e^+e^- \rightarrow ZH$ cross section:

$$C_{ZH} = \kappa_{HZZ}^2;$$

while for specific final states such as $e^+e^- \rightarrow ZH$; $H \rightarrow b\bar{b}$ and $e^+e^- \rightarrow H\nu_e\bar{\nu}_e$; $H \rightarrow b\bar{b}$:

$$C_{ZH, H \rightarrow b\bar{b}} = \frac{\kappa_{HZZ}^2 \kappa_{Hbb}^2}{\left(\Gamma_{H,md}/\Gamma_H^{SM}\right)}$$

and:

$$C_{H\nu_e\bar{\nu}_e, H \rightarrow b\bar{b}} = \frac{\kappa_{HWW}^2 \kappa_{Hbb}^2}{\left(\Gamma_{H,md}/\Gamma_H^{SM}\right)},$$

respectively.

Since at the first energy stage of CLIC no significant measurements of the $H \rightarrow \mu^+\mu^-$, $H \rightarrow \gamma\gamma$ and $H \rightarrow Z\gamma$ decays are possible, the fit is reduced to six free parameters (the coupling to top is also not constrained, but this is without effect on the total width) with an appropriate rescaling of the branching ratios used in the total width for 350 GeV.

Parameter	Relative precision		
	350 GeV 500 fb ⁻¹	+ 1.4 TeV + 1.5 ab ⁻¹	+ 3 TeV + 2 ab ⁻¹
κ_{HZZ}	0.57 %	0.37 %	0.34 %
κ_{HWW}	1.1 %	0.21 %	0.14 %
κ_{Hbb}	2.0 %	0.41 %	0.24 %
κ_{Hcc}	5.9 %	2.2 %	1.7 %
$\kappa_{H\tau\tau}$	3.9 %	1.5 %	1.1 %
$\kappa_{H\mu\mu}$	—	14.1 %	7.8 %
κ_{Htt}	—	4.3 %	4.3 %
κ_{Hgg}	3.2 %	1.6 %	1.2 %
$\kappa_{H\gamma\gamma}$	—	5.6 %	3.1 %
$\kappa_{HZ\gamma}$	—	15.6 %	9.1 %
$\Gamma_{H,md,derived}$	1.6 %	0.41 %	0.28 %

Table 31: Results of the model-dependent fit. Values marked "—" can not be measured with sufficient precision at the given energy. For g_{Htt} , the 3 TeV case has not yet been studied, but is not expected to result in substantial improvement due to the significantly reduced cross section at high energy. The uncertainty of the total width is calculated from the fit results following Equation 1, taking the parameter correlations into account. Operation with -80% electron beam polarisation is assumed above 1 TeV.

As in the model-independent case the fit is performed in three stages, taking the statistical errors of CLIC at the three considered energy stages (350 GeV, 1.4 TeV, 3 TeV) successively into account. Each new stage also includes all measurements of the previous stages. The total width is not a free parameter of the fit. Instead, its uncertainty, based on the assumption given in Equation 1, is calculated from the fit results, taking the full correlation of all parameters into

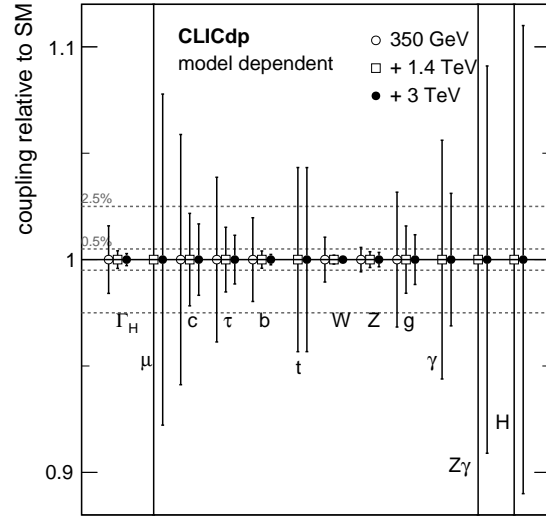


Fig. 27: Illustration of the precision of the Higgs couplings of the three-stage CLIC programme determined in a model-dependent fit. The dotted lines show the relative precisions of 0.5 % and 2.5 %.

account. Table 31 summarises the results of the fit, and Figure 27 illustrates the evolution of the precision over the full CLIC programme.

11.3 Discussion of Fit Results

The full Higgs physics programme of CLIC, interpreted with a combined fit of the couplings to fermions and gauge bosons as well as the total width, and combined with the measurement of the self-coupling, will provide a comprehensive picture of the properties of this recently discovered particle. Figure 28 illustrates the expected uncertainties of the various couplings determined in the model-independent fit as well as the self-coupling as a function of the particle mass. Combined with the quasi model-independent measurement of the total width with a precision of 3.6 %, this illustrates the power of the three-stage CLIC programme. Each of the stages contributes significantly to the total precision, with the first stage at 350 GeV providing the model-independent "anchor" of the coupling to the Z boson as well as a first measurement of the total width and coupling measurements to most fermions and bosons. The higher-energy stages add direct measurements of the coupling to top quarks, to muons and photons as well as overall improvements of the branching ratio measurements and with that of the total widths and all couplings except the one to the Z already measured in the first stage. They also provide a measurement of the self-coupling of the Higgs boson. In a model-dependent analysis, the improvement with increasing energy is even more

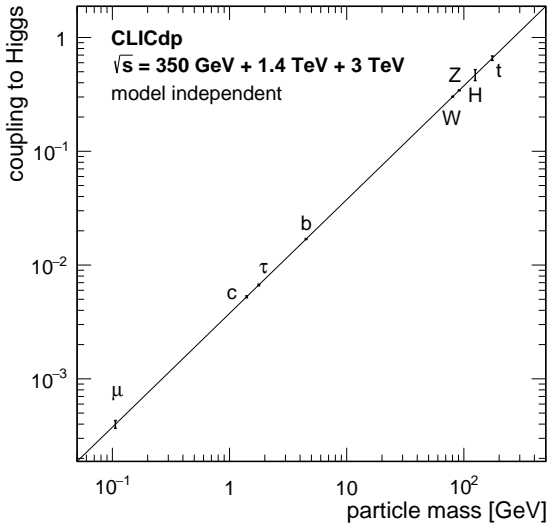


Fig. 28: Illustration of the precision of the model-independent Higgs couplings and of the self-coupling as a function of particle mass. The line shows the SM prediction that the Higgs coupling of each particle is proportional to its mass.

significant than in the model-independent fit, since the overall limit of all couplings imposed by the model-independent measurement of the ZH recoil process is removed.

12 Summary and Conclusions

A detailed study of the Higgs physics reach of CLIC has been presented in the context of CLIC operating in three energy stages, $\sqrt{s} = 350 \text{ GeV}$, 1.4 TeV and 3 TeV . The initial stage of operation, 500 fb^{-1} at $\sqrt{s} = 350 \text{ GeV}$, would allow the study of Higgs production from both the $e^+e^- \rightarrow ZH$ and the WW-fusion process. These data would yield precise model-independent measurements of the Higgs boson couplings, in particular $\Delta(g_{HZZ}) = 0.8\%$, $\Delta(g_{HWW}) = 1.3\%$ and $\Delta(g_{Hbb}) = 2.8\%$. In addition, the branching ratio to invisible decay modes would be constrained to $\Gamma_{\text{invis}}/\Gamma_H < 0.01$ at 90% C.L. and the total Higgs width would be measured to $\Delta(\Gamma_H) = 6.4\%$. Operation of CLIC at $\sqrt{s} > 1 \text{ TeV}$ would provide high-statistics samples of Higgs bosons produced through the WW-fusion process and give access to rarer processes such as $e^+e^- \rightarrow t\bar{t}H$ and $e^+e^- \rightarrow HH\nu_e\bar{\nu}_e$. Studies of these rare processes would provide measurements of the top Yukawa coupling to 4.4% and the Higgs boson self-coupling to about 10%. Furthermore, the full data sample would lead to very tight constraints on the Higgs couplings to vector bosons and fermions. In a model-independent treatment, many of the accessible couplings could be measured to better than 2%, and the model-dependent κ param-

eters could be determined with a precision of between 0.1% and 1%.

Acknowledgements This work benefited from services provided by the ILC Virtual Organisation, supported by the national resource providers of the EGI Federation. This research was done using resources provided by the Open Science Grid, which is supported by the National Science Foundation and the U.S. Department of Energy's Office of Science. The authors would like to acknowledge the use of the Oxford Particle Physics Computing Cluster. This work was supported by the Comisión Nacional de Investigación Científica y Tecnológica (CONICYT), Chile; the Ministry of Education, Youth and Sports, Czech Republic, under Grant INGO II-LG 14033; the DFG cluster of excellence "Origin and Structure of the Universe", Germany; the EC HIG-GSTOOLS project, under contract PITN-GA-2012-316704; the European Union's Horizon 2020 Research and Innovation programme under Grant Agreement no. 654168; the German - Israel Foundation (GIF); the Israel Science Foundation (ISF); the I-CORE programme of VATAT, ISF and the Israel Academy of Sciences, Israel; the Research Council of Norway; the Ministry of Education, Science and Technological Development of the Republic of Serbia through the national project OI171012; the Polish Ministry of Science and Higher Education under contract nr 3501/H2020/2016/2; the National Science Centre, Poland, HARMONIA project, under contracts 2013/10/M/ST2/00629 and UMO-2015/18/M/ST2/00518; the Romanian agencies UEFISCDI and ROSA; the Secretary of State of Research, Development and Innovation of Spain, under project FPA2011-15330-E, FPA2015-71956-REDT; the Gates Foundation, United Kingdom; the UK Science and Technology Facilities Council (STFC), United Kingdom; and the U.S. Department of Energy, Office of Science, Office of Basic Energy Sciences and Office of High Energy Physics under contract DE-AC02-06CH11357.

References

1. G. Aad et al., Phys. Lett. **B716**, 1 (2012). DOI 10.1016/j.physletb.2012.08.020
2. S. Chatrchyan et al., Phys. Lett. **B716**, 30 (2012). DOI 10.1016/j.physletb.2012.08.021
3. F. Englert, R. Brout, Phys. Rev. Lett. **13**, 321 (1964). DOI 10.1103/PhysRevLett.13.321
4. P. Higgs, Phys. Lett. **12**, 132 (1964). DOI 10.1016/0031-9163(64)91136-9
5. P. Higgs, Phys. Rev. Lett. **13**, 508 (1964). DOI 10.1103/PhysRevLett.13.508
6. G. Guralnik, C. Hagen, T. Kibble, Phys. Rev. Lett. **13**, 585 (1964). DOI 10.1103/PhysRevLett.13.585
7. P. Higgs, Phys. Rev. **145**, 1156 (1966). DOI 10.1103/PhysRev.145.1156
8. T. Kibble, Phys. Rev. **155**, 1554 (1967). DOI 10.1103/PhysRev.155.1554
9. H. Abramowicz et al., *Physics at the CLIC e^+e^- Linear Collider – Input to the Snowmass process 2013* (2013). arXiv:1307.5288
10. M. Aicheler et al. (eds.), *A Multi-TeV Linear Collider based on CLIC Technology: CLIC Conceptual Design Report* (CERN, 2012). DOI 10.5170/CERN-2012-007

11. L. Linssen et al. (eds.), *Physics and Detectors at CLIC: CLIC Conceptual Design Report* (CERN, 2012). DOI 10.5170/CERN-2012-003
12. H. Aihara et al. (eds.), *SiD Letter of Intent* (2009). SLAC-R-989, [arXiv:0911.0006](https://arxiv.org/abs/0911.0006)
13. T. Behnke et al. (eds.), *The International Linear Collider Technical Design Report - Volume 4: Detectors* (2013). ILC-Report-2013-040, [arXiv:1306.6329](https://arxiv.org/abs/1306.6329)
14. T. Abe et al., *The International Large Detector: Letter of Intent* (2010). DESY 2009-87, [arXiv:1006.3396](https://arxiv.org/abs/1006.3396)
15. M. Thomson, Nucl. Instrum. Meth. **A611**, 25 (2009). DOI 10.1016/j.nima.2009.09.009
16. J. Marshall, A. Münnich, M. Thomson, Nucl. Instrum. Meth. **A700**, 153 (2013). DOI 10.1016/j.nima.2012.10.038
17. P. Burrows et al. (eds.), *Updated baseline for a staged Compact Linear Collider* (CERN, 2016). DOI 10.5170/CERN-2016-004
18. K.A. Olive et al., Chin. Phys. **C38**, 090001 (2014). DOI 10.1088/1674-1137/38/9/090001
19. W. Kilian, T. Ohl, J. Reuter, Eur. Phys. J. **C71**, 1742 (2011). DOI 10.1140/epjc/s10052-011-1742-y
20. S. Dittmaier et al., *Handbook of LHC Higgs Cross Sections: 2. Differential Distributions* (2012). DOI 10.5170/CERN-2012-002
21. J. Beringer et al., Phys. Rev. **D86**, 010001 (2012). DOI 10.1103/PhysRevD.86.010001
22. S. Dawson et al., *Working Group Report: Higgs Boson*. FERMILAB-CONF-13-671-T, [arXiv:1310.8361](https://arxiv.org/abs/1310.8361)
23. H. Baer et al. (eds.), *The International Linear Collider Technical Design Report - Volume 2: Physics* (2013). ILC-Report-2013-040, [arXiv:1306.6352](https://arxiv.org/abs/1306.6352)
24. S. Agostinelli et al., Nucl. Instrum. Meth. **A506**, 250 (2003). DOI 10.1016/S0168-9002(03)01368-8
25. J. Allison et al., IEEE Trans. Nucl. Sci. **53**, 270 (2006). DOI 10.1109/TNS.2006.869826
26. T. Sjöstrand, S. Mrenna, P.Z. Skands, JHEP **0605**, 026 (2006). DOI 10.1088/1126-6708/2006/05/026
27. Z. Was, Nucl. Phys. Proc. Suppl. **98**, 96 (2001). DOI 10.1016/S0920-5632(01)01200-2
28. K. Fujii, *Physics Study Libraries*. URL <http://www-jlc.kek.jp/subg/offl/physim/>
29. P. Mora de Freitas, H. Videau, *Detector simulation with MOKKA / GEANT4: Present and future* (2002). LC-TOOL-2003-010
30. N. Graf, J. McCormick, AIP Conf. Proc. **867**, 503 (2006). DOI 10.1063/1.2396991
31. F. Gaede, Nucl. Instrum. Meth. **A559**, 177 (2006). DOI 10.1016/j.nima.2005.11.138
32. N.A. Graf, J. Phys. Conf. Ser. **331**, 032012 (2011). DOI 10.1088/1742-6596/331/3/032012
33. J.S. Marshall, M.A. Thomson, Eur. Phys. J. **C75**, 439 (2015). DOI 10.1140/epjc/s10052-015-3659-3
34. T. Suehara, T. Tanabe, Nucl. Instrum. Meth. **A808**, 109 (2016). DOI 10.1016/j.nima.2015.11.054
35. P. Schade, A. Lucaci-Timoce, *Description of the signal and background event mixing as implemented in the Marlin processor OverlayTiming* (2011). URL <http://cds.cern.ch/record/1443537>. LCD-Note-2011-006
36. M. Cacciari, G.P. Salam, G. Soyez, Eur. Phys. J. **C72**, 1896 (2012). DOI 10.1140/epjc/s10052-012-1896-2
37. S. Catani et al., Phys. Lett. **B269**, 432 (1991). DOI 10.1016/0370-2693(91)90196-W
38. S. Catani et al., Nucl. Phys. **B406**, 187 (1993). DOI 10.1016/0550-3213(93)90166-M
39. S.D. Ellis, D.E. Soper, Phys. Rev. **D48**, 3160 (1993). DOI 10.1103/PhysRevD.48.3160
40. C. Grefe et al., J. Phys. Conf. Ser. **513**, 032077 (2014). DOI 10.1088/1742-6596/513/3/032077
41. A. Tsaregorodtsev et al., J. Phys. Conf. Ser. **119**, 062048 (2008). DOI 10.1088/1742-6596/119/6/062048
42. J. Marshall, *Higgs Mass and Cross-Section Measurements at a 500 GeV CLIC Machine, Operating at $\sqrt{s} = 350$ GeV and 500 GeV* (2012). URL <https://cds.cern.ch/record/1498592>. LCD-Note-2012-015
43. J. Therhaag, AIP Conf. Proc. **1504**, 1013 (2009). DOI 10.1063/1.4771869
44. K.S. Cranmer, Comput. Phys. Commun. **136**, 198 (2001). DOI 10.1016/S0010-4655(00)00243-5
45. K.S. Cranmer, *Kernel Estimation for Parameterizing Distributions of Discriminating Variables* (1999). ALEPH Note 99-144
46. The OPAL Collaboration, *Search for Neutral Higgs Bosons in e^+e^- Collisions at $\sqrt{s} = 192 - 202$ GeV* (2000). OPAL Physics Note PN426
47. A.L. Read, *Modified frequentist analysis of search results (the CL_s method)* (2000). DOI 10.5170/CERN-2000-005.81. URL <http://cds.cern.ch/record/451614/>. CERN-OPEN-2000-205
48. M. Thomson, Eur. Phys. J. **C76**, 72 (2016). DOI 10.1140/epjc/s10052-016-3911-5
49. A. Münnich, *Measurement of $\sigma(e^+e^- \rightarrow H\nu\bar{\nu}) \times \text{BR}(H \rightarrow \tau\tau)$ at CLIC @ 350 GeV* (2013). URL <http://cds.cern.ch/record/1504764>. LCD-Note-2012-019
50. A. Münnich, *Taufinder: A Reconstruction Algorithm for tau Leptons at Linear Colliders* (2010). URL <http://cds.cern.ch/record/1443551/>. LCD-Note-2010-009
51. A. Münnich, *Measurement of $\sigma(e^+e^- \rightarrow H\nu\bar{\nu}) \times \text{BR}(H \rightarrow \tau\tau)$ at CLIC @ 1.4 TeV* (2013). URL <http://cds.cern.ch/record/1558360/>. LCD-Note-2012-010
52. S. Kawada et al., Eur. Phys. J. **C75**, 617 (2015). DOI 10.1140/epjc/s10052-015-3854-2
53. A. Winter, N. Watson, *Measurement of the $H \rightarrow WW^*$ Branching Ratio at 1.4 TeV using the semileptonic final state at CLIC* (2016). URL <http://cds.cern.ch/record/2157035/>. CLICdp-Note-2016-003

54. C. Greife, E. Sicking, *Physics potential of the $\sigma_{e^+e^- \rightarrow H\nu_e\bar{\nu}_e} \times \text{BR}_{H \rightarrow Z\gamma}$ measurement at a 1.4 TeV Compact Linear Collider* (2014). URL <http://cds.cern.ch/record/1749741>. CLICdp-Note-2014-003
55. C. Greife, T. Lastovicka, J. Strube, *Eur. Phys. J.* **C73**(2), 2290 (2013). DOI 10.1140/epjc/s10052-013-2290-4
56. G. Milutinović-Dumbelović et al., *Eur. Phys. J.* **C75**, 515 (2015). DOI 10.1140/epjc/s10052-015-3742-9
57. S. Redford, P. Roloff, M. Vogel, *Physics potential of the top Yukawa coupling measurement at a 1.4 TeV Compact Linear Collider using the CLIC_SiD detector* (2014). URL <http://cds.cern.ch/record/1690648>. CLICdp-Note-2014-001
58. S. Redford, P. Roloff, M. Vogel, *Study of the effect of additional background channels on the top Yukawa coupling measurement at a 1.4 TeV CLIC* (2015). URL <http://cds.cern.ch/record/1982243>. CLICdp-Note-2015-001
59. A. Djouadi, J. Kalinowski, P.M. Zerwas, *Z. Phys.* **C54**, 255 (1992). DOI 10.1007/BF01566654
60. A. Djouadi, J. Kalinowski, P.M. Zerwas, *Mod. Phys. Lett.* **A7**, 1765 (1992). DOI 10.1142/S0217732392001464
61. T. Price et al., *Eur. Phys. J.* **C75**, 309 (2015). DOI 10.1140/epjc/s10052-015-3532-4
62. R.S. Gupta, H. Rzehak, J.D. Wells, *Phys. Rev.* **D88**, 055024 (2013). DOI 10.1103/PhysRevD.88.055024
63. F. James, M. Roos, *Computer Physics Communications* **10**(6), 343 (1975). DOI 10.1016/0010-4655(75)90039-9